

# University of Wollongong - Research Online

## Thesis Collection

Title: The liquid-phase synthesis and electrochemical application of novel inorganic nanocomposites

Author: Zheng W Zhao

Year: 2008

Repository DOI:

### Copyright Warning

You may print or download ONE copy of this document for the purpose of your own research or study. The University does not authorise you to copy, communicate or otherwise make available electronically to any other person any copyright material contained on this site.

You are reminded of the following: This work is copyright. Apart from any use permitted under the Copyright Act 1968, no part of this work may be reproduced by any process, nor may any other exclusive right be exercised, without the permission of the author. Copyright owners are entitled to take legal action against persons who infringe their copyright. A reproduction of material that is protected by copyright may be a copyright infringement. A court may impose penalties and award damages in relation to offences and infringements relating to copyright material.

Higher penalties may apply, and higher damages may be awarded, for offences and infringements involving the conversion of material into digital or electronic form.

**Unless otherwise indicated, the views expressed in this thesis are those of the author and do not necessarily represent the views of the University of Wollongong.**

Research Online is the open access repository for the University of Wollongong. For further information contact the UOW Library: [research-pubs@uow.edu.au](mailto:research-pubs@uow.edu.au)

*University of Wollongong Theses Collection*

*University of Wollongong Theses Collection*

---

*University of Wollongong*

*Year 2008*

---

The liquid-phase synthesis and  
electrochemical application of novel  
inorganic nanocomposites

Zheng W. Zhao  
University of Wollongong

Zhao, Zheng W, The liquid-phase synthesis and electrochemical application of novel inorganic nanocomposites, PhD thesis, Institute for Superconducting and Electronic Materials, University of Wollongong, 2008. <http://ro.uow.edu.au/theses/49>

This paper is posted at Research Online.  
<http://ro.uow.edu.au/theses/49>

## **NOTE**

This online version of the thesis may have different page formatting and pagination from the paper copy held in the University of Wollongong Library.

## **UNIVERSITY OF WOLLONGONG**

### **COPYRIGHT WARNING**

You may print or download ONE copy of this document for the purpose of your own research or study. The University does not authorise you to copy, communicate or otherwise make available electronically to any other person any copyright material contained on this site. You are reminded of the following:

Copyright owners are entitled to take legal action against persons who infringe their copyright. A reproduction of material that is protected by copyright may be a copyright infringement. A court may impose penalties and award damages in relation to offences and infringements relating to copyright material. Higher penalties may apply, and higher damages may be awarded, for offences and infringements involving the conversion of material into digital or electronic form.

# **The Liquid-Phase Synthesis and Electrochemical Application of Novel Inorganic Nanocomposites**

A thesis submitted in fulfillment of the  
requirements for the award of the degree

**Doctor of Philosophy**

From the  
University of Wollongong

By

**ZhengWei Zhao, M. Eng., B. Eng.**

**Institute for Superconducting and Electronic  
Materials**

**Faculty of Engineering**

**2008**

## **CANDIDATE’S CERTIFICATE**

This is to certify that the work presented in this thesis is original and was carried out by the candidate at the laboratories of the Institute for Superconducting and Electronic Materials, the Faculty of Engineering, University of Wollongong, New South Wales, Australia, and has not been submitted for a degree to any other university or institution.

**ZhengWei Zhao**

## **ACKNOWLEDGEMENTS**

I would firstly like to express my deep gratitude to my supervisors, Professor Hua Kun Liu and Dr Zai Ping Guo for their academic guidance, financial support, and constant encouragement throughout the project.

Many thanks should also be given to Prof. Shi Xue Dou, Dr. Guo Xiu Wang, Dr. Jia Zhao Wang, Mr. Min Sik Park, Mr. See How Ng, Ms. Sau Yen Chew, and all the members of the Institute for Superconducting & Electronic Materials, and to all the technicians at the Department of Materials Engineering. Thanks should also go to Dr. T. Silver for helpful comments and advice on this thesis.

# TABLE OF CONTENTS

CANDIDATE'S CERTIFICATE .....	i
ACKNOWLEDGEMENTS .....	ii
TABLE OF CONTENTS .....	iii
ABSTRACT .....	vi
CHAPTER 1. INTRODUCTION .....	1
CHAPTER 2. LITERATURE REVIEW .....	4
2.1 Liquid-phase synthesis of inorganic nanocomposites.....	4
2.1.1 Co-precipitation synthetic methods .....	4
2.1.2 Microemulsion synthetic methods .....	21
2.1.3 Other synthetic methods .....	24
2.2 Lithium ion rechargeable batteries and anode materials.....	29
2.2.1. Lithium ion rechargeable batteries and anodes.....	30
2.2.2. Tin based anode materials.....	32
2.3 Direct methanol fuel cells and electrocatalysts.....	39
2.3.1 Direct methanol fuel cells .....	39
2.3.2 Electrocatalysts for direct methanol fuel cells .....	41
2.3.3 Electrocatalyst supports .....	46
2.4 Summary .....	56
CHAPTER 3. EXPERIMENTAL.....	58
3.1 Typical materials and chemicals.....	58
3.2 Experimental procedures .....	59
3.3 Structural and physical characterization of the nanocomposites .....	60
3.4 Electrode preparation .....	61
3.4.1 Electrode preparation for lithium ion batteries .....	61
3.4.2 Electrode preparation for direct methanol fuel cells.....	61
3.5 Test cell construction .....	62
3.5.1 Cell construction for lithium ion batteries .....	62
3.5.2 Cell construction for the direct methanol fuel cell.....	62
3.6 Electrochemical performance characterization.....	64
3.6.1 Electrochemical characterization for the lithium ion battery.....	64
3.6.2 Electrochemical characterization for direct methanol fuel cells.....	64
CHAPTER 4. ELECTROCHEMICAL LITHIATION AND DE-LITHIATION OF MWNT-Sn/SnNi NANOCOMPOSITES .....	66
4.1 Introduction.....	66
4.2 Synthesis and structure characterization of MWNT-Sn and MWNT-SnNi composites .....	67
4.2.1 Preparation of MWNTs .....	67

4.2.2 Preparation of MWNT nanocomposites with Sn and SnNi .....	68
4.2.3 Microstructural characterization .....	68
4.3 Electrochemical testing of nanocomposite electrodes .....	71
4.4 Conclusion .....	83
CHAPTER 5. MESOPOROUS CARBON-TIN NANOCOMPOSITES AS ANODE MATERIALS FOR THE LI-ION BATTERY .....	
5.1 Introduction.....	84
5.2 Synthesis and characterization of MC-Sn nanocomposite.....	85
5.2.1 Synthesis of the mesoporous carbon.....	85
5.2.2 Mesoporous carbon-tin nanocomposite .....	86
5.2.3 Microstructure characterization .....	86
5.3 Electrochemical testing of nanocomposite electrodes .....	88
5.4 Conclusion .....	92
CHAPTER 6. TITANIA NANOTUBE SUPPORTED TIN ANODES FOR LITHIUM INTERCALATION .....	
6.1 Introduction.....	93
6.2 Synthesis and characterization of titania nanotube supported tin.....	94
6.2.1 Synthesis of the titania nanotube supported tin anodes .....	94
6.2.2 Characterization of the titania nanotube supported tin anodes .....	94
6.3 Electrochemical properties of titania nanotube supported tin anodes .....	98
6.4 Conclusion .....	103
CHAPTER 7. NOVEL IONIC LIQUID SUPPORTED SYNTHESIS OF PLATINUM BASED ELECTROCATALYSTS ON MULTIWALLED CARBON NANOTUBES .....	
7.1 Introduction.....	104
7.2 Synthesis and characterization of the Pt/CNT nanocomposite .....	105
7.2.1 Microwave heated synthesis of Pt/CNTs.....	105
7.2.2 Characterization of the Pt/CNT nanocomposites.....	107
7.3 Electrochemical properties of Pt/CNTs .....	114
7.4 Conclusion .....	116
CHAPTER 8. PREPARATION OF POROUS CARBON SUPPORTED Pt NANOCOMPOSITES FOR DIRECT METHANOL FUEL CELLS .....	
8.1 Introduction.....	117
8.2 Synthesis and characterization of porous carbon Pt nanocomposites.....	118
8.3 Electrochemical properties of porous carbon Pt nanocomposites .....	122
8.4 Conclusion .....	125
CHAPTER 9. METHANOL TOLERANT Pt/FeO <sub>x</sub> /C NANOCOMPOSITE CATHODES FOR DIRECT METHANOL FUEL CELLS .....	
9.1 Introduction.....	127
9.2 Synthesis and characterization of Pt/FeO <sub>x</sub> /C nanocomposites .....	128
9.3 Electrochemical properties of Pt/FeO <sub>x</sub> /C nanocomposites .....	133
9.4 Conclusion .....	136
CHAPTER 10. GENERAL CONCLUSIONS.....	
	137

10.1 Review of this study .....	137
10.1.1 Tin based nanocomposites for lithium ion battery anodes.....	137
10.1.2 Pt based nanocomposites for DMFC electrocatalysts.....	139
10.2 Suggestions for future study .....	141
REFERENCES .....	142
LIST OF SYMBOLS .....	159
LIST OF FIGURES .....	160
LIST OF TABLES .....	164
PUBLICATIONS.....	165

## **ABSTRACT**

The aim of this study is to investigate various liquid-phase syntheses of novel inorganic nanocomposites for electrochemical power sources. Lithium ion batteries and fuel cells are two typical kinds of electrochemical power sources in the consumer electronics market. Lithium ion batteries are currently one of the most popular energy storage devices. Direct methanol fuel cells also have much potential as next generation electrochemical power sources, especially for small electronic devices.

Tin and Pt based nanocomposites are two types of inorganic materials studied in this work for use as alternative electrodes, as lithium ion battery anodes and as direct methanol fuel cell electrocatalysts, respectively. Different liquid-phase synthesis methods were employed to prepare these novel nanocomposites. Physical and electrochemical characterizations were carried out systematically on the as-prepared nanocomposites.

All of the results show that these novel inorganic nanocomposite materials are unique and good substitutes for the anode materials in lithium ion batteries or as electrocatalysts for direct methanol fuel cells.

## **CHAPTER 1. INTRODUCTION**

This study is targeted towards liquid-phase synthesis of various inorganic nanocomposites for lithium ion battery anodes and direct methanol fuel cell electrocatalysts. These nanostructured materials show good electrochemical performance in lithium ion batteries and electrocatalytic properties in direct methanol fuel cells.

Chapter 2 of the present study commences with an overview of the recent development of the liquid-phase synthesis method for inorganic nanoparticles, lithium ion battery tin based anodes, and direct methanol fuel cell electrocatalysts.

Chapter 3 describes the experimental methods and procedures used in this study, and the materials and chemicals chosen to accomplish the research work.

Chapter 4 presents multiwall carbon nanotube (MWNT) supported tin and tin nickel alloy nanocomposites as anodes for lithium ion batteries. A high reversible capacity, high charge/discharge efficiency, and fairly good cyclability were achieved for MWNT-Sn and MWNT-SnNi anodes in lithium ion batteries.

Chapter 5. A mesoporous carbon (MC) and tin nanocomposite was prepared by a two step liquid phase synthesis method. The mesoporous structure can successfully buffer the volume changes during the Li-Sn alloying process. The MC/Sn nanocomposites exhibited extremely good cycling stability.

Chapter 6. A new type of nanostructured titania nanotube supported tin anode was prepared for lithium ion batteries. Tin nanoparticles were abundantly decorated on the titania nanotubes by a chemical co-precipitation method. The titania nanotube and tin nanocomposite promises good retention of reversible capacity on cycling for lithium intercalation.

Chapter 7. Pt on carbon nanotube (CNT) nanocomposites were prepared by a microwave heated polyol process with ionic liquid support. It was found that the ionic liquid had a significant impact on the surface of the as-prepared CNTs, and there is a strong interaction between the ionic liquids and the CNTs. The Pt/CNT nanocomposite had higher electrochemical surface areas than commercial Pt/C catalysts, as determined by hydrogen electro-adsorption in direct methanol fuel cells.

Chapter 8. Two different types of porous carbon material supported Pt nanocomposites were prepared as anode catalysts for direct methanol fuel cells. By using a microwave assisted

polyol process, Pt nanoparticles were decorated on mesoporous carbons (MCs) and carbon aerogels (CAs). The Pt/CA catalysts have a quite homogenous dispersion of Pt nanoparticles, while Pt particles on MCs tend to agglomerate on some defect sites. Thus, Pt/CA nanocomposite showed good electrocatalytic performance towards methanol oxidation in cyclic voltammetry measurements.

Chapter 9. Pt/FeO<sub>x</sub>/C nanocomposites were synthesized by a two step impregnation method using sodium borohydride as the reducing reagent. Pt nanoparticles were found to be randomly oriented on the active carbon supports, and the iron oxides were located close to the Pt nanoparticles in the composite. The Pt/FeO<sub>x</sub>/C nanocomposite showed very good methanol tolerant performance as a cathode electrocatalyst in direct methanol fuel cells.

Chapter 10 gives an overview and summary of the study, and suggestions for further investigations.

## **CHAPTER 2. LITERATURE REVIEW**

### **2.1 Liquid-phase synthesis of inorganic nanocomposites**

Synthesis of different novel materials is a fundamental focal point of chemical research, and this interest is mandated by advancements in all areas of industry and technology. Nowadays, nanotechnology is rapidly thrusting its applications into all aspects of life, including engineering and science. Materials science and engineering have experienced tremendous growth in the field of nanocomposite development, with enhanced chemical, mechanical, and physical properties. Various liquid-phase synthetic methodologies [1] are being used to prepare inorganic nanocomposites.

#### **2.1.1 Co-precipitation synthetic methods**

Many of the earliest syntheses of nanoparticles were achieved by the co-precipitation of sparingly soluble products from aqueous solutions, followed by thermal decomposition of those products to oxides. Co-precipitation reactions involve the simultaneous occurrence of nucleation, growth, coarsening, and/or agglomeration processes. Due to the difficulties in isolating each process for independent study, the fundamental mechanisms of co-precipitation are still not thoroughly understood.

As a brief overview, co-precipitation reactions tend to exhibit the following characteristics: (i) The products of precipitation reactions are generally sparingly soluble

species formed under conditions of high supersaturation. (ii) Such conditions dictate that nucleation will be a key step of the precipitation process and that a large number of small particles will be formed. (iii) Secondary processes, such as aggregation, will dramatically affect the size, morphology, and properties of the products. (iv) The supersaturation conditions necessary to induce precipitation are usually the result of a chemical reaction. As such, any reaction conditions influencing the mixing process, such as the rate of reactant addition and the stirring rate, must be considered relevant to product size, morphology, and particle size distribution.

Although precipitation can be induced in any number of ways, chemical reactions are by far the most common method for the synthesis of nanoparticles. Generally, chemical reactions are chosen that result in products with low solubilities, such that the solution quickly reaches a supersaturated condition.

### (a) Synthesis of Metals from Aqueous Solutions

Due to their widespread application as catalysts [2], metals precipitated from aqueous solutions continue to be a thoroughly investigated subject. The precipitation of metals from aqueous or non-aqueous solutions typically requires the chemical reduction of a metal cation. Reducing agents take many forms, the most common of which are gaseous  $H_2$ , solvated  $ABH_4$  ( $A$  = alkali metal), hydrazine hydrate, and hydrazine dihydrochloride.

In theory, the reduction of any metal with an  $E$  (potential) more positive than  $-0.481$  V or negative than  $-0.23$  V, respectively, should be possible at room temperature, given a sufficient excess of reducing agent and proper control of pH. With respect to precipitating metals from solution, this would obviously include many first-row transition metal ions, such as  $\text{Fe}^{2+}$ ,  $\text{Fe}^{3+}$ ,  $\text{Co}^{2+}$ ,  $\text{Ni}^{2+}$ , and  $\text{Cu}^{2+}$ , but also many second and third row transition metals, as well as a few non-metals.

As a practical matter, the reduction of some metal ions with  $E > -0.481$  V is either not feasible or exceedingly difficult, but this is usually due to the instability of the cation in aqueous environments. However, in some instances, transition metal cations, such as  $\text{Rh}^{3+}$ , form stable complexes with hydrazine, thereby greatly limiting the available options for carrying out a reduction [3]. We should further emphasize that consideration of pH and relative redox potentials is, at best, only a guide for predicting which metals may or may not be prepared by this method.

The reduction of gold cations to gold metal is easily the single most thoroughly studied metal precipitation reaction. Gold cations, usually in the form of  $\text{AuCl}_4^-$ , are easily reduced by gaseous  $\text{H}_2$ , although  $\text{AuCl}_4^-$  is so strongly oxidizing ( $E = +1.002$  V) that weaker reducing agents such as carboxylates or alcohols are usually sufficient. Tan et al. have recently reported the synthesis of Au, Pt, Pd, and Ag nanoparticles by reduction with potassium bitartrate; all of the products formed stable colloids with the addition of a suitable stabilizing agent [4].

Normally, if thiol stabilizing agents are used, the reduction of  $\text{AuCl}_4^-$  in aqueous solution must be performed with borohydride or similar reducing agents because the complexes formed between  $\text{AuCl}_4^-$  and thiols are too stable to be reduced by citrate or other weak reducing agents. Yonezawa *et al.*, however, have demonstrated that reduction of  $\text{AuCl}_4^-$  with citrate in the presence of a thiol is possible, if the thiol and citrate are added to the gold solution simultaneously [5]. Gold colloids with 2-10 nm dimensions are achievable with this method, and narrow size distributions are possible at high thiol / Au ratios.

Silver can similarly be reduced with borohydride from aqueous  $\text{Ag}^+$  in a solution containing bis(11-trimethylammoniumdecanoylaminoethyl)disulfide dibromide (TADDD), producing monodisperse nanoparticles as small as 3.3 nm [6]. In this case, the excess borohydride reduces the disulfide to a thiol that serves as a capping ligand. The particles are easily redispersed into stable colloids in slightly acidified water.

While nanoparticulate Fe and Cu are easily reduced individually with borohydride, Chow *et al.* prepared fcc  $\text{Fe}_{1-x}\text{Cu}_x$  ( $0.6 \leq x \leq 1$ ) alloys with 30-45 nm particle sizes by reduction of aqueous  $\text{FeCl}_2 + \text{CuCl}_2$  mixtures [7]. The result is noteworthy in that Fe and Cu are not normally miscible in the equilibrium state. The formation of the alloy may, however, be facilitated by the incorporation of boron, due to formation of  $\text{Fe}_2\text{B}$ , as is known to be the case with  $\text{Fe}_{1-x}\text{Co}_x$  alloys prepared by reduction with  $\text{KBH}_4$  in aqueous solution [8].

Harris *et al.* heat-treated mixtures of CuO + CoO precipitated from aqueous solution to produce Cu<sub>80</sub>Co<sub>20</sub> alloys. The samples were heated under flowing H<sub>2</sub> at temperatures ranging from 200 to 650 °C, resulting in alloy particles with 10-20 nm particle sizes with a broad size distribution. Heat treatment at 650 °C or above resulted in decomposition to the composite metals [9].

### (b) Precipitation of Metals by Reduction from Non-aqueous Solutions

The stabilization of Au nanoparticles against agglomeration in aqueous solutions by capping ligands such as citrate is a well-documented process. Brust *et al.*, however, reported the synthesis of alkanethiol-stabilized colloidal Au nanoparticles that are stable almost indefinitely in non-polar solvents [10]. Moreover, the particles exhibited the rather unusual ability to be fully redispersed into colloids after being isolated as dry powders.

The synthesis method of Brust *et al.* [10] is noteworthy in that a two-phase reaction mixture was used to carry out the gold reduction, similar to the technique of Faraday. Starting from an aqueous solution of AuCl<sub>4</sub><sup>-</sup>, the tetrachloroaurate ions were transferred to an organic phase by vigorously mixing the aqueous solution with a solution of tetraoctylammonium bromide (TOAB) dissolved in toluene. (TOAB is a well-known phase-transfer catalyst.) After adding dodecanethiol to the organic phase, an aqueous solution of NaBH<sub>4</sub> was subsequently introduced into the mixture with rapid stirring. Colloidal gold (1-3 nm) was formed in the organic phase and subsequently isolated by

vacuum evaporation or by precipitation with methanol. The authors found that once the products were isolated as dry powders, stable colloidal suspensions could be reconstituted in any number of non-polar or weakly polar solvents, including toluene, pentane, and chloroform, but not alcohol or water. The authors further determined by infrared (IR) and X-ray photoelectron spectroscopy (XPS) that the powder, even after washing, contained thiolate and that the gold was present as Au<sup>0</sup>.

The results of Brust *et al.* triggered a flurry of research into the thiol-based stabilization of colloidal nanoparticles. Among the more significant results from these investigations, numerous new thiol-, amine-, silane-, phosphine-, and disulfide-based capping ligands have been identified [11-17], and several techniques have emerged for the exchange of capping ligands [18-21]. This effectively allows the functionality and chemical properties of the ligand shells to be tuned [22, 23]. Stoeva *et al.* have modified Brust's method to allow the gram-scale synthesis of thiol-stabilized colloidal Au particles [24].

Au nanoparticles reduced with borohydride and capped with mercaptosuccinic acid (MSA), HOOCCH<sub>2</sub>CH(SH)COOH, as reported by Chen *et al.*, exhibit the additional benefit of being dispersable in water if the capped nanoparticles are precipitated as a sodium salt [25]. The sizes of the nanoparticles were controllable within the 1-3 nm range by variation of the MSA/Au ratio.

Han *et al.* developed a method for reducing gold in non-aqueous solutions in which the solvent, in this case formamide ( $\text{HCONH}_2$ ), also served as the reducing agent [26]. The reaction mechanism appears to involve a two-step process of ligand-exchange followed by reduction, and the reaction will not proceed in the presence of oxygen. The 30 nm particles were stabilized by poly(vinylpyrrolidone) (PVP) and exhibited a narrow size distribution. It is not clear, however, as to whether the particle size can be controlled, as the PVP/Au ratio did not appear to influence the particle size.

### (c) Precipitation of Metals by Electrochemical Reduction

Although the method is not widely used, the synthesis of powdered metallic nanoparticles is possible by electrochemical reduction. The method developed by Reetz *et al.* involves the anodic dissolution of a metal and the reduction of the intermediate metallic salt at the cathode (usually Pt foil) [27]. The reaction must be carried out in the presence of a stabilizer, such as a tetraalkylammonium salt, to prevent all of the particles from simply depositing (plating) at the cathode's surface.

In Reetz *et al.*'s initial experiments, Pd metal was deposited from a 0.1 M solution of tetraoctylammonium bromide dissolved in a 4:1 mixture of acetonitrile-THF by applying a  $0.1 \text{ mA/cm}^2$  current at 1 V using a potentiostat. The monodispersed 4.8 nm particles were collected by decantation/drying and were redispersable in THF or toluene. The authors also noted that increasing the current density resulted in a substantial decrease in particle size, such that 1.4 nm particles were obtained at  $5.0 \text{ mA/cm}^2$ .

Rodriguez-Sanchez *et al.* adapted the method to the precipitation of 2-7 nm silver nanoparticles by cycling an Ag/0.1 M tetrabutylammonium bromide in acetonitrile/Pt cell from 1.35 V to -0.15 V at 500 mV/s for 5 min [28]. The authors noted a similar relationship between current density and particle size to that reported by Reetz *et al.* In a variation of this method, Mohamed *et al.* were able to deposit Au nanorods by adding  $\text{Ag}^+$  to the supporting electrolyte [29].

Asenjo *et al.* have recently developed an analogous method for the preparation of nanoparticulate strontium ferrites by electrolyzing acidic aqueous solutions of  $\text{Sr}^{2+}$  and  $\text{Fe}^{2+}$  chlorides and nitrates in a 40-80 °C temperature range [30]. The spherical products were typically on the order of ~50 nm in size, although trace impurities resulting from the electrolysis were detected in their lattices.

### (d) Precipitation of Metals by Radiation-Assisted Reduction

The most obvious example of radiation-assisted reduction is the photoreduction of aqueous  $\text{AgNO}_3$  solutions upon exposure to ultraviolet (UV) light. Huang *et al.* adapted this method to the synthesis of Ag nanoparticles by exposing a solution of  $\text{AgNO}_3$  to 243 nm radiation in the presence of poly(N-vinylpyrrolidone) (PVP) as stabilizer [31]. The average particle size could be varied from 15 to 22 nm by adjusting the PVP/ $\text{Ag}^+$  ratio.

### (e) Precipitation of Oxides from Aqueous Solutions

The precipitation of oxides, from both aqueous and non-aqueous solutions, is somewhat less straightforward than the precipitation of metals. Reactions for the synthesis of oxides can generally be broken into two categories: those that produce an oxide directly and those that produce what is best termed a precursor, as it must be subjected to further processing (drying, calcination, etc.). In either case, monodispersed nanoparticles of oxides, like those of metals, frequently require a capping ligand or other surface-bound stabilizer to prevent agglomeration of the particles.

In those cases where calcination or annealing of the samples is necessary, some agglomeration will be unavoidable. Nanoparticles can nonetheless be so obtained, but there is little chance of the particles being monodispersed. For many of the reported syntheses of oxides, monodispersity of the products was neither a requirement nor a priority for the researchers involved.

The products of co-precipitation reactions, particularly those performed at or near room temperature, are usually amorphous. In those cases where hydroxides or carbonates of mixed metals are precipitated from solution and subjected to a calcination or a post-annealing process, it is extremely difficult to experimentally determine whether the as-prepared precursor is a single-phase solid solution or a multiphase,

nearly-homogeneous mixture of the constituent metal hydroxides-carbonates-oxides that react to form a single-phase mixed-metal oxide when heated.

Many nanoparticulate metal oxides are prepared by calcining hydroxide co-precipitation products. Albuquerque *et al.* prepared spinel-structured  $\text{Ni}_{0.5}\text{Zn}_{0.5}\text{Fe}_2\text{O}_4$  by precipitating a mixture of Fe, Ni, and Zn nitrates with NaOH and calcining at 300 °C or higher [32].

The co-precipitation of metal cations as carbonates, bicarbonates, or oxalates, followed by their subsequent calcination and decomposition, is a common method for producing crystalline nanoparticulate oxides. The calcination will, however, almost invariably lead to agglomeration or, at high temperatures, aggregation and sintering. Fortunately, nanoparticulate hydroxide, carbonate, and oxalate precursors tend to decompose at relatively low temperatures (<400 °C) due to their high surface areas, thereby minimizing agglomeration and aggregation. As an example,  $\text{Ce}_{0.8}\text{Y}_{0.2}\text{O}_{1.9}$  (a fluorite-structured, oxide-ion conducting electrolyte for solid oxide fuel cells) was precipitated by the addition of oxalic acid to an aqueous solution of  $\text{Ce}(\text{NO}_3)_3$  and  $\text{Y}(\text{NO}_3)_3$ , followed by calcination [33]. Calcining at 500 °C yielded 10 nm, slightly agglomerated, roughly spherical particles. Calcining at 1000 °C resulted in 100 nm aggregates with irregular shapes, although lower calcination temperatures reduced aggregation considerably.  $\text{CeO}_2$  nanopowders, by contrast, have been prepared by calcining the product of the precipitation between  $\text{Ce}(\text{NO}_3)_3$  and  $(\text{NH}_4)_2\text{CO}_3$ , resulting in crystalline, 6 nm particles of  $\text{CeO}_2$  at calcination temperatures as low as 300 °C [34].

10-15 nm particles of NiO have been similarly prepared by precipitating aqueous  $\text{Ni}^{2+}$  solutions with  $(\text{NH}_4)_2\text{CO}_3$  and calcining the products at 400 °C [35].

Du *et al.* were able to prepare ferroelectric  $\text{Bi}_4\text{Ti}_3\text{O}_{12}$  by calcining the product from the reaction between a basic solution of  $\text{TiO}_2$  and  $\text{Bi}(\text{NO}_3)_3$ , performed in an acidic solution [36]. Agglomerate sizes ranged from 16 to 48 nm after calcining between 500 and 800 °C. When the calcination temperature was kept at 500 °C or below,  $\text{Bi}_4\text{Ti}_3\text{O}_{12}$  appeared to crystallize in a metastable tetragonal phase previously thought to be stable only at high temperatures.

In some rare instances, crystalline oxides can be precipitated from aqueous solution, eliminating the need for a calcination step and greatly reducing the risk of agglomeration. This approach is most common for simple binary oxides. 50-60 nm aggregates of 4 nm rutile-structured  $\text{TiO}_2$ , for instance, can be prepared by precipitating aqueous  $\text{TiCl}_3$  with  $\text{NH}_4\text{OH}$  under ambient conditions and stabilizing the products with poly(methyl methacrylate) [37].

The direct co-precipitation of more complex ternary oxides, while somewhat uncommon, is nonetheless possible, particularly when the product assumes a very thermodynamically favorable structure such as spinel. In such cases, the precipitation reactions are normally carried out at elevated temperatures (50-100 °C), such that the hydroxide intermediates are condensed into oxides in the same reaction vessel in which

co-precipitation was induced. Such "one-pot" synthesis techniques render calcination steps unnecessary.  $\text{Fe}_3\text{O}_4$ , for example, has been prepared as an oxide by the simple co-precipitation of  $(\text{Fe}^{2+} + 2 \text{Fe}^{3+})$  with NaOH at temperatures above 70 °C [38]. 5-25 nm particles of  $\text{MnFe}_2\text{O}_4$  were similarly prepared from aqueous  $\text{Mn}^{2+}$  and  $\text{Fe}^{2+}$  at temperatures up to 100 °C [39].  $\text{Pr}^{3+}$ -doped ceria has likewise been precipitated by aging aqueous solutions of  $\text{Ce}(\text{NO}_3)_3$  and  $\text{PrCl}_3$  at 100 °C in the presence of a hexamethylenetetramine stabilizer to yield monodispersed 13 nm particles [40]. In this case, the stabilizer indirectly serves as the precipitating agent, by raising the pH high enough to induce precipitation of the metal hydroxides.

Chinnasamy *et al.* reported an extensive series of experiments for spinel-structured  $\text{CoFe}_2\text{O}_4$  that were designed to determine the influence of reaction temperature, reactant concentration, and reactant addition rate on the size of the products [41]. In each case, aqueous solutions of  $\text{Fe}^{3+}$  and  $\text{Co}^{2+}$  were precipitated with dilute NaOH. The results were predominantly in line with expectations based on the considerations outlined in the beginning of this section: Increasing the temperature from 70 °C to 98 °C increased the average particle size from 14 to 18 nm. Increasing the NaOH concentration from 0.73 to 1.13 M increased the particle size from 16 to 19 nm. NaOH concentrations of 1.5 M or greater resulted in the formation of a secondary  $\text{FeOOH}$  phase, and slowing the NaOH addition rate appeared to broaden the particle size distribution.

Li *et al.* prepared 12 nm  $\text{CoFe}_2\text{O}_4$  by a similar route, but stabilized the product by acidification with dilute nitric acid [42]. The electrostatic repulsion of the particles created

by the adsorption of  $H^+$  at the particle surfaces resulted in an indefinitely stable colloid of ferromagnetic particles (a ferrofluid). By contrast,  $Fe_3O_4$  ferrofluids, which tend to not be stable in acidic solutions, have been sterically stabilized by coating  $Fe_3O_4$  nanoparticles with oleic acid, poly(vinyl alcohol), or starch [43].

### (f) Precipitation of Oxides from Non-aqueous Solutions

Simple precipitation reactions are sometimes carried out in non-aqueous solvents. This method can be particularly advantageous when precipitating dissimilar metals that cannot be simultaneously precipitated from aqueous solution, due to large variations in the pH values necessary to induce precipitation of the constituent cations. Such is the case with  $LiCoO_2$ , a well-known cathode material for rechargeable lithium batteries [44].  $LiOH$  cannot be precipitated from aqueous solution, but its solubility in alcohols is greatly diminished. Hagenmuller *et al.* induced nearly simultaneous co-precipitation (of  $LiOH + Co(OH)_2$ ) by dripping a mixture of  $LiNO_3$  and  $Co(NO_3)_2$  dissolved in ethanol into a stirred 3 M KOH ethanol solution [45]. The hydroxide mixture was then calcined at 400-700 °C in air to yield 12-41 nm  $LiCoO_2$ .

There is at least one account of a nanoparticle oxide synthesis in which the solvent also served as the precipitating agent. Deb *et al.* prepared 5-20 nm  $\gamma$ - $Fe_2O_3$  by melting a mixture of stearic acid ( $CH_3(CH_2)_{16}COOH$ ) and hydrated  $Fe(NO_3)_3$  at 125 °C and calcining the product in air at 200 °C [46].

In other cases, the use of aqueous solvents is avoided, specifically to prevent the premature precipitation of metal hydroxides/oxides. Premature precipitation tends to be problematic with high-valence, electropositive metals such as  $\text{Ti}^{4+}$ ,  $\text{Zr}^{4+}$ , and so forth. This can, to some extent, be circumvented by using metal chloride or metal alkoxide precursors in non-aqueous solvents. The hydrolysis reactions can consequently be controlled to limit particle growth and prevent agglomeration. Ferroelectric  $\text{BaTiO}_3$ , for instance, has been prepared by precipitating a mixed-metal alkoxide precursor,  $\text{BaTi}(\text{O}_2\text{C}(\text{CH}_3)_6\text{CH}_3)[\text{OCH}(\text{CH}_3)_2]_5$  (which is highly susceptible to hydrolysis) with  $\text{H}_2\text{O}_2$  in diphenyl ether solution with oleic acid as stabilizer [47]. The addition of  $\text{H}_2\text{O}_2$  effectively initiates a hydrolysis reaction. Condensation occurred as the solution was heated at 100 °C, resulting in Ba-O-Ti linkages, but with particle growth constrained by the presence of the oleic acid stabilizer. This method resulted in 6-12 nm monodisperse, crystalline particles that did not require calcination.

The method of Caruntu *et al.* for the synthesis of colloidal ferrites is similar, in that a metal chelate precursor formed between a metal chloride and diethylene glycol was subsequently subjected to controlled hydrolysis [48]. Here, the diethylene glycol served as both solvent and stabilizing agent, although the glycol was usually exchanged for oleic or myristic acid to ensure growth termination. The authors have prepared a series of monodispersed  $\text{MFe}_2\text{O}_4$  ferrites by this method, where M = Mn, Fe, Co, Ni, or Zn, exhibiting sizes in the 3-7 nm range, with the standard deviation of the particle sizes typically on the order of 15%.

### (g) Microwave-Assisted Co-precipitation

The microwave processing of nanoparticles results in rapid heating of the reaction mixtures, particularly those containing water. As a consequence, the precipitation of particles from such solutions tends to be rapid and nearly simultaneous. This leads to very small particle sizes and narrow size distributions within the products. The method offers the additional benefit of requiring very short reaction times.

Pastoriza-Santos and Liz-Marzan were able to make a direct comparison of colloidal Ag and Au nanoparticles prepared by both reflux-induced precipitation and microwave-assisted precipitation. In both cases, the metals were reduced by the solvent, DMF [49]. They found that, generally, the microwave method offered better control of particle size and morphology.

Many colloidal metals can be prepared by microwaving mixtures of metal salts and polyalcohols. This method, originally developed by Fievet *et al.* [50], is now referred to as the microwave-polyol process. Recently, Yu *et al.* prepared 2-4 nm colloidal Pt particles by irradiating a mixture of poly(N-vinyl-2-pyrrolidone), aqueous  $\text{H}_2\text{PtCl}_6$ , ethylene glycol, and NaOH with 2450 MHz microwaves in an open beaker for 30 s [51]. Tsuji *et al.* have prepared PVP-stabilized, nanoparticulate Ni in ethylene glycol by a similar method [52]. Tu *et al.* adapted the method to a continuous-flow reactor [53]. This method can reportedly produce colloidal  $\sim 1.5$  nm Pt at 0.8 L/h.

Microwave methods have been used for the synthesis of chalcogenides. Gedanken *et al.* prepared CdSe, PbSe, and Cu<sub>2-x</sub>Se nanoparticles by microwave-refluxing [54] solutions containing aqueous Cd<sup>2+</sup>, Pb<sup>2+</sup>, or Cu<sup>2+</sup> and Na<sub>2</sub>SeSO<sub>3</sub> in the presence of an amine-based stabilizer [55]. In the case of CdSe, increased irradiation time influenced the structure of the product. Interestingly, the as-prepared CdSe samples consisted of well-dispersed 4-5 nm particles, whereas the PbSe and Cu<sub>2-x</sub>Se formed aggregates. Gedanken's group has published extensively on various oxides and chalcogenides prepared by microwave-assisted irradiation [56-59].

### (j) Sonication-Assisted Co-precipitation

Like microwave-induced heating, sonication of a liquid also results in rapid heating, although the mechanism is fundamentally different. The sonication of a liquid results in cavitation (the implosive collapse of bubbles), which creates localized "hot spots" with an effective temperatures of 5000 K and lifetimes on the order of a few nanoseconds or less [60, 61]. As such, the chemical reactions largely take place inside the bubbles [62]. The extremely rapid cooling rates encountered in this process, however, strongly favor the formation of amorphous products.

Many of the methods reported in the literature for sonochemical syntheses of nanoparticles involve the decomposition of carbonyl precursors. Suslick *et al.*, who have published extensively on the use of ultrasound in chemical syntheses, have prepared amorphous, nanoparticulate Fe, Co, and several Fe-Co alloys [63-65]. Typically, the

corresponding metal carbonyls were dissolved in decane and irradiated at 20 kHz for ~3 h under an inert atmosphere to produce well-dispersed ~8 nm particles. Others have reported the synthesis of 40 nm particles of M50 steel by a similar process [66].

Oxides can be prepared by similar methods if the sonication is performed under an oxygen atmosphere. Shafi *et al.* prepared amorphous nanoparticles of  $\text{NiFe}_2\text{O}_4$  by sonicating a solution of  $\text{Fe}(\text{CO})_5$  and  $\text{Ni}(\text{CO})_4$  in Decalin under a 1-1.5 atm pressure of  $\text{O}_2$ , although the products were agglomerated [67].

In some cases, the use of carbonyl precursors is not necessary.  $\text{ZrO}_2$ , for instance, has been precipitated by ultrasonic irradiation of an aqueous solution containing  $\text{Zr}(\text{NO}_3)_4$  and  $\text{NH}_4\text{OH}$ , followed by calcination at 300-1200 °C to improve the crystallinity or, for temperatures of 800 °C and above, to induce a tetragonal  $\rightarrow$  monoclinic phase transition [68]. Nanoparticulate, perovskite-structured  $\text{La}_{1-x}\text{Sr}_x\text{MnO}_3$  has been similarly prepared [69].

Zheng *et al.* have developed an interesting variation of this method, in which 100-200 nm hollow spheres of CdSe have been precipitated by ultrasonic irradiation of a solution of  $\text{Na}_2\text{SeO}_3$  and  $\text{CdCl}_2$  in the presence of sodium dodecyl sulfate (SDS), an anionic surfactant that serves as a vesicle template [70].

### **2.1.2 Microemulsion synthetic methods**

Hoar and Schulman noted in 1943 that certain combinations of water, oil, surfactant, and an alcohol- or amine-based co-surfactant produced clear, seemingly homogeneous solutions that Schulman termed "microemulsions." [71] The oil phases, in this case, were simple long-chain hydrocarbons, and the surfactants were long-chain organic molecules with a hydrophilic head (usually an ionic sulfate or quarternary amine) and a lipophilic tail. The surfactant in Schulman's study was cetyltrimethylammonium bromide (CTAB), which is still used extensively today.

The amphiphilic nature of the surfactants such as CTAB makes them miscible in both hydrocarbons and water, but when the surfactant is mixed with a hydrocarbon, the resulting mixture, although optically isotropic, cannot be properly described as a solution. As noted by Schulman, the orientation of the surfactant molecules is not random [72]. Instead, the surfactant, through ion-dipole interactions with the polar co-surfactant, forms spherical aggregates in which the polar (ionic) ends of the surfactant molecules orient toward the center. The co-surfactant acts as an electronegative "spacer" that minimizes repulsions between the positively charged surfactant heads. The addition of water to the system will cause the aggregates to expand from the center as the water molecules (again as a result of ion-dipole and dipole-dipole interactions) position themselves at the center of the sphere.

#### **(a) Synthesis of Metals by Reduction**

When a reverse micelle solution contains a dissolved metal salt and a second reverse micelle solution containing a suitable reducing agent is added, the metal cations can be reduced to the metallic state. Such reactions are, for all practical purposes, identical to those discussed in section 2.1.1 for the precipitation of metals from aqueous solutions. Although the number of metals that can be prepared this way is somewhat limited by the aqueous nature of the reactions, this approach has garnered much attention due to the potential application of the products as catalysts [3].

The reducing agent must be stable in an aqueous environment and not react with the other components of the reverse micelle system. This immediately excludes all non-aqueous reducing agents. Since bubbled  $H_2$  gas results in slow reduction kinetics for many metals, particularly at room temperature [3], sodium borohydride and hydrazine (usually in the form of water-soluble  $N_2H_4 \cdot 2HCl$  or  $N_2H_4 \cdot H_2O$ ) are most commonly employed in such reactions.

Lisiecki and Pileni adapted the technique to the reduction of  $Cu^{2+}$  with hydrazine and  $NaBH_4$ , but they started from a  $Cu(AOT)_2$  precursor [73, 74]. This technique is advantageous in that the  $NO_3^-$  counterions can be removed from the precursor, thereby avoiding any potential interference. Using hydrazine as the reducing agent, Lisiecki and Pileni obtained 2-10 nm Cu particles, whereas borohydride resulted in particles 20-28 nm in size.

### (b) Synthesis of Alloys by Reduction

Substitutional alloys can similarly be prepared if salts of different metals are dissolved in the reverse micelle solution prior to reduction, provided that the two metals are miscible in the metallic state. Reverse micelle solutions containing both  $\text{Fe}^{2+}$  and  $\text{Pt}^{2+}$ , for example, have been reported as being simultaneously reduced with  $\text{BH}_4^-$  [75]. Variation of the Fe/Pt ratio resulted in FePt,  $\text{Fe}_2\text{Pt}$ , disordered  $\text{FePt}_3$ , or ordered  $\text{FePt}_3$  [75, 76].

### (c) Synthesis of Metal Oxides

The synthesis of oxides from reverse micelles relies on the co-precipitation of one or more metal ions and is similar in most respects to the precipitation of oxides from aqueous solutions. Typically, precipitation of hydroxides is induced by addition of a reverse micelle solution containing dilute  $\text{NH}_4\text{OH}$  to a reverse micelle solution containing aqueous metal ions in the micellar cores. Alternatively, dilute  $\text{NH}_4\text{OH}$  can simply be added directly to a micelle solution of the metal ions. The precipitation of the metal hydroxides is typically followed by centrifugation and heating to remove water and/or improve crystallinity. This technique has proven particularly useful in preparing mixed-metal ferrites [77]. The oxidation of  $\text{Fe}^{2+} \rightarrow \text{Fe}^{3+}$  results from the reaction being performed under air, although other authors prefer to use  $\text{Fe}^{3+}$  as a starting material [78]. The products are typically on the order of 10-20 nm in diameter. Zhang *et al.* have recently demonstrated that, at least in the case of  $\text{MnFe}_2\text{O}_4$ , the cation distribution within the spinel structure of oxides prepared this way exhibits strong temperature dependence [79].

In some instances, as with co-precipitation reactions, microemulsions are used to prepare precursors that are decomposed to the desired phase by subsequent calcination, although this will inevitably result in some degree of agglomeration. Yener and Giesche prepared a series of mixed-metal ferrites by precipitating the precursors in a H<sub>2</sub>O-AOT-isooctane system and calcining the products at 300-600 °C [80]. Kumar *et al.* prepared 10 nm particles of YBa<sub>2</sub>Cu<sub>3</sub>O<sub>7-δ</sub> superconductor by combining a micellar solution of Y<sup>3+</sup>, Ba<sup>2+</sup>, and Cu<sup>2+</sup> prepared in an Igepal CO-430-cyclohexane system with a second micellar solution containing oxalic acid in the aqueous cores [81]. The precipitate was collected by centrifugation and calcined at 800 °C to decompose the oxalate precursors. Nanoparticulate Al<sub>2</sub>O<sub>3</sub> [82], LaMnO<sub>3</sub> [83], BaFe<sub>12</sub>O<sub>19</sub> [84], Cu<sub>2</sub>L<sub>2</sub>O<sub>5</sub> (L = Ho, Er) [85], and LiNi<sub>0.8</sub>Co<sub>0.2</sub>O<sub>2</sub> [86] are among the oxides that have recently been prepared by similar processes. The BaFe<sub>12</sub>O<sub>19</sub> prepared in this way is noteworthy in that it exhibits a higher coercivity and saturation magnetization than samples prepared by the traditional co-precipitation route [87].

### 2.1.3 Other synthetic methods

#### (a) Principles of Hydrothermal and Solvothermal Processing

In a sealed vessel (bomb, autoclave, etc.), solvents can be brought to temperatures well above their boiling points by the increase in autogenous pressures resulting from heating. Performing a chemical reaction under such conditions is referred to as solvothermal processing or, in the case of water as solvent, hydrothermal processing. Review articles devoted specifically to these methods appear frequently in the literature [88, 89].

The critical point for water lies at 374 °C and 218 atm. Above this temperature and pressure, water is said to be supercritical. Supercritical fluids exhibit characteristics of both a liquid and a gas: the interfaces of solids and supercritical fluids lack surface tension, yet supercritical fluids exhibit high viscosities and easily dissolve chemical compounds that would otherwise exhibit very low solubilities under ambient conditions.

Some solvothermal processes indeed involve supercritical solvents. Most, however, simply take advantage of the increased solubility and reactivity of metal salts and complexes at elevated temperatures and pressures without bringing the solvent to its critical point. In any event, solvothermal processing allows many inorganic materials to be prepared at temperatures substantially below those required by traditional solid-state reactions. Unlike the cases of co-precipitation and sol-gel methods, which also allow for substantially reduced reaction temperatures, the products of solvothermal reactions are usually crystalline and do not require post-annealing treatments.

As a matter of safety, the pressures generated in a sealed vessel should always be estimated beforehand. The equations necessary for doing so go far beyond the ideal gas law and are outlined in the review by Rajamathi and Seshadri [88].

### (b) Templated Syntheses

The synthesis of nanoparticles on templates has garnered an increasing amount of attention in the past few years. As will be discussed here, this approach encompasses a broad array of synthetic strategies and frequently involves methods that are best described as hybrids between previously discussed techniques.

The technique of heterogeneous nucleation, in which "seed" crystals serve as nucleation sites for further deposition and growth of crystallites, can essentially be considered one of the simpler forms of templated synthesis. This technique can be used to increase the average particle size of nanoparticles, such as when aqueous  $\text{Au}^{3+}$  is deposited on colloidal Au, or  $\text{Ag}^+$  is deposited on colloidal Ag [90, 91]. The method can also be used for the synthesis of core-shell and onion structures, such as the deposition of Pd, Bi, Sn, or In on colloidal Au [92, 93], Au on  $\text{TiO}_2$  [94], ZnO on  $\text{Al}_2\text{O}_3$  [95], or CdS on HgTe [96]. Pileni has recently reviewed these methods [97].

To maintain the narrow size distribution of the nanoparticles, care must be taken to ensure that smaller particles do not nucleate from solution during the deposition process. Several new techniques have recently emerged to prevent this occurrence. Brown *et al.* used hydroxylamine ( $\text{NH}_2\text{OH}$ ) for the seed-mediated growth of colloidal Au, increasing the average particle diameter from 12 nm up to 50 nm [98]. The use of hydroxylamine is critical to this process. While hydroxylamine can theoretically reduce  $\text{AuCl}_4^-$  to  $\text{Au}^0$ , the reduction kinetics of this process is greatly enhanced in the presence of the colloidal Au seed particles, in which the Au surfaces serve as catalysts. The reduction of  $\text{AuCl}_4^-$  therefore preferentially occurs at the Au surfaces, as opposed to leading to the nucleation

of new, smaller Au particles from solution. Taking the process one step further, Schmid *et al.* deposited ~9 nm thick Pt and Pd shells on 18 nm colloidal Au particles from solutions of  $\text{HtPtCl}_2$  or  $\text{H}_2\text{PdCl}_4$ , using hydroxylamine hydrochloride ( $\text{NH}_2\text{OH}\cdot\text{HCl}$ ) as the reducing agent and  $\text{p-H}_2\text{NC}_6\text{H}_5\text{SO}_3^-\text{Na}^+$  as a stabilizer [92].

### (c) Biomimetic Syntheses

Interest in biotemplated nanoparticle syntheses was spurred dramatically when Meldrum *et al.* reported the synthesis of nanometric iron sulfide and amorphous manganese and uranyl oxides within protein cages [99]. The ferritin-containing protein cages were, in effect, serving as nanoreactors to constrain particle growth. Douglas and Young later reported the similar host-guest encapsulation of paratungstate and decavanadate inside the protein cage of a virus [100]. Research along these lines continues, now involving the protein engineering of viral cages as tailored nanoreactors [101].

Much of the recent interest in biological nanoparticle synthesis is based on the molecular self-assembly of nanoparticles. Most of this work stems from the 1996 report by Mirkin *et al.*, who demonstrated that functionalized DNA is capable of directing the self-assembly of Au nanostructures into regularly spaced 2-D arrays [102]. This line of research continues at a rapid pace [103-106], and review articles appear frequently [107, 108].

Seidel *et al.* were recently able to induce the nucleation and growth of Pt nanoparticles on single DNA molecules [109]. In this case,  $\lambda$ -DNA was aged in a  $K_2PtCl_4$  solution, followed by the addition of dimethylamine borane as a reducing agent. The DNA molecules effectively served as a heterogeneous nucleating agent and template for the formation of nanoparticulate Pt chains. Through an impressive application of scanning force microscopy (SFM), the researchers were able to observe the formation of the Pt particles on the biomolecules *in situ*. Similarly, Dujardin *et al.* used the tobacco mosaic virus as a template for the growth of <10 nm Pt, Au, and Ag nanoparticles into cylindrical aggregates [110].

### (d) Sol-Gel Process

The sol-gel process can be characterized by a series of distinct steps.

Step 1: Formation of a stable solution of the alkoxide or solvated metal precursor (the sol). Step 2: Gelation resulting from the formation of an oxide- or alcohol-bridged network (the gel) by a polycondensation or polyesterification reaction that results in a dramatic increase in the viscosity of the solution. If so desired, the gel may be cast into a mold during this step. Step 3: Aging of the gel (syneresis), during which the polycondensation reactions continue until the gel transforms into a solid mass, accompanied by contraction of the gel network and expulsion of solvent from the gel pores. Ostwald ripening and phase transformations may occur concurrently with syneresis. The aging process of gels can exceed 7 days and is critical to the prevention of cracks in gels that have been cast. Step 4: Drying of the gel, so that water and other volatile liquids are removed from the gel network. This process is complicated due to

fundamental changes in the structure of the gel. The drying process has itself been broken into four distinct steps [111]: (i) the constant rate period, (ii) the critical point, (iii) the first falling rate period, and (iv) the second falling rate period. If isolated by thermal evaporation, the resulting monolith is termed a xerogel. If the solvent is extracted under supercritical or near-supercritical conditions, the product is an aerogel. Step 5: Dehydration, during which surface-bound M-OH groups are removed, thereby stabilizing the gel against rehydration. This is normally achieved by calcining the monolith at temperatures up to 800 °C. Step 6: Densification and decomposition of the gel at high temperatures ( $T > 800$  °C). The pores of the gel network are collapsed, and remaining organic species are volatilized. This step is normally reserved for the preparation of dense ceramics or glasses.

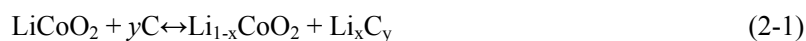
### **2.2 Lithium ion rechargeable batteries and anode materials**

The lithium battery industry is undergoing rapid expansion, now representing the largest segment of the portable battery industry and dominating the laptop, cell phone, and camera power source industry. The principal features of the lithium ion battery are as follows: (1) high energy density (both gravimetric and volumetric), (2) high operating voltage, (3) low self-discharge rate, (4) no memory effect, (5) high drain capability, (6) wide operating temperature range, and (7) quick charge acceptance. These excellent characteristics have enabled the lithium ion battery market to advance with such rapid strides [112].

### 2.2.1. Lithium ion rechargeable batteries and anodes

In its most common configuration, a lithium ion battery consists of a graphite anode, a lithium metal oxide (e.g.  $\text{LiCoO}_2$ ) cathode, and a separator soaked in a liquid solution of a lithium salt (e.g.  $\text{LiPF}_6$ ) in an organic solvent mixture (e.g. an ethylene carbonate-dimethylcarbonate, EC-DMC mixture). The batteries are light, compact, and have an operational voltage averaging 3.5 V, with an energy density that, according to the structure, ranges from 150 Wh/kg up to ~250 Wh/kg [113].

Lithium metal negative electrode has serious problems in secondary battery use, since it does not have a long enough cycle life and there are safety aspects that need to be considered, due to the dendrite formation on the surface of lithium metal electrode during charge/discharge cycling. In order to solve these problems a "rocking-chair" concept has been established, in which the intercalation phenomenon has been used for the anode reaction in lithium ion secondary batteries [114]. Graphite has a layered structure that, as is well known, can be intercalated or doped with different atoms and atomic groups between the layers to form so-called graphite intercalation compounds (GIC) [115]. The theoretical lithium storage capacity of a graphite anode for a Li ion secondary battery has been considered to be  $372 \text{ mAh g}^{-1}$ , corresponding to the first stage  $\text{LiC}_6$ -GIC. The charge/discharge total reactions and the anode reaction based on  $\text{Li}^+$  intercalation and de-intercalation are shown as follows:



Various types of carbonaceous materials ranging from highly ordered graphites to disordered carbons have been investigated experimentally and theoretically as potential anode materials. Investigations have focused on improving the specific capacity, cycling efficiency, and cycling lifetime of the energy storage devices. The microstructure and morphology of the lithium ion battery anode material must be controlled for practical devices. It is well known that the performance of lithium ion batteries depends strongly on the thermal history and morphology of the carbon and graphite materials used for the anode [116]. A great deal of effort has been devoted to the identification of the key parameters of the carbon and graphite materials used for the battery. Because carbon and graphite materials have large variations in their microstructure, texture, crystallinity, and morphology, it has been important to design and choose the anode material from a wide variety in order to get better battery performance. Two typical types of carbon materials, highly-ordered graphite, heat-treated at high temperatures such as 3000°C, and non-graphitizable carbon, heat-treated at low temperatures such as 1100°C, have been used in the anode in commercial batteries.

New lithium ion battery configurations assuring an increase in capacity, in safety, and in energy and power density, as well as in compatibility with the environment are urgently required. Many industrial and academic laboratories are involved in this race. The main goals of the research are the replacement of: (1) graphite with alternative, higher capacity anode materials, (2) lithium cobalt oxide with lower cost and more environmentally benign cathode materials, and (3) the organic liquid electrolyte with a more reliable polymer electrolyte. In this study, the author has mainly focused on the alternative tin based anode materials for lithium ion batteries.

### 2.2.2. Tin based anode materials

In 1995, FUJI Photofilm was granted a patent [117] in which the use of an alternative anode material was proposed. The starting electrode material was a non-crystalline solid: tin-based composite oxide (TCO). The stoichiometry of this solid is  $\text{SnM}_x\text{O}_y$ , where M is the vitrifying element (B(III), P(V), As(III)), and  $x \geq 1$ ). A typical composition is TCO-1,  $\text{Sn}_{1.0}\text{B}_{0.56}\text{P}_{0.40}\text{Al}_{0.42}\text{O}_{3.6}$ , which can be obtained by a reaction of SnO,  $\text{B}_2\text{O}_3$ ,  $\text{SnP}_2\text{O}_7$ , and  $\text{Al}_2\text{O}_3$  at 1100 °C, followed by quenching to yield a yellowish, transparent glass. The electrochemical activity of these solids was first described by assuming that Sn(II) behaves as the electroactive element for lithium insertion, while the other elements form a  $-\text{M}-\text{O}-$  network that expands isotropically, allowing the dispersion of the Sn(II) centers as well as  $\text{Li}^+$  diffusion. Reversible capacities larger than  $600 \text{ mAh g}^{-1}$  and  $2200 \text{ Ah l}^{-1}$  were described, which are significantly higher than  $372 \text{ mAh g}^{-1}$  and double the volumetric capacity of the best carbon-based material ( $\sim 1200 \text{ Ah l}^{-1}$ ), respectively.

Since then, a renewed interest in tin and tin alloys and compounds has grown. Many research papers have been devoted to the study of different crystalline and non-crystalline tin compounds as starting materials. Moreover, the mechanism of the reaction previously described has been revised. Two different approaches to understanding the mechanism of the reactions with lithium of different tin compounds can be distinguished in the literature: (i) mechanical dispersion of electroactive Li–Sn alloys, while the other elements are mere "spectators" [118] of the Li–Sn system; (ii) deeper interactions between the dispersing matrix and the Sn atoms. The latter approach

has been reinforced by the application of different spectroscopic techniques, some of them highly specific to tin, such as  $^{119}\text{Sn}$  Mössbauer spectroscopy. It should be noted that due to the non-crystalline structure of many products of the reaction with lithium, X-ray diffraction techniques are less useful for illuminating the mechanism of the reaction. Some examples of the compounds which have been studied so far include  $\text{SnO}$ ,  $\text{SnO}_2$ ,  $\text{SnP}_2\text{O}_7$ ,  $\text{SnHPO}_4$ ,  $\text{SnPO}_4\text{Cl}$ ,  $\text{SnSiO}_3$ ,  $\text{SnBPO}_6$ ,  $\text{Sn}(\text{C}_2\text{O}_4)$ ,  $\text{SnSO}_4$ , etc. Some of them are discussed in the following sections.

Crystalline tin monoxide possesses a layered structure in which  $\text{Sn-O-Sn}$  slabs are stacked together so that tin atoms protrude from both sides of the oxygen layers. This oxide was one of the first materials to be tested [119] after the FUJI patent. The first discharge curve of lithium cells using  $\text{SnO}$  as the active electrode material shows a complex multistep shape that could be simply ascribed to  $\text{Sn(II)}$  to  $\text{Sn(0)}$  reduction with  $\text{Li}_2\text{O}$  formation, followed by the formation of  $\text{Li-Sn}$  phases, and ending with the approximate " $\text{Li}_{4.4}\text{Sn}$ " composition. The reversible capacity on charge should then correspond to the formation of intermediate  $\text{Li-Sn}$  compositions and finally tin metal. An irreversible capacity of  $2\text{Li/SnO}$  is then expected after the first charge. However, some extra irreversible capacity is detected, as a result of the formation of a passivating layer during the first steps of the discharge [120]. X-ray diffraction studies partially agree with the simplified hypothesis, as some reflections ascribable to  $\beta\text{-Sn}$  and  $\text{Li-Sn}$  phases are visible as low intensity broadened profiles [121]. However, the quality of the diffraction effects resulting from small crystallite size and/or imperfections prevents a clear picture.  $^{119}\text{Sn}$  Mössbauer spectroscopy has proven particularly sensitive to the oxidation states and the environments of tin in  $\text{Li/SnO}$  cells. Thus, the formation of tin

and Li–Sn alloys close to the nominal phases has been qualitatively confirmed. However, it has also been confirmed that SnO is formed during charge of the cell for lithium content lower than 2Li/Sn [122].

Tin dioxide was also soon considered as electrode material [119]. Considering the electrode behavior of SnO<sub>2</sub> as compared with the monoxide, the initial first discharge capacity of the cells, 8.4Li/Sn ( $\sim 1220 \text{ Ah kg}^{-1}$ ), involves two main steps: total reduction of tin and the formation of a lithium–tin intermetallic. Thus, the values for irreversible capacity are higher than in SnO, as expected, while reversibility is restricted to 4.4Li/Sn, after complete reduction to tin metal ( $\sim 600 \text{ Ah kg}^{-1}$  of observed reversible capacity). A particular topic of interest in tin dioxide research results from the different preparation routes described in the literature, as semiconducting tin dioxide films and ceramics are widely used as gas sensors. Thus, spray pyrolysis, sol–gel [123], and dip-coating [124] procedures have been used in the preparation of coatings and films, while the sol–gel route using inorganic hydrosols [125] and tin alkoxides has been used to obtain powdered material. The different textures and microstructures resulting from each synthesis route may play an important role in the electrochemical behavior and condition the ability of the oxide products to be used as the active anode material in lithium-ion batteries. Moreover, the conductivity of the oxide can be improved by doping with other elements, e.g. doping with Sb allows its use in stable electrodes for glass melting furnaces [123].

Amorphous tin-oxide films were prepared by spray pyrolysis of  $\text{SnCl}_2$  mixed with  $\text{CH}_3\text{COOH}$  and deposited onto a stainless steel substrate at a mild temperature ( $350^\circ\text{C}$ ) [126]. These films exhibit good charge/discharge properties over more than 100 cycles. Heating at  $600^\circ\text{C}$  causes significant changes in their surface composition, in term of the virtual disappearance of the tin component and the presence of oxygen-bound Fe. Under these conditions, the reversible capacity dramatically fades, and the cell behaves similarly to one made from uncoated substrate. Concerning thin-film  $\text{SnO}_2$  electrodes, Schleich and co-workers [127, 128] and Nam *et al.* [129] reported their preparation by chemical vapor deposition and electron beam evaporation, respectively. The resulting electrodes show good capacity retention on prolonged cycling. However, the problems associated with the poor adhesion of the films may limit cycling efficiency.

Recently, novel thin films of a few nanostructured carbon-free anode materials ( $\text{SnO}_2$ ,  $\text{Li}_2\text{O-SnO}_2$ ,  $\text{CuO-SnO}_2$ , and  $\text{Li}_2\text{O-CuO-SnO}_2$  composite) were prepared by the electrostatic spray deposition (ESD) technique [130]. As a new anode material for lithium ion batteries,  $\text{Li}_2\text{O-CuO-SnO}_2$  composite (molar ratio  $\text{Li/Cu/Sn} = 1:1:1$ ) film displayed the highest initial capacity ( $1158 \text{ mAh g}^{-1}$ ) and the lowest initial capacity loss (17.6%) at 0.5 C. It also showed excellent rate capability with an 8 C rate capacity of up to  $525 \text{ mAh g}^{-1}$ . The  $\text{Li}_2\text{O}$  and  $\text{CuO}$  components in the composite and the hollow porous structure were responsible for the excellent electrochemical performance.

Cobalt tin oxide ( $\text{CoSnO}_3$ ) was synthesized as a novel negative electrode material through the pyrolysis of  $\text{CoSn(OH)}_6$  precursor [131]. The product is amorphous and

composed of small square flakes, which have an average size of about 70 nm. The nanocomposite has an improved electrochemical performance compared with a ball-milled mixture of CoO and SnO<sub>2</sub>.

Tin pyrophosphate was studied in depth by Xiao *et al.* [132]. Amorphous Sn<sub>2</sub>P<sub>2</sub>O<sub>7</sub> was prepared by melt-quenching the crystalline form. The first discharge branch was described in a parallel way to the oxides discussed above, by tin reduction to the metal and Li–Sn alloy formation. The first difference is that two energetically different Li sites were detected in the crystalline material. A higher potential was required for complete Li-extraction, and then the reversible capacity (400 mAh g<sup>-1</sup>) was lower than in the amorphous solid (520 mAh g<sup>-1</sup>). In addition, the first evidence that the pyrophosphate groups were not mere spectators was obtained by IR spectroscopy. Thus, the dissociation  $\text{P}_2\text{O}_7^{2-} \rightarrow \text{PO}_4^{3-} + \text{PO}_3^-$  was proposed after repeated cycling. The presence of chlorine in the composition of tin(II) phosphate chloride does not affect tin reduction. The structure of Sn<sub>2</sub>PO<sub>4</sub>Cl resembles that of SnO, although the layers differ in composition, being –Sn–O–P–O–Sn–, while the chlorine atoms are located in the interlayer space. The phosphate group suffers limited changes on cycling, and the product after the first discharge can be then considered as a matrix of LiCl and Li<sub>3</sub>PO<sub>4</sub> that finely disperses Sn–Li alloys. Thus capacity retention stabilizes after a decrease during the first ten cycles, which is ascribable to an increase in the size of tin domains. The charge and discharge capacities remain close to 300 Ah kg<sup>-1</sup> (Sn) up to ~ 40 cycles [133], which is better retention for extended cycling than that found for polycrystalline SnO<sub>2</sub>.

A different behavior is found in tin hydrogen phosphate.  $\alpha$ - $\text{Sn}(\text{HPO}_4)_2 \cdot 2\text{H}_2\text{O}$  is known to show an extensive intercalation chemistry [134]. In contrast, the synthesis conditions and the characterization of  $\alpha$ - $\text{SnHPO}_4$  are less clearly resolved. A new soft chemistry precipitation route of  $\alpha$ - $\text{SnHPO}_4$  was recently described, and its interactions with lithium when used as electrode material were studied by X-ray diffraction (XRD) and  $^{31}\text{P}$  MAS NMR [135, 136].  $\text{Li}/\text{SnHPO}_4$  cells showed a capacity higher than  $1500 \text{ mAh g}^{-1} \text{ Sn}$  during the first discharge, but the reversible capacity was limited to  $\sim 200 \text{ mAh g}^{-1} \text{ Sn}$  after 25 cycles working at  $40^\circ\text{C}$ . The large theoretical irreversible capacity of  $3\text{Li}/\text{Sn}$  suggests that the hydrogen reduction took place during the first discharge. A step by step characterization of the Li-network interaction agreed with this hypothesis. Besides formation of  $\text{Li}_3\text{PO}_4$ ,  $^7\text{Li}$  NMR signals gave evidence of lithium–tin alloys with a high level of dispersion and negligible Knight shift [136].

Among tin salts without phosphorous in their composition, tin(II) oxalate offers interesting possibilities, as it can be used as a precursor for the preparation of ultra-fine  $\text{SnO}_2$  by chemical and thermal reactions, as well as an active electrode material because of the "in situ" electrochemical reaction with lithium [137]. Good cycling behavior was found by using tin(II) oxalate directly to prepare the electrodes in lithium test cells. This fact may be indicative of the good dispersion effect of the redox decomposition process in the oxalate salt. On the other hand, thermogravimetric analysis of tin(II) oxalate in air shows a single weight loss in a narrow temperature range around  $350^\circ\text{C}$ , whose magnitude agrees fairly well with the reaction  $\text{SnC}_2\text{O}_4 \rightarrow \text{SnO}_2 + 2\text{CO}$ . The XRD patterns and Fourier transform IR (FTIR) spectroscopy of the thermally decomposed products were basically characteristic of tin dioxide with a rutile-type structure. A chemical

method to convert the precursor into tin oxide was also reported. In this case, tin oxalate powder was dissolved in aqueous hydrogen peroxide (33%) at room temperature. The clean solution was smoothly heated with stirring. Parallel to water evaporation, white colloidal product precipitates were formed. The continuous heating provoked the dehydration of the compound until a white solid product was obtained. The X-ray diffraction patterns recorded for the pristine material showed several broadened diffraction maxima, which are coincident with the more intense reflections of rutile-type  $\text{SnO}_2$ . The products obtained by heating the former solid in air at different temperatures show a continuous decrease in line broadening with the heating temperature, which implies an expected progressive augmentation of the size of the particle domains. The electrochemical behavior of "ex-oxalate" tin dioxide cells revealed only two signals in the first reduction. The capacity of the first discharge reached  $\sim 1600 \text{ mAh g}^{-1}$ , and a reversible capacity of  $\sim 750 \text{ mAh g}^{-1}$  was achieved in the first cycle. The good reproducibility of the curve shape, from cycles 2–5, was taken as indicative of the homogeneity in the redox reaction, probably caused by the good dispersion effects originating from the initial irreversible processes on the tin alloy particles. Other P-free salts already studied in the literature include tin(II) sulfate. For the electrochemical reaction of  $\text{SnSO}_4$  with lithium, a two step mechanism (reduction to metallic tin in the first reaction and  $\text{Li}_4\text{Sn}$  after the second cycle) has also been proposed, which is supported by Mössbauer data [138].

## 2.3 Direct methanol fuel cells and electrocatalysts

Fuel cells, energy converting devices with a high efficiency and low/zero emissions, have been attracting more and more attention in recent decades due to high energy demands, fossil fuel depletion, and environmental pollution throughout the world. For hydrogen gas fed fuel cells at their current technological stage, hydrogen production, storage, and transportation are the major challenges, in addition to cost, reliability and durability issues. Direct methanol fuel cells (DMFCs), using liquid and renewable methanol fuel, have been considered to be a favorable option in terms of fuel usage and feed strategies [139, 140]. Compared to hydrogen-fed fuel cells, which have a reforming unit, or low capacity in the hydrogen storage tank, DMFC uses liquid methanol fuel, which is easily stored and transported, and simplifies the fuel cell system.

### 2.3.1 Direct methanol fuel cells

The direct methanol fuel cell (DMFC) uses methanol, in either a vapour or liquid form, as the fuel and operates at relatively low temperatures (<100 °C) [141]. The cell reactions are:



which can be combined and give the overall reaction:



Thus, the overall cell reaction is the combustion of methanol to carbon dioxide and water. The structure of the DMFC consists of two porous electrocatalytic electrodes on either side of a solid polymer electrolyte membrane. The thermodynamic reversible potential for the overall cell reaction is 1.214 V, which compares favorably to 1.23 V for the hydrogen fuel cell and, consequently, has generated interest in the DMFC as an alternative power source.

However, a current advantage of the hydrogen cell over the DMFC is that hydrogen oxidation at the anode is very fast and, consequently, the performance of the hydrogen cell is better than that of the methanol cell. For methanol, six electrons must be exchanged for complete oxidation, so that the oxidation kinetics is inherently slower, as a result of intermediates formed during methanol oxidation.

In the research and development of the DMFC and similar organic fed fuel cells, there are several issues which have to be addressed, which include thermal management, gas management, methanol fuel management and hydrodynamics, and mass transport. Methanol crossover [142] results in a mixed potential at the cathode with significant loss in oxygen reduction performance. It has been recognized that the success of fuel cell technology depends largely on two key materials: the membrane and the electrocatalyst. These two key materials are also directly linked to the major challenges faced in DMFCs, including (1) methanol crossover, which can only be overcome by developing new membranes and a new cathode catalyst that tolerates the presence of methanol; and (2) slow anode kinetics, which can only be overcome by developing new anode catalysts.

With regard to new DMFC anode catalysts, there are two major challenges, namely, the performance, including activity, reliability, and durability, and cost reduction.

### **2.3.2 Electrocatalysts for direct methanol fuel cells**

In recent years, Pt–Ru catalyst has been one of the major topics in DMFC anode catalyst exploration [143]. The Pt–Ru catalyst has been supported on some high-surface-area materials, such as carbon particles, in order to achieve high dispersion and maximum utilization, as well as to avoid catalyst agglomeration during the fuel cell operation. Platinum supported on carbon is generally used as the electrocatalyst for cathodes [144], with Pt having the highest catalytic activity towards the oxygen reduction reaction (ORR) of any of the pure metals. Alloy catalysts of platinum with various transition metals have been employed to improve the catalytic activity and to reduce the cost. Many approaches have been reported for Pt catalytic activity enhancement towards ORR in fuel cell applications [145-147]. In particular, the Pt–transition metal alloys have attracted much interest due to their enhanced catalytic activities towards ORR in direct methanol fuel cell development. The common criteria for a high performance catalyst are: (1) a narrow nanoscale size distribution; (2) a uniform composition throughout the nanoparticles; (3) a fully alloyed nature; (4) and high dispersion on carbon support. According to these criteria, some innovative and cost-effective preparation methods have been developed and show promise for attaining performance optimization by controlling the synthetic procedures and conditions. There are three important methods for preparing

carbon-supported Pt based catalysts, including the impregnation method, the colloidal method, and the microemulsion method.

### (a) The impregnation method

Of those three methods, the impregnation method is the most widely used, and is a simple and straightforward chemical preparation technique for Pt based catalyst preparation [148-152]. The impregnation method includes an impregnation step, followed by a reduction step. During the impregnation step, metal precursors are mixed with high-surface-area carbon black in aqueous solution to form a homogeneous mixture. As a catalyst support, carbon black plays a major role in terms of penetrating and wetting the precursors, and it can also limit nanoparticle growth. The chemical reduction step can be carried out by liquid phase reduction using  $\text{Na}_2\text{S}_2\text{O}_3$ ,  $\text{NaBH}_4$ ,  $\text{Na}_4\text{S}_2\text{O}_5$ ,  $\text{N}_2\text{H}_4$  or formic acid as the reductive agent, or gas phase reduction using a flowing hydrogen stream as the reductive agent at elevated temperature.

During the impregnation process, many factors can affect the composition, morphology and dispersion of Pt based catalyst, resulting in the variation of catalytic activity. The porosity of the carbon black support can effectively control the catalyst nanoparticle size and dispersion, which will be discussed in the next section. Many studies have indicated that the synthetic conditions, such as the nature of the metal precursors used, the reduction method, and the heating temperature, are also crucial in the impregnation

process [148, 151, 152]. Generally, metal chloride salts (e.g.,  $\text{H}_2\text{PtCl}_6$  and  $\text{RuCl}_3$ ) are commonly used as precursors in the impregnation–reduction process due to their easy availability.

### (b) The colloidal method

The colloidal method is another extensively explored preparation route for Pt based electrocatalyst [153-159]. Usually, the colloidal method includes the following common steps: (1) preparation of Pt-containing colloids; (2) deposition of the colloids onto the carbon support; and (3) chemical reduction of the mixture.

Watanabe *et al.* [153] reported a preparation procedure for a highly dispersed Pt–Ru catalyst through co-deposition of colloidal Pt and Ru oxides on carbon in aqueous media, followed by a reduction with bubbling hydrogen. A modified Watanabe route using metal sulphite slats, with a final thermal treatment in an  $\text{H}_2$  atmosphere was successful in producing a catalyst with better performance [154, 155]. This metal oxide colloid route can result in the preparation of a Pt–Ru catalyst with a much higher specific surface area compared with that resulting from the conventional impregnation method. However, the particle growth and agglomeration control in this route seem to be problematic.

Other colloid routes using various reducing agents, organic stabilizers or shell-removing approaches have also been developed in recent years. Bensebaa *et al.* [156] reported the preparation of Pt–Ru nanoparticles using ethylene glycol as both a solvent and a reducing agent, with PVP as a stabilizer. Liu *et al.* [157] developed a glycol colloid route in which an organic stabilizer was unnecessary. Pt–Ru colloids were prepared in an ethylene glycol solution and subsequently transferred to a toluene medium with decanethiol as the phase transfer agent. The microwave method was used to remove the organic shell from these colloids [156, 157].

### (c) The microemulsion method

The microemulsion method is a new route for synthesizing Pt based catalysts that has been developed in recent years [160, 161]. In this method, the first step is the formation of Pt nanoparticles through a water-in-oil microemulsion reaction, followed by a reduction step. Here the microemulsion serves as a nanoscale reactor in which the chemical reaction takes place. The microemulsion is a nanoscale aqueous liquid droplet containing a noble metal precursor. The droplets are engulfed by surfactant molecules and uniformly dispersed in an immiscibly continuous organic phase. The reduction step can be carried out either by adding a reducing agent (e.g.,  $\text{N}_2\text{H}_4$ ,  $\text{HCHO}$ , or  $\text{NaBH}_4$ ) into the microemulsion system, or by mixing it with another reducing agent-containing microemulsion system. As a result, the reduction reaction is confined to the inside of the nanoscale microemulsion droplets, and the formed metal particle sizes can be easily controlled by the magnitude of the microemulsion droplet size. The surfactant molecules can function as protective agents to prevent the Pt nanoparticles from agglomerating.

The removal of the surfactant molecules can be easily carried out by heat-treating the high-surface-area carbon supported nanoparticles. Pt–Ru/C catalysts prepared by this method were found to exhibit higher activity than those commercially available for methanol oxidation in both an electrochemical half-cell containing sulphuric acid and methanol [161], and in a DMFC [160]. However, like the organometallic colloid method, the microemulsion method also uses costly surfactant molecules and requires a substantial number of separation and washing steps, which may be not suitable for large-scale production.

In addition to the impregnation, colloidal, and microemulsion methods, many other methods have also been applied to the preparation of carbon-supported fuel cell catalysts, e.g. the ion exchange method and the vapor phase method. Many fuel cell catalysts used in DMFC are multi-component systems, and alloying the components is necessary to give the maximum benefit. To achieve this with practical catalyst technology requires the use of flexible preparation routes. One straightforward way of preparing a bimetallic catalyst is to impregnate a second component on a preformed catalyst. Specific interactions can be induced by subsequent treatment of the catalyst. Component alloying can be induced by high-temperature heat treatment under either inert or reducing gas streams. This method has the disadvantage of particle sintering, resulting in a lower catalyst active area. Other methods involve the co-deposition of soluble metal salts using changes in pH or the addition of reducing agents. This has the advantage of forming bimetallic structures at low temperature and, hence, at high dispersion [144]. However, this approach is generally restricted to components with similar precipitation chemistry and/or ease of reduction to metals. As noted above, colloid methods have also been

applied to bimetallic catalysts. An alternative method of depositing a second metal on a preformed catalyst is the use of surface organometallic modification. In this approach, an organometallic precursor is reacted in a solvent with a preformed catalyst that has a layer of adsorbed  $H_2$ . This approach has the advantage that the precursor only reacts with the adsorbed hydride and therefore is only deposited on the active catalyst sites. The technique has been reported to be suitable for preparing Sn-, Ge-, and Mo-modified Pt catalysts [162-164].

### **2.3.3 Electrocatalyst supports**

In order to achieve fine dispersion, high utilization, and stable nanoscale metallic particles, catalyst-supporting strategies have been explored. Compared to bulk metal catalysts, supported catalysts show higher activity and stability. Carbon particles are frequently used as catalyst supports, because of their relative stability in both acidic and basic media, good electric conductivity, and high specific surface area. In the past, several carbon materials have been tested as catalyst supports for DMFCs. The carbon material has a strong influence on the properties of the supported noble metal catalyst, such as metal particle size, morphology, size distribution, degree of alloying, stability, and dispersion. On the other hand, carbon supports can also affect the performance of the properties of the supported catalysts in fuel cells, such as mass transport and catalyst layer electronic conductivity, electrochemical active area, and metal nanoparticle stability during operation. Hence, the optimization of carbon supports is very important in DMFC development. The properties of a suitable carbon support, such as specific surface area, porosity, morphology, surface functional groups, electronic conductivity, corrosion resistance, etc., must be carefully selected in order to make an active catalyst.

The properties of the carbon support materials have strong effects on the preparation procedures and performance of the synthesized supported catalysts. The physical and chemical origins of those effects are not fully understood yet, although considerable efforts have been made over the last two decades to optimize the supporting strategies in terms of theoretical and experimental approaches, especially in the DMFC area. In recent years numerous studies have concentrated on understanding the effects of carbon supports and exploring new carbon supports.

### (a). Carbon black

Carbon blacks are commonly used as supports for DMFC anode catalysts. There are many types of carbon black, such as Acetylene Black, Vulcan XC-72, Ketjen Black, etc., and these are usually manufactured by pyrolyzing hydrocarbons, such as natural gas or oil fractions taken from petroleum processing. These carbon blacks show different physical and chemical properties, such as specific surface area, porosity, electrical conductivity, and surface functionality. Among these factors, the specific surface area has a significant effect on the preparation and performance of supported catalysts [140, 165]. Generally, highly dispersed, supported catalysts cannot be prepared from low-surface-area carbon blacks (e.g., Acetylene Black). High-surface-area carbon blacks (e.g., Ketjen Black) could theoretically support highly dispersed catalyst nanoparticles. However, Ketjen Black supported catalysts showed high Ohmic resistance and mass transport limitations during fuel cell operation [140]. Vulcan XC-72, with a surface area of  $\sim 250 \text{ m}^2 \text{ g}^{-1}$ , has been widely used as a catalyst support, especially in DMFC electrocatalyst preparation. An accessible and sufficiently large surface for maximum catalyst dispersion has been argued to be a necessary, but not sufficient condition for obtaining optimized carbon supported catalysts. Other factors, such as pore size and

distribution, and the surface functional groups of carbon blacks, also affect the preparation and performance of carbon black supported catalysts [166-170]. For example, in a conventional impregnation process, a portion of the metal nanoparticles may have sunken into the micropores of Vulcan XC-72. This portion inside the micropores has less or no electrochemical activity, due to the difficulty in reactant accessibility. This is the major reason why some catalysts prepared by the impregnation method have not shown high activity, even when the metal loading is very high. By keeping the Pt nanoparticle size larger than the micropore size, Anderson *et al.* [167] found that the saturated weight loading of Pt onto Vulcan carbon by the colloid method was 9–10 wt.%, versus 10–40 wt.% by the impregnation method. Their results indicated that micropores which are smaller than the Pt nanoparticle size could effectively block the sinking in of the metal nanoparticles.

The contact between the metal nanoparticles and the Nafion micelles in the catalyst layer of the membrane electrode assembly (MEA) is also affected by the carbon support particle pore size and distribution. As reported by Uchida *et al.* [166], the Nafion ionomer has rather large (>40 nm) micelles. Metal nanoparticles residing in carbon pores below 40 nm in diameter have no access to the Nafion ionomer and do not contribute to the electrochemical activity. The metal catalyst utilization is determined by the electrochemically accessible active area rather than the carbon specific surface area. Recently, Rao *et al.* [169] investigated the effects of carbon porosity on the specific activity of the Pt–Ru/C catalyst towards methanol oxidation. They found that a higher content of small pore (<20 nm) containing metal particles where the Nafion ionomer could not easily enter resulted in poor contact between the metal nanoparticles and the

Nafion micelles and there was, therefore, a lower level of methanol oxidation activity. For example, 20% PtRu supported on Sib-19P ( $S_{\text{BET}} = 72 \text{ m}^2 \text{ g}^{-1}$ ) showed a mass specific activity of  $180 \text{ mA mg}^{-1}$  at 500 mV during DMFC half cell testing, which is almost six times higher than that for PtRu/Sib-619P ( $S_{\text{BET}} = 415 \text{ m}^2 \text{ g}^{-1}$ ). More recently, Wang *et al.* [170] reported that Vulcan XC-72 supported Pt–Ru catalysts showed improved catalytic activity towards methanol oxidation after the catalyst was pre-treated with ozone. Cyclic voltammetry (CV) results showed that the anodic peak current of the ozone-treated sample was 1.5 times of that of the untreated sample in an Ar-saturated 0.5 M  $\text{CH}_3\text{OH}$  + 0.5 M  $\text{H}_2\text{SO}_4$  solution. This improvement contributed to the increase in the surface concentration of the active functional oxygen containing groups on the ozone-treated Vulcan XC-72. These results indicate that some innovative approaches should be explored for the improvement and optimization of catalyst activity and performance.

(b). Nanostructured carbon

In recent decades, a series of new nanostructured carbon materials have been explored as catalyst supports. The family of carbon nanotubes (CNTs) is the most well-known nanostructured carbon, which has shown very promising results in catalyst support for fuel cell applications, due to their unique electrical and structural properties. The reported studies have shown that CNTs are superior to carbon blacks as catalyst supports for proton exchange membrane fuel cells (PEMFCs) [171, 172]. A CNT supported Pt catalyst with 12 wt.% Pt loading could give a 10% higher fuel cell voltage and twice the power density of carbon black support with 29 wt.% Pt loading [173] and [174]. On the

other hand, many studies have explored CNTs as supports for DMFC catalysts in recent years. Li *et al.* [175-177] reported that multiwall carbon nanotube (MWNT) supported catalysts exhibited better performance in DMFCs compared to those supported by carbon black (XC-72) under identical conditions, both in half cell characterization and in a fuel cell performance test. Their results showed that the mass activity of Pt/MWNT catalyst at 0.7 V (versus dynamic hydrogen electrode (DHE)) in single cell testing was  $14.7 \text{ mA mg}^{-1}$ , much better than Pt/XC-72 catalyst ( $2.2 \text{ mA mg}^{-1}$ ). Che *et al.* [178] found that the current density of methanol oxidation on a Pt/MWNT catalyzed membrane electrode was 20 times higher than that of a bulk Pt electrode. Rajesh *et al.* [179, 180] investigated methanol oxidation catalyzed by various metal catalysts that could be supported on CNTs and commercially available Vulcan carbon. The activity and stability of these electrodes were ranked from highest to lowest as: Pt-WO<sub>3</sub>/CNT > Pt-Ru/Vulcan > Pt/CNT > Pt/Vulcan > bulk Pt. Single-wall carbon nanotube (SWNT) supported Pt electrodes were also reported to exhibit higher catalytic activity both for methanol oxidation and for oxygen reduction than an unsupported Pt electrode [181]. The authors studied the kinetics of the methanol oxidation reaction on Pt/SWCNT electrode and found that the onset potential of methanol oxidation on this electrode was ~200 mV versus saturated calomel electrode (SCE), which was 200 mV lower than that of the unsupported Pt electrode (400 mV versus SCE). The higher catalytic activity was therefore attributed to the larger surface area of carbon nanotube architecture and the lower overpotential for methanol oxidation. Therefore, CNTs appear to have promising potential as catalyst supports for DMFCs.

However, the CNT synthesis, metal loading, and electrode preparation based on CNT supports still face some challenges, especially when applied to fuel cells. CNTs are usually synthesized by carbon-arc discharge, laser ablation of carbon, or chemical vapor deposition (typically on catalytic particles). These synthetic methods have their limitations in terms of large-scale production and cost-effectiveness. The harsh synthetic conditions that they require and their low production yields are major disadvantages. Currently, SWCNTs are produced only on a very small scale, and the process is extremely costly [182]. It is necessary to further develop industrial large-scale production of CNTs to meet the needs of all the possible applications, including the fuel cell industry.

Metal nanoparticle loading onto CNTs with high dispersion is not an easy task. Several methods have been developed to prepare highly dispersed metal/CNT catalysts. The conventional impregnation method has been frequently used to deposit metal nanoparticles onto CNTs [175], [178], and [183]. Using this method, Che *et al.* [178] were able to deposit Pt–Ru alloy particles with a very narrow particle size distribution onto CNTs. However, conventional impregnation techniques based on wet impregnation and chemical reduction of the metal precursors are time consuming, and the catalysts produced are easily contaminated by certain by-products. Alternatively, the electrodeposition method has been used to make CNT supported catalysts because of its high purity and simplicity [172], [174], [181], and [184]. The disadvantage of this method is that it is difficult to estimate the loading of the metallic catalyst, due to the concurrent reduction of protons. It was also difficult to attain small nanoparticles by the electrodeposition method. Recently, Lin *et al.* [185] used a supercritical fluid (SCF)

method as a rapid, direct, and clean approach to prepare Pt/CNT catalyst for DMFCs. It was claimed that the supercritical fluid technology could result in products (and processes) that are cleaner, less expensive, and of higher quality than those produced using conventional technologies and solvents. More recently, the microwave-heated polyol process has been demonstrated to be an effective way to prepare Pt nanoparticles and Pt/CNT nanocomposites [51, 186, 187].

Additionally, it was found that the surface modification of CNTs before metal deposition was important for achieving optimal interaction between the support and the catalyst precursor [188, 189]. Because the pristine surface of CNTs is inert, it is difficult to attach metal nanoparticles to the substrate surface. Through surface modification or pre-treatments, some anchoring sites are introduced onto the surface so the metal nanoparticles can easily attach onto the CNT surface. The most widely used pre-treatment is refluxing CNTs in nitric acid to create an acid site on the surface, which can act as a nucleation center for metal ions.

Another challenge for CNTs as a catalyst support for DMFCs is how to use them to fabricate high performance working electrodes. For an electrode prepared by a conventional ink process, it was estimated that only 20–30% of the platinum catalyst was utilized because of the difficulty for the reactants in accessing interior electrocatalytic sites [181]. Developing new electrode structures could make use of the CNT advantages in structural, electronic, and mechanical properties. Recently, Sun *et al.* [190] developed some techniques to grow CNTs on carbon paper fibers to produce a

three-dimensional nanotube-based hierarchical structure. Platinum or platinum alloys are expected to deposit directly onto these novel CNT-based catalyst supports, which seems to be a promising way to make low-cost electrodes for DMFCs by increasing noble metal utilization.

In addition to CNTs, other nanostructured carbons, such as carbon nanofibers, carbon nanocoils, and fullerenes, have also been explored as catalyst supports for DMFCs. Graphitic carbon nanofibers (GCNFs) have three structure types: platelet, ribbon, and herring-bone. Bessel *et al.* [191] investigated the methanol oxidation activities of these three types of GCNF supported Pt catalysts. They found that the catalysts containing 5 wt.% Pt supported on platelet and ribbon GCNFs exhibited comparable activities to a catalyst consisting of 25 wt.% Pt supported on Vulcan carbon, while a herring-bone GCNF supported Pt catalyst showed poorer electrochemical activity. Steigerwalt *et al.* [149, 150] also prepared highly dispersed Pt–Ru/GCNF catalysts and investigated their performance as anode catalysts for DMFCs. A 50% increase in performance was observed compared to an unsupported Pt–Ru colloid anode catalyst. Recently, carbon nanocoils (CNCs), a new nanostructured carbon support, were synthesized by a solid-phase synthetic method and used as DMFC catalyst supports [192]. The authors prepared Pt–Ru/CNC and Pt–Ru/Vulcan catalysts with 60 wt% metal loading and compared their performance to commercially available E-TEK Pt–Ru/C catalyst for DMFCs. They found that, under identical testing conditions, the current density at 0.6 V catalyzed by a CNC-supported catalyst was 4 and 20 times higher, and the maximum power density was 170% and 230% higher than those of the Vulcan supported catalyst and the commercial catalyst, respectively. The excellent performance was attributed to

the low electrical resistance and the unique pore characteristics of CNCs, which favor the diffusion of methanol and the removal of CO<sub>2</sub> gas. More recently, a fullerene (C<sub>60</sub>) film electrode was also suggested as a catalyst support for methanol oxidation after electrodeposition of Pt on these fullerene nanoclusters [193].

### (c). Mesoporous carbon

Mesoporous carbon used as catalyst support is another new area in DMFC anode catalysis [194]. Generally, a high performance DMFC anode requires an efficient three-phase reaction zone on the nanoscale, in which the electrochemical reactions involving electron and proton transport occur on the surface of metal nanoparticles. In addition, it also requires the provision of an efficient transport passage for liquid-phase reactants (CH<sub>3</sub>OH, H<sub>2</sub>O) and the gas-phase product (CO<sub>2</sub>). Too many small micropores (<2 nm) in carbon supports (e.g., Vulcan XC 72) decreases catalyst utilization, because the mass transport of reactants and product is poor in these micropores. When there are macropores with a size larger than 50 nm, the specific surface area will become small, and the electrical resistance will increase [194]. Mesoporous carbons with tunable pore sizes in the range of 2–50 nm are, thus, attractive for use as catalyst supports and have the potential to enhance both the dispersion and utilization of metal catalysts.

Ordered mesoporous carbon is usually synthesized by a template method, starting with either highly ordered mesoporous silica or nanosized silica spheres. With mesoporous silica or nanosized silica as a template, organic materials are diffused into the pores, and

then carbonized. Uniform mesoporous carbon can be formed after removing the silica template by HF etching. Yu *et al.* [195, 196] synthesized a series of porous carbons with pore sizes in the range of 10–1000 nm by this procedure and investigated the performance of these porous carbon-supported Pt–Ru catalysts under DMFC conditions. They found that the porous carbon with a mesopore size (25 nm) showed the highest performance, which corresponds to a 43% increase in activity as compared to that of a commercially available Pt–Ru/C catalyst (E-TEK). This higher performance was considered to be not only due to the higher surface areas and larger pore volumes, which allowed a higher degree of catalyst dispersion, but also due to the highly integrated interconnected pore systems with periodic order, which allowed efficient transport of reactants and products. Raghuveer and Manthiram [197, 198] used a modified colloidal template route to control the pore size of porous carbon. The obtained mesoporous carbon had a larger surface area and pore volume than the Vulcan XC 72R. They carried out the electrochemical measurements using catalyst coated glassy carbon electrodes, with a catalyst loading of  $0.28 \text{ mg cm}^{-2}$ , and found that the mesoporous carbon loaded with 5% Pt exhibited three times higher mass activity ( $\text{mA mg}^{-1} \text{ Pt}$ ) than the commercially available 20% Pt/C catalyst for methanol oxidation. Recently, spherical carbon capsules with a hollow core and mesoporous shell structure (HCMS) were used to support Pt–Ru catalyst [199]. The HCMS carbon supported catalysts exhibited higher specific activity towards methanol oxidation than the commonly used E-TEK catalyst, by approximately 80%. In addition, mesocarbon microbeads (MCMB), a type of spherical carbon particle with many nodular lumps and pores on its surface, was also investigated as a Pt or Pt–Ru catalyst support for methanol oxidation [200, 201]. Although the particle size of MCMB supported Pt–Ru nanoparticles is comparatively

larger (12–13 nm), better performance compared to Vulcan XC 72R carbon support catalyst was observed. The overpotential of Pt–Ru/MCMB electrode was 0.39 V (versus SCE) at  $300 \text{ mA cm}^{-2}$ , which was 70 mV lower than that of Pt–Ru/Vulcan XC-72 electrode. Therefore, mesoporous carbons appear to have great potential as catalyst supports in DMFC anode catalysis, because they can offer significant cost reduction by improving catalyst utilization and lowering the catalyst loading.

### 2.4 Summary

Many papers were explored for information on inorganic nanocomposite synthesis methods, lithium ion battery tin based anodes, and direct methanol fuel cell electrocatalysts. In this study, the author used different liquid-phase synthesis methods to prepare nanocomposite materials for lithium ion batteries and direct methanol fuel cells.

Tin metal and tin oxides are among the most promising substitute anodes for lithium ion batteries. However, the irreversible capacity is high due to the volume changes during the lithium alloying and de-alloying. In order to prevent this effect, one of the solutions is to use secondary or tertiary components to suppress the volume changes. In the following chapters, carbon nanotubes (CNTs), mesoporous carbons (MCs), and titania nanotubes are used as the ‘buffer matrix’ in different inorganic nanocomposites with tin or tin alloys. These novel inorganic nanocomposites synthesized by different methods show great potential as alternative anodes for lithium ion batteries.

Pt based electrocatalysts supported on carbon materials are commonly used as both anodes and cathodes for direct methanol fuel cells. Different Pt/C nanocomposites were prepared by the impregnation method or the microwave assisted polyol process in this study. The author also evaluated different carbon supports and new methanol tolerant cathode electrocatalysts. These Pt based nanocomposites are novel candidates with high electrocatalytic activities for direct methanol fuel cells.

## CHAPTER 3. EXPERIMENTAL

### 3.1 Typical materials and chemicals

The materials and chemicals were supplied by several chemical companies. Most of them were from the Aldrich Chemical Company Pty. Limited. The details are given in Table 3-1.

Table 3-1 Typical materials and chemicals used in this study.

Materials or Chemicals	Formula	Purity	Supplier
Tin (II) chloride dihydrate	$\text{SnCl}_2 \cdot 2\text{H}_2\text{O}$	98+%	Aldrich
Hexachloroplatinic Acid	$\text{H}_2\text{PtCl}_6 \cdot 6\text{H}_2\text{O}$	A.C.S. Reagent	Aldrich
EG (ethylene glycol)	$\text{C}_2\text{H}_6\text{O}_2$	>99%	Aldrich
Sodium borohydrite	$\text{NaBH}_4$	98%	Aldrich
Sulfuric Acid	$\text{H}_2\text{SO}_4$	98%	Aldrich
Vulcan XC-72 Carbon	C		Cabot Corp.
Methanol	$\text{CH}_3\text{OH}$	Reagent	Aldrich
Lithium hexafluorophosphate	$\text{LiPF}_6$	98%	Aldrich
EC (ethylene carbonate)	$\text{C}_3\text{H}_4\text{O}_3$	>99%	Fluka
DMC (dimethyl carbonate)	$\text{C}_3\text{H}_6\text{O}_3$	99%	Fluka
PVDF (polyvinylidene fluoride)			Aldrich
DMP (dimethyl phthalate)	$\text{C}_6\text{H}_4\text{-1, 2-(CO}_2\text{CH}_3)_2$	99%	Aldrich
Carbon black	C		Lexel

### 3.2 Experimental procedures

Various inorganic nanocomposites were prepared by different methods. Synthesized tin based nanocomposites for lithium ion batteries and Pt based electrocatalysts were used for preparing testing electrodes. Coin cells (CR2032) were assembled to examine the electrochemical properties of lithium ion batteries, and a conventional three-electrode electrochemical testing cell was used to evaluate the electrocatalytic performance. The overall experimental procedure is schematically illustrated in Fig. 3-1.

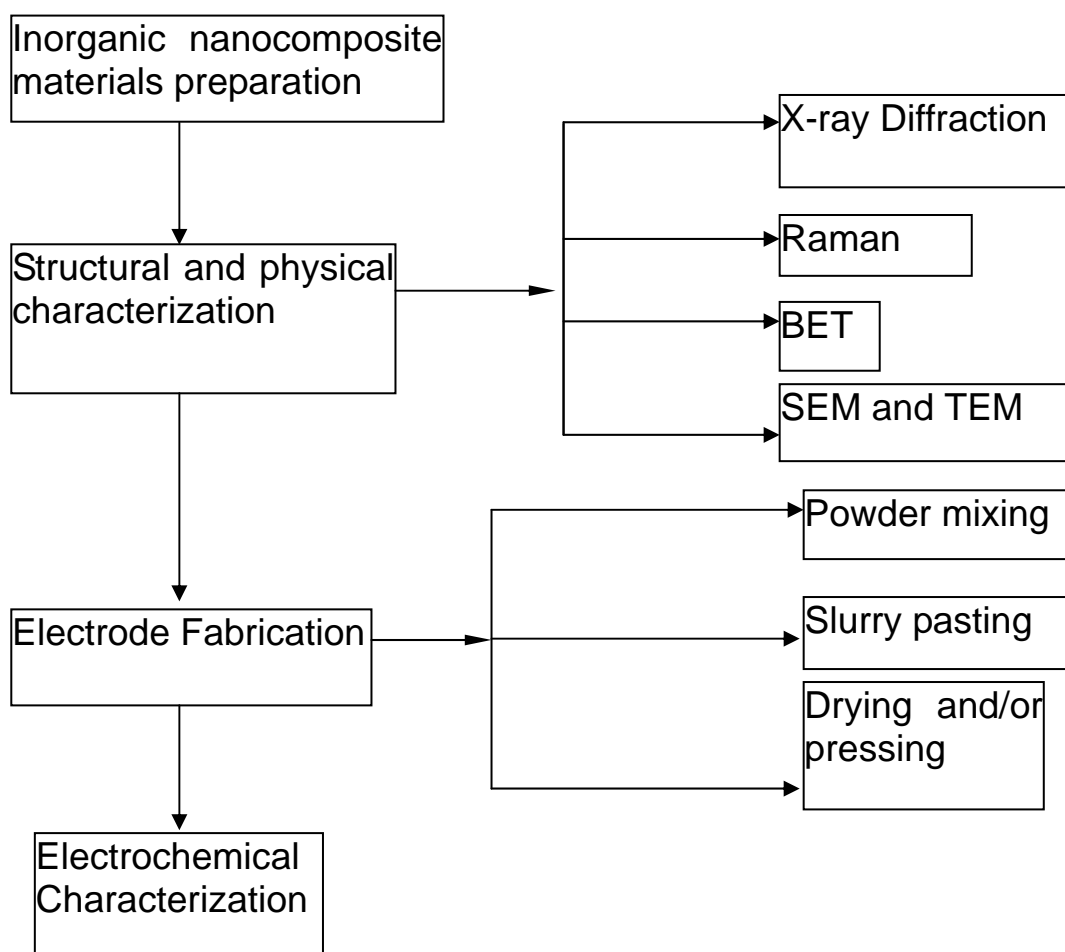


Fig. 3-1 Schematic diagram of experimental procedure.

### 3.3 Structural and physical characterization of the nanocomposites

The synthesized nanocomposite materials were thoroughly characterized by a variety of approaches. X-ray diffraction patterns were obtained with a Phillips PW 1730 generator and diffractometer using Cu K $\alpha$  radiation and a graphite monochromator. The crystal size was calculated by the Scherrer formula:

$$d = k\lambda/\beta \cos\theta, \quad (3-1)$$

where  $\lambda$  is the X-ray wavelength (1.54056 Å),  $\theta$  is the Bragg angle, and  $\beta$  is the half-peak width in radians. According to Bragg's law:

$$2d \sin \theta = n\lambda \quad (3-2)$$

where  $\theta$  is measured from the plane and  $\lambda$  is the wavelength.

Nanocomposites were analyzed by the X-ray diffraction technique for structural identification and to monitor changes in the crystallinity.

The morphology of the as-prepared products was observed by scanning electron microscopy (SEM) using a JEOL JSM-6460A instrument, with additional semi-quantitative information obtained using large area standardless energy dispersive spectroscopy (EDS). Transmission Electron Microscopy (TEM) and High Resolution (HR) TEM were performed using a JEOL JEM 2011 device. TEM samples were dispersed on lacey carbon support films. The nitrogen adsorption-desorption isotherms were measured using a Micromeritics ASAP 2010 analyzer. The pore size was

calculated by the Barrett-Joyner-Hallenda (BJH) method, based on the desorption branch of the nitrogen sorption isotherms. The specific surface area was determined by the gas sorption technique, using the Brunauer-Emmett-Teller (BET) method. A Quantachrome Nova 1000 gas sorption analyzer was used for this purpose.

### **3.4 Electrode preparation**

#### **3.4.1 Electrode preparation for lithium ion batteries**

The electrodes were made by dispersing a mixture of 75 wt% active materials, 10 wt% carbon black, and 15 wt% PVDF binder into dimethyl phthalate to obtain a slurry. (This ratio may be adjusted in certain cases.) The slurry was spread onto copper foil or a copper mass. After the electrode was dried at 120°C overnight, it was compressed at a rate of about 170 kg/cm<sup>2</sup>. The electrodes were then dried in a vacuum furnace for 24 hours and finally transferred to a glove box. The electrode area was approximately 1 cm<sup>2</sup>, and the typical thickness of the electrode was about 100 μm.

#### **3.4.2 Electrode preparation for direct methanol fuel cells**

The working electrode was a thin layer of catalyst spread on a vitreous carbon disk held in a Teflon cylinder. The catalyst layer was prepared by the following procedures: (a) making a slurry by sonicating 1 mg catalyst and 1ml deionized water; (b) spreading

10 $\mu$ L of the slurry on the carbon disk; and (c) then drying the electrode at room temperature for 2 h.

### 3.5 Test cell construction

#### 3.5.1 Cell construction for lithium ion batteries

The test cells were assembled in an argon filled glove box (Unilab, Mbraun, USA), in which moisture and oxygen were automatically controlled to be less than 0.1 ppm. In order to examine the electrochemical properties of the prepared electrode materials, lithium metal was used as a standard counter electrode in all test cells. The electrolyte was 1 M LiPF<sub>6</sub> in a solution of EC (ethylene carbonate) and DMC (dimethyl carbonate) (1:1 in volume). The separator was Celgard 2500 porous plastic film. The coin test cell used in the present work is shown in Fig. 3-2.

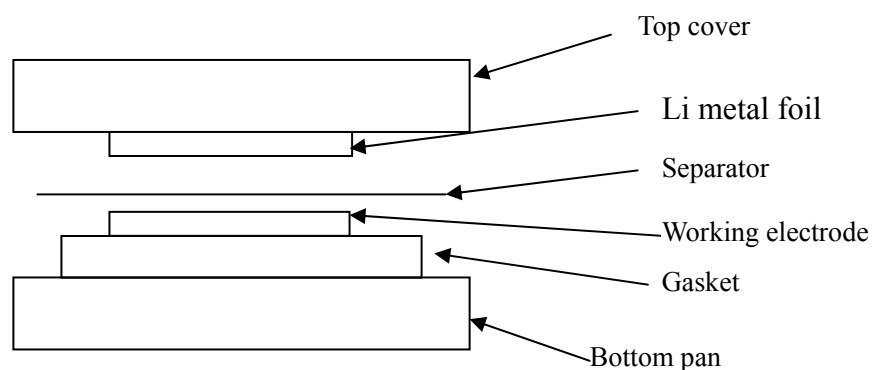


Fig. 3-2 Schematic diagram of the configuration of the coin test cell.

#### 3.5.2 Cell construction for the direct methanol fuel cell

A conventional three-electrode test cell was used for cyclic voltammetric (CV) testing

(Fig. 3-3). Pt wire and a saturated Hg/Hg<sub>2</sub>SO<sub>4</sub> electrode or an Ag/AgCl electrode were used as the counter and reference electrodes, respectively. The electrolyte solution (0.5 M H<sub>2</sub>SO<sub>4</sub> or 1 M CH<sub>3</sub>OH in 0.5 M H<sub>2</sub>SO<sub>4</sub>) was de-aerated in high purity Ar before measurements. The glassy carbon working electrode was polished with an alumina nanoparticle slurry before use. The methanol tolerance studies were carried out in 0.5 M H<sub>2</sub>SO<sub>4</sub> electrolyte containing various amounts of methanol, which was de-aerated in high purity N<sub>2</sub> before measurements. Oxygen reduction was studied in 0.5 M H<sub>2</sub>SO<sub>4</sub> electrolyte employing a rotating disk electrode (RDE). The electrolyte was saturated with pure oxygen before measurements.

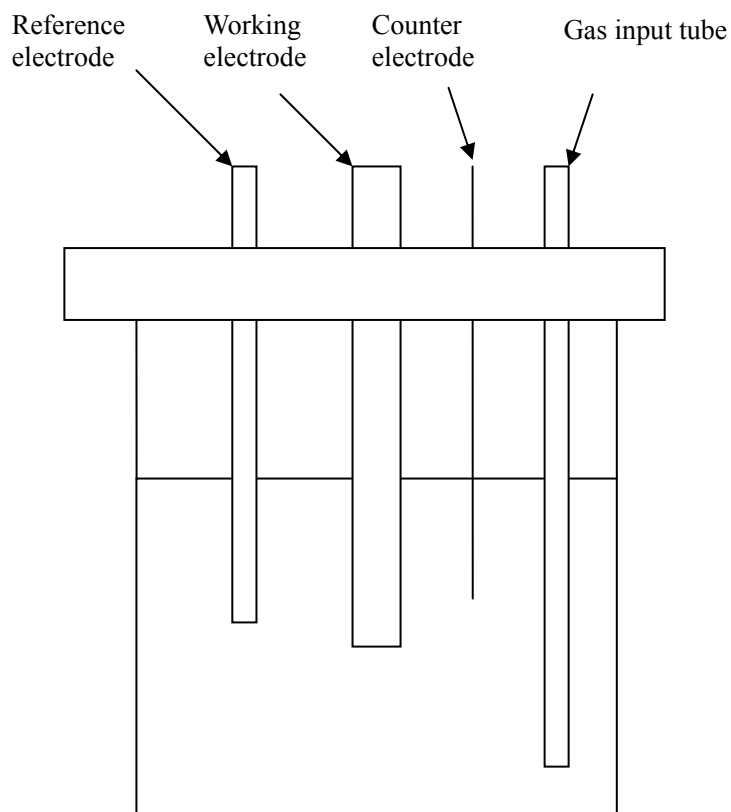


Fig. 3-3 Schematic diagram of the conventional three-electrode electrochemical cell.

### **3.6 Electrochemical performance characterization**

#### **3.6.1 Electrochemical characterization for the lithium ion battery**

The assembled test cells were cycled galvanostatically at a constant current density with a pre-determined cut-off voltage. The cycling tests were performed at different current densities for different electrode materials.

Cyclic voltammetry (CV) was performed to determine the characteristics of the lithium insertion/extraction reactions for the investigated electrodes. The CV measurements were carried out with an electrochemical workstation (CHI 660B), at a pre-determined sweep rate. The a.c. impedance measurements were used to analyze the interface behavior between the active materials and the electrolyte, and the kinetic properties of the electrode materials were characterized using an EG&G Princeton Applied Electrochemical Impedance Analyzer (Model 6310). Electrochemical impedance software (Model 398) was used to provide computer control for conductivity and stability measurements. A.c. impedance was measured potentiostatically, with a 5mV AC input signal applied between the working and reference electrodes over a frequency range from 100 to 0.001Hz at six points per decade of frequency.

#### **3.6.2 Electrochemical characterization for direct methanol fuel cells**

Electrochemical measurements were carried out on electrochemical workstations (CHI 660B and EG&G Princeton Model 2273). The cyclic voltammetry measurements were carried out in 0.5 M H<sub>2</sub>SO<sub>4</sub> electrolyte at a scan rate of 20-50 mV s<sup>-1</sup> or in an electrolyte consisting of 0.5 M H<sub>2</sub>SO<sub>4</sub> and 1 M methanol at room temperature. The specific electrochemical surface area (ECA) of Pt (sometimes referred to as the real Pt catalyst surface area) was calculated by integrating the CV curves in the hydrogen absorption region, assuming that the charge per real cm<sup>2</sup> of Pt with monolayer adsorption of hydrogen is 210 μC/cm<sup>2</sup>. The hydrodynamic voltammetry technique was employed to study the number of electrons consumed during the course of the oxygen reduction reactions. Linear sweep voltammetry measurements were performed on a rotating electrode disk in the O<sub>2</sub>-saturated 0.5 M H<sub>2</sub>SO<sub>4</sub> electrolyte.

## CHAPTER 4. ELECTROCHEMICAL LITHIATION AND DE-LITHIATION OF MWNT-Sn/SnNi NANOCOMPOSITES

### 4.1 Introduction

Lithium ion batteries continue to be the state-of-the-art power sources for consumer electronic devices because of their high capacities, long charge/discharge cycle life and lack of “memory effect” [202-204]. However, while cathode systems have been researched extensively, anode materials are now also beginning to receive significant attention [205-208]. While the numerous chemically or physically modified carbons have received intensive investigation [209-211] and become typically the anode material of choice, metals and metallic alloys have also been studied as anodes, because of their higher theoretical capacity than carbonaceous materials. However, a large specific volume change occurs during Li insertion and extraction reactions in metallic systems, which causes the electrode to fail by pulverization. As a result rapid capacity fading is observed. Metal-carbon composites such as Sn-C [212], SnSb-MCMB [213], and Sn-Fe-C [214] were introduced to overcome this problem. All these nanocomposite systems are based on the concept that the ductile carbonaceous materials could absorb the mechanical stress caused by the volume change, thus improving the cyclability of the composite electrode. Although these systems are promising, there are problems related to either capacity or cyclability. The chemical and electrochemical stability are also difficult to control in these systems. More recently, Chen *et al.* [215] used carbon nanotube as a support matrix to prepare CNT-Sb and CNT-SnSb<sub>0.5</sub> nanocomposites. Although the cyclability is improved compared with metal electrodes, CNT-Sb/ SnSb<sub>0.5</sub>

systems still pose some problems, such as large first cycle irreversible capacity (804 mAh/g for CNT-Sb and 574 mAh/g for CNT-SnSb<sub>0.5</sub>) and a relatively high capacity fading rate (1.3%/cycle and 1.1%/cycle for CNT-Sb and CNT-SnSb<sub>0.5</sub>, respectively), which prevents their use as anodes in commercial systems. As a result, there is a need for improving the concept of CNT supported nanocomposites further.

In this chapter, high quality MWNTs were prepared by a catalytic CVD method, followed by a series of purification processes. Results of the charge/discharge tests indicate excellent electrochemical performance. Furthermore, we prepared nanocrystalline MWNT-Sn and MWNT-SnNi composites using a chemical reduction procedure. The electrochemical properties of nanocrystalline MWNT-Sn and MWNT-SnNi composites as anode materials in lithium ion cells were systematically evaluated.

## **4.2 Synthesis and structure characterization of MWNT-Sn and MWNT-SnNi composites**

### **4.2.1 Preparation of MWNTs**

The MWNTs were prepared by catalytic CVD using nanosized cobalt as the catalyst. During the production of MWNTs, about 100 mg of catalyst was placed in a quartz tube mounted in a tube furnace. The furnace was initially evacuated and then purged with argon gas. The furnace was then heated to 800-1000°C under a continuous argon flow. The argon was then replaced by acetylene at a flow rate of 100-500 ml/min for 20-60

min. The synthesized MWNTs were then purified by stirring in concentrated HF acid and distilled water (in a 1:3 ratio) for 18 h, which was then followed by gas-phase oxidation in a 15% air/Ar mixture at 550°C for 1 h. The oxidized MWNTs were sonicated in concentrated HCl acid for 30 min. Then the purified samples were filtered, washed with distilled water, and dried overnight at 150°C.

#### **4.2.2 Preparation of MWNT nanocomposites with Sn and SnNi**

Composites of MWNT with Sn and SnNi were prepared by chemical reduction of metal chloride salts in MWNT suspensions. Typically, calculated amounts of  $\text{SnCl}_2 \cdot 2\text{H}_2\text{O}$  and  $\text{NiCl}_2 \cdot 6\text{H}_2\text{O}$  were dissolved in alcohol to obtain 0.02 mol/L solutions. 50 ml of each solution was added to a beaker and further dissolved in 100 ml distilled water, followed by the addition of 0.044 g of MWNTs prepared by the procedures above. The suspension was sonicated for 2 h, followed by gently adding  $\text{NaBH}_4$  under continuous and vigorous stirring until the air bubbles no longer emerged. The MWNT-SnNi composites were then filtrated and subsequently washed with large amounts of distilled water, then alcohol, then distilled water again, followed by an overnight drying under vacuum at 120°C. MWNT-Sn composites were prepared by only transferring 50 ml of  $\text{SnCl}_2 \cdot 2\text{H}_2\text{O}$  solution to the reaction beaker, and Sn particles were synthesized by the same method, but in the absence of MWNTs.

#### **4.2.3 Microstructural characterization**

Fig. 4-1 shows the XRD patterns of the nanocomposites. As a comparison, the XRD patterns of the bare MWNT and nanocrystalline Sn prepared by the same chemical

reduction method are also presented. The peaks due to MWNT and Sn diffraction can be clearly observed. The  $d_{002}$  value derived from the peak of the (002) diffraction of graphite in the MWNT-Sn nanocomposite is 0.338 nm, indicating that the MWNTs are well-graphitized. The calculated mean crystallite size along the c-axis ( $L_c$ ) is 2.4 nm. The sharp peaks of tin also show that the tin in the nanocomposite is well-crystallized tin. The SnNi alloy prepared by chemical reduction has an amorphous structure. As shown in Fig. 4-1(a), its XRD spectrum indicates a typical amorphous character, with a broad, low-intensity, diffraction peak [216].

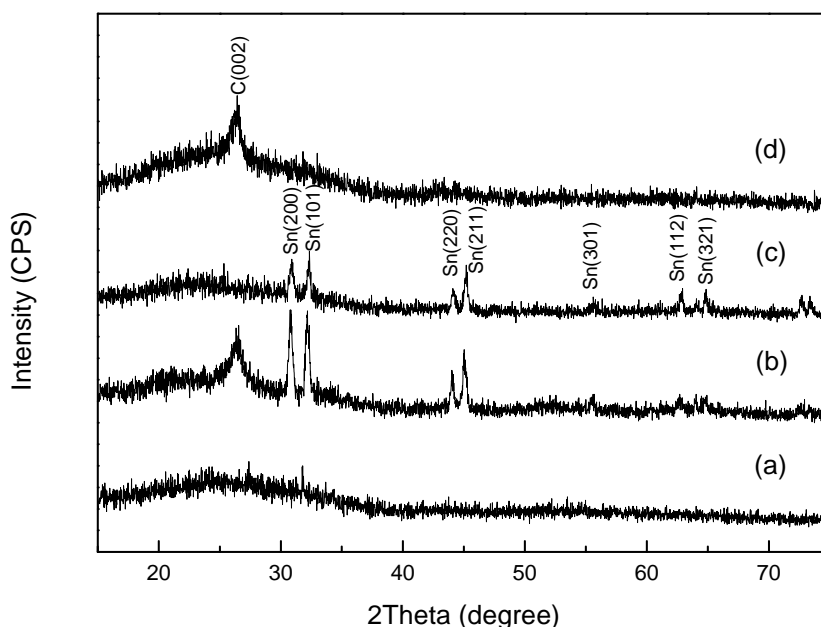


Fig. 4-1 X-ray diffraction (XRD) patterns of (a) SnNi alloy; (b) MWNT-Sn nanocomposite; (c) Sn; and (d) MWNTs.

The SEM morphologies of the SnNi samples and MWNT-supported nanocomposites are presented in Fig. 4-2. The SnNi alloy appear to be in a porous and nanocrystalline phase. The unsupported SnNi is agglomerated together, with the agglomerated particle size in the range of 100-200nm. The composition of tin and nickel on the particle surface

of the alloy, as determined by EDS analysis, was 52% Sn and 48% Ni. In the case of MWNT-Sn and MWNT-SnNi nanocomposites, most of the carbon nanotubes are entangled together, so that the MWNT web captures a large majority of the metallic particles between 100 and 200 nm in diameters. Typical HRTEM images of MWNT-Sn/SnNi nanocomposites show that metal clusters with diameters ranging from 3 to 5 nm are homogeneously dispersed on the surface of the MWNTs. Hence, both XRD and TEM confirm that the chemical reduction method leads to the formation of small homogeneous clusters of metallic Sn and SnNi particles on MWNT support.

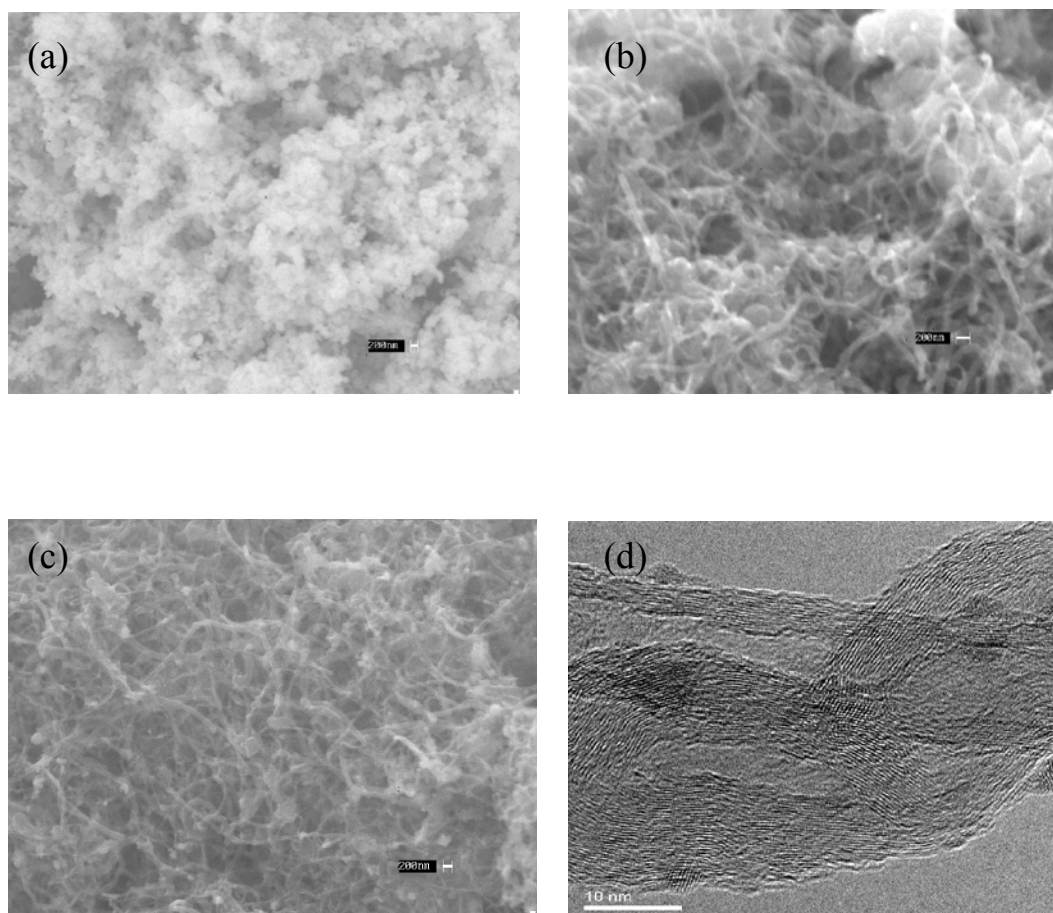


Fig. 4-2 SEM images of (a) SnNi; (b) MWNT-SnNi; (c) MWNT-Sn; and (d) typical TEM image of MWNT-Sn/SnNi nanocomposite.

### 4.3 Electrochemical testing of nanocomposite electrodes

To get a rough estimation of the electrochemical behavior of the nanocomposites, cyclic voltammetry was first conducted at a scan rate of 0.1 mV/s. Cyclic voltammograms of MWNT, Sn, SnNi, CNT-Sn, and CNT-SnNi electrodes in lithium-ion cells, in which lithium foil was used as the counter electrode and reference electrode, are shown in Fig. 4-3. In Fig. 4-3(a), the lithium insertion potential in MWNT electrode is quite low, 0.02 V versus the Li/Li<sup>+</sup> reference electrode, whereas the potential for lithium de-intercalation is in the range of 0.15-0.35 V. Wu *et al.* think that it is the presence of interstitial carbon atoms and the strong binding with inserted lithium that gives rise to the large hysteresis [217]. The voltage range does not significantly affect the potentials of the lithium ion insertion and extraction peaks. For the bare Sn electrode, the irreversible peak of electrolyte decomposition in the first cycle above 1.0 V can be clearly seen. There are roughly three pairs of other cathodic/anodic peaks that can be observed. A shoulder at about 0.5 V vs. Li/Li<sup>+</sup> is also present on the negative potential side of the anodic peak at 0.65 V vs. Li/Li<sup>+</sup>. These peaks originate from the phase transitions between Li<sub>2</sub>Sn, LiSn, Li<sub>7</sub>Sn<sub>3</sub>, Li<sub>5</sub>Sn<sub>2</sub>, and Li<sub>22</sub>Sn<sub>5</sub>, respectively [218]. However, the cyclic voltammogram of the SnNi nanocomposite electrode is totally different from that of the Sn electrode. Only one anodic peak was observed in the cyclic voltammogram of SnNi electrode, although the Ni component in the SnNi alloy electrode is electrochemically inactive. The reason for this phenomenon is not clear yet, but one possible explanation is: SnNi dissociates and transforms into pure nickel metal and Li<sub>x</sub>Sn during the charging process, but the SnNi could be regenerated in the fully discharged state. The total charging-discharging behavior of SnNi can be explained in the following reaction [219]:



For the MWNT-Sn nanocomposite electrode, one pair of reduction and oxidation peaks appeared at around 0.02 and 0.1 V vs.  $\text{Li/Li}^+$ , corresponding to the lithiation and delithiation of MWNT in the MWNT-Sn nanocomposite. There are four other anodic peaks that can be clearly observed at about 0.5, 0.62, 0.71 and 0.79 V vs.  $\text{Li/Li}^+$ , respectively. These peaks are related to the Li extraction from Sn in the MWNT-Sn nanocomposite. However, there are only two corresponding cathodic peaks that can be observed in the cathodic scans of the CV. Moreover, the irreversible peak of electrolyte decomposition in the first cycle above 1.0 V can barely be observed, which implies a small irreversible capacity during the first cycle for the MWNT-Sn nanocomposite electrode. This conclusion has been verified by the charge/discharge curves (Fig. 4-5).

For the MWNT-SnNi nanocomposite electrode, the reduction/oxidation peaks corresponding to Li insertion/extraction from MWNT, which are located at around 0.02 and 0.1 V, still appear in the CV curves. However, all the other peaks, which are related to lithiation and de-lithiation of Sn, disappear. On the other hand, an anodic peak at about 0.5 V, which corresponds to Li extraction from SnNi in MWNT-SnNi nanocomposite, can be clearly seen. Comparison of the CVs of all the electrodes indicates differences in the cyclabilities of the metallic systems and MWNT supported nanocomposites in the potential range from 1.5 V to 0.02 V vs.  $\text{Li/Li}^+$ . In the CV of MWNT supported nanocomposites, there is little decrease in the current with cycling, which implies good cyclability of nanocomposite electrodes. However, noticeable decreases can be seen in the peak currents during cycling for the metallic electrodes.

This means that cyclability of metallic electrodes can be improved by adding MWNT support.

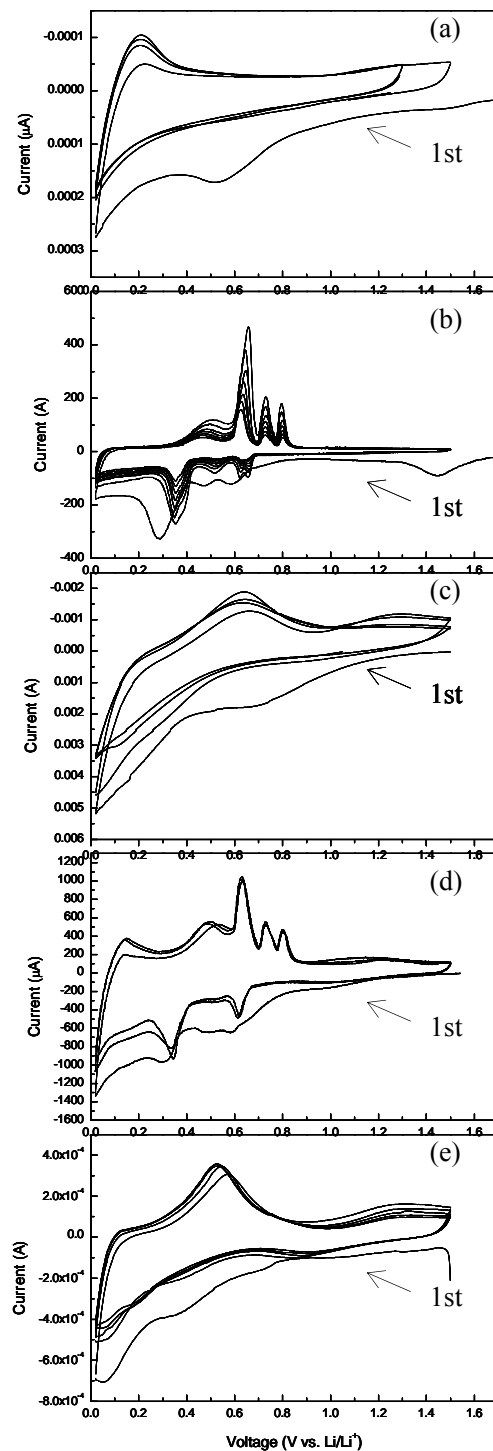


Fig. 4-3 Cyclic voltammograms of (a) MWNT electrode; (b) bare Sn electrode; (c) SnNi electrode; (d) MWNT-Sn electrode; and (e) MWNT-SnNi electrode.

Such a conclusion was verified by charge/discharge cycling tests. Fig. 4-4 shows the cycle life behavior of CNT, Sn, SnNi, MWNT-Sn, and MWNT-SnNi electrodes in constant current charge/discharge mode. The bare MWNT electrode is very stable on cycling, but with limited capacity. The bare nanocrystalline Sn anode has the highest first discharge capacity (670 mAh/g), however, its capacity fades rapidly on cycling. Furthermore, this value is still much lower than the theoretical capacity (990mAh/g) of bare Sn electrode. Therefore, it is not suitable to use nanocrystalline Sn alone as an electrode in Li-ion cells. Generally, nanocrystalline MWNT-Sn and MWNT-SnNi composite electrodes demonstrated superior performance (high capacity and satisfactory cyclability), compared to SnNi, bare MWNT, and bare nano-Sn electrodes.

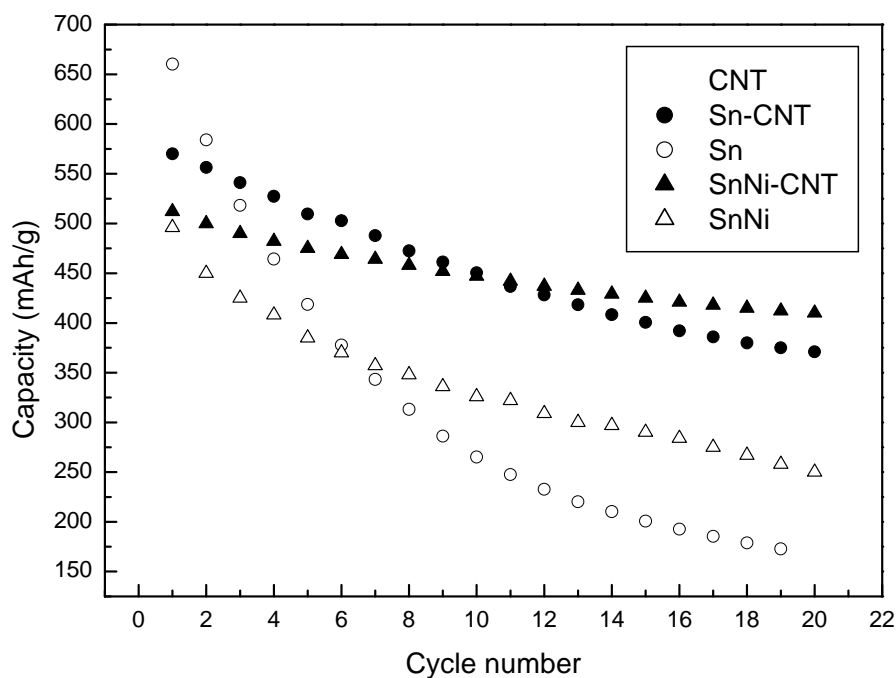


Fig. 4-4 The discharge capacity vs. cycle number. Note that the current density was 50 mA/g.

In particular, the MWNT-SnNi electrode shows stable cyclability with only 0.99% capacity loss/cycle. Compared with the pure MWNT samples reported by Wu *et al.*

[217], the efficiency after 20 charge/discharge cycles for MWNT is much better than for their two MWNT samples. The discharge capacity for MWNT-SnNi after 20 cycles is 80% of the first discharge capacity, which is comparable with their MWNT samples, and even MWNT-Sn electrode exhibits a similar capacity retention ( $Q_{20}/Q_{\max} = 65\%$ ) to their sample A ( $Q_{20}/Q_{\max} = 66\%$ ) (Table 4-1).

Table 4-1  $Q_{20}/Q_{\max}$  of different samples ( $Q_{20}$  is the discharge capacity at the 20th cycle,  $Q_{\max}$  is the maximum discharge capacity of samples).

Samples	$Q_{20}/Q_{\max}$
MWNT	98%
MWNT-SnNi	80%
MWNT-Sn	65%
Sample A of Wu <i>et al.</i> [217]	89%
Sample B of Wu <i>et al.</i> [217]	66%

Fig. 4-5 shows the charge/discharge profiles in the first cycle for the MWNT, Sn, SnNi, MWNT-Sn, and MWNT-SnNi electrodes, respectively. There are several plateaus in the voltage profiles for the lithiation and de-lithiation of MWNT-Sn alloy (Fig. 4-5(d)), which is quite similar to those of the Sn electrode (Fig. 4-5(b)). The Sn electrode had a very high irreversible capacity of about 810 mAh/g in the first cycle. In contrast, the MWNT-Sn electrode delivered a reversible capacity of 570 mAh/g in the first cycle with high efficiency (77.5%).

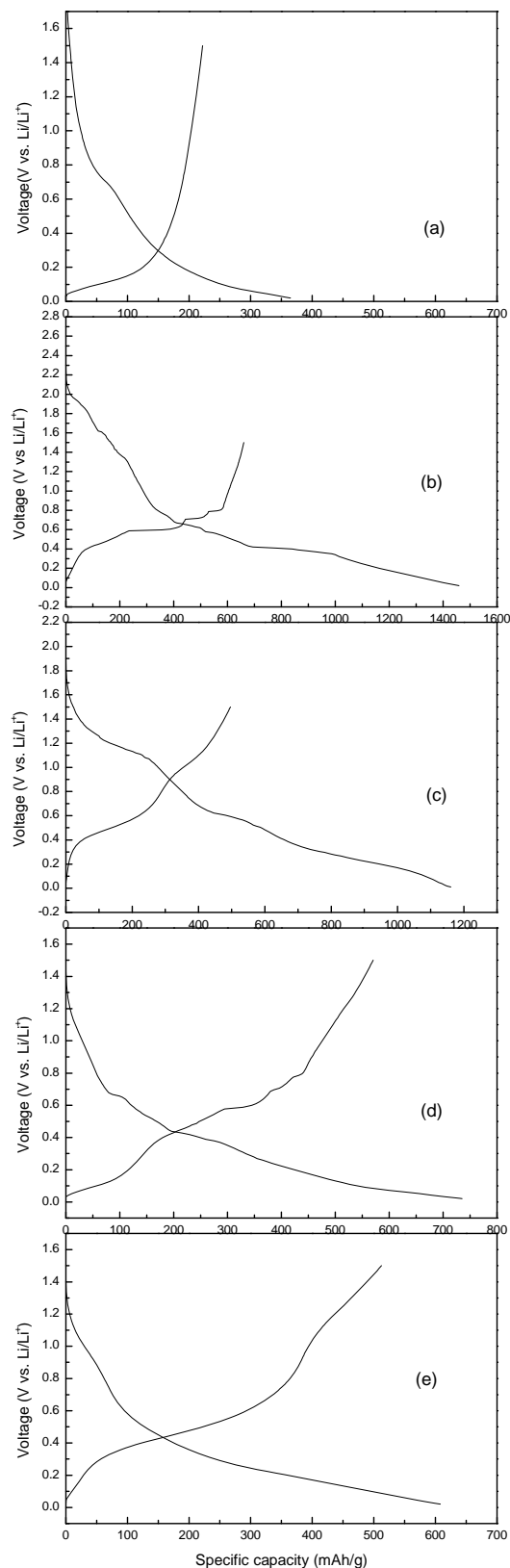


Fig. 4-5 The charge/discharge profiles in the first cycle for (a) bare MWNT electrode; (b) bare Sn electrode; (c) SnNi electrode; (d) MWNT-Sn electrode; and (e) MWNT-SnNi electrode.

The formation of Li-Sn alloy induces a large volume increase, which could create microcracks and therefore destroy the integrity of the electrode, causing high irreversible capacity and poor cyclability in the bare Sn electrode. However, the integrity of the MWNT-Sn electrode could be preserved under repeated lithium insertion and extraction. Because the Sn particles are nanosize in nature, the volume increase in the local environment is small and can be easily absorbed by the ductile MWNT matrix surrounding the nano-Sn clusters. As a result, the volume change in the macrodomain is negligibly small for MWNT-Sn electrodes. For the MWNT-SnNi electrodes, an even higher charge/discharge efficiency (84.1%) and a comparable reversible capacity (512 mAh/g) were achieved in the first cycle compared with the MWNT-Sn electrode. Ni in MWNT-SnNi is an inactive component which provides good binding properties and can also withstand the stresses arising from the alloying and de-alloying of Sn with Li, due to its good electrical conductivity, mechanical strength, and chemical inertness. Therefore, besides the buffering effect of the MWNT matrix in the macrodomain, Ni in the MWNT-SnNi can further absorb or buffer the volume expansion in local SnNi domains. Ni could also promote better dispersion of Sn in MWNT-SnNi nanocomposites, so that a higher charge/discharge efficiency can be achieved. A proposed schematic model of the lithiation and de-lithiation process in MWNT-Sn and MWNT-SnNi nanocomposites is presented in Fig. 4-6.

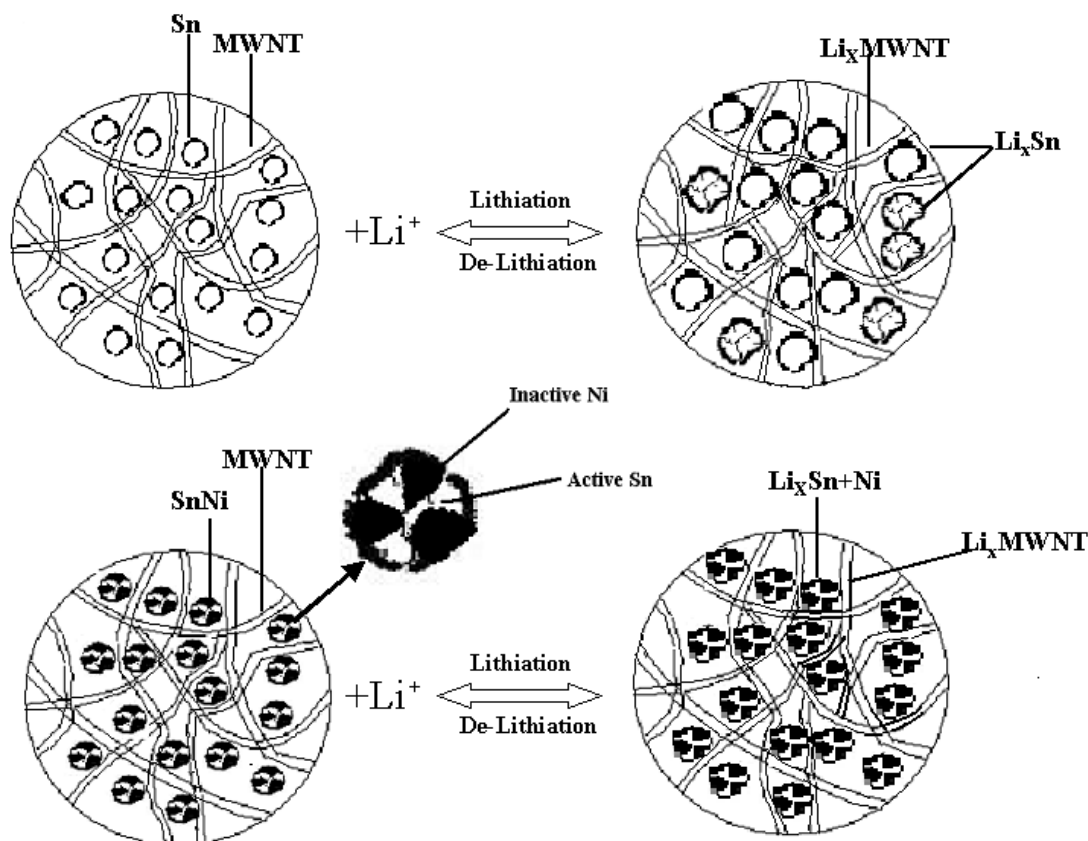


Fig. 4-6 Schematic model of the lithiation and de-lithiation processes in MWNT-Sn (top) and MWNT-SnNi (bottom) nanocomposites. For MWNT-Sn anode, most of the volume increases due to the formation of  $Li_xSn$  alloys are buffered by the MWNT matrix, while the volume increases are effectively absorbed by the inactive component Ni in MWNT-SnNi in the local domain and further absorbed by the MWNT matrix in the macrodomain.

To verify the reason for the improved charge/discharge efficiency and the improved cyclability of nanocomposites with MWNT support, ac impedance measurements were conducted to investigate the interface reaction between the electrolyte solution and the electrode. The thickness of the electrodes was controlled at 50  $\mu m$ , and the coated area of the electrode at 1  $cm^2$ . Samples were initially cycled five times at room temperature, and electrochemical impedance spectroscopy (EIS) measurements were carried out after electrodes were charged up to 1.5 V. EIS plots of all the electrodes presented in Fig. 4-7 show only one depressed semicircle instead of two semicircles in the high and

intermediate frequency region, which generally correspond to the migration within the surface layer and the charge transfer process, respectively. The reason for this phenomenon is that the passivated film on the anode surface is destroyed by the de-intercalation of lithium ions from the anode, so that the resistance of the SEI film decreases very rapidly. The two semicircles in the high and intermediate frequency regions overlap and appear to be one. The 45° line in the low-frequency region presents typical characteristics of the Warburg impedance,  $Z_w$ , which generally reflects the diffusion process of lithium within the bulk electrode. A comparison of the EIS Nyquist complex plots (Fig. 4-7) shows that the size of the semicircle drastically increases with increasing cycle number for the bare Sn electrode, while small and negligible increases in semicircle size are observed in the EIS plots of the MWNT-Sn and MWNT-SnNi electrodes, respectively. Zview 2.3 C software was used to quantitatively analyze the condition of the anodes, and the situation at the anodes can be approximately represented by the equivalent circuit in Fig. 4-8. In this circuit a constant phase angle element,  $Z_w'$ , rather than the true capacitances, is taken into account, due to the depressed nature of the semicircles. For a rough or porous electrode, such as the composite electrodes being analyzed here, the ac signal penetration depth is comparable to the depth of the pores, especially at high frequencies, and the frequency dispersion of the impedance is analogous to that of a non-uniform transmission line. Therefore, such a non-faradaic response can be represented by a constant phase angle element,  $Z_w'$ , with the form

$$Z_w' = A_w' (j\omega)^{-m} = A_w' \omega^{-m} [\cos(m\pi/2) - j\sin(m\pi/2)] \quad 0 < m < 1 \quad (4-2)$$

where A is termed the  $Z_w'$  factor, and m is the  $Z_w'$  exponent.

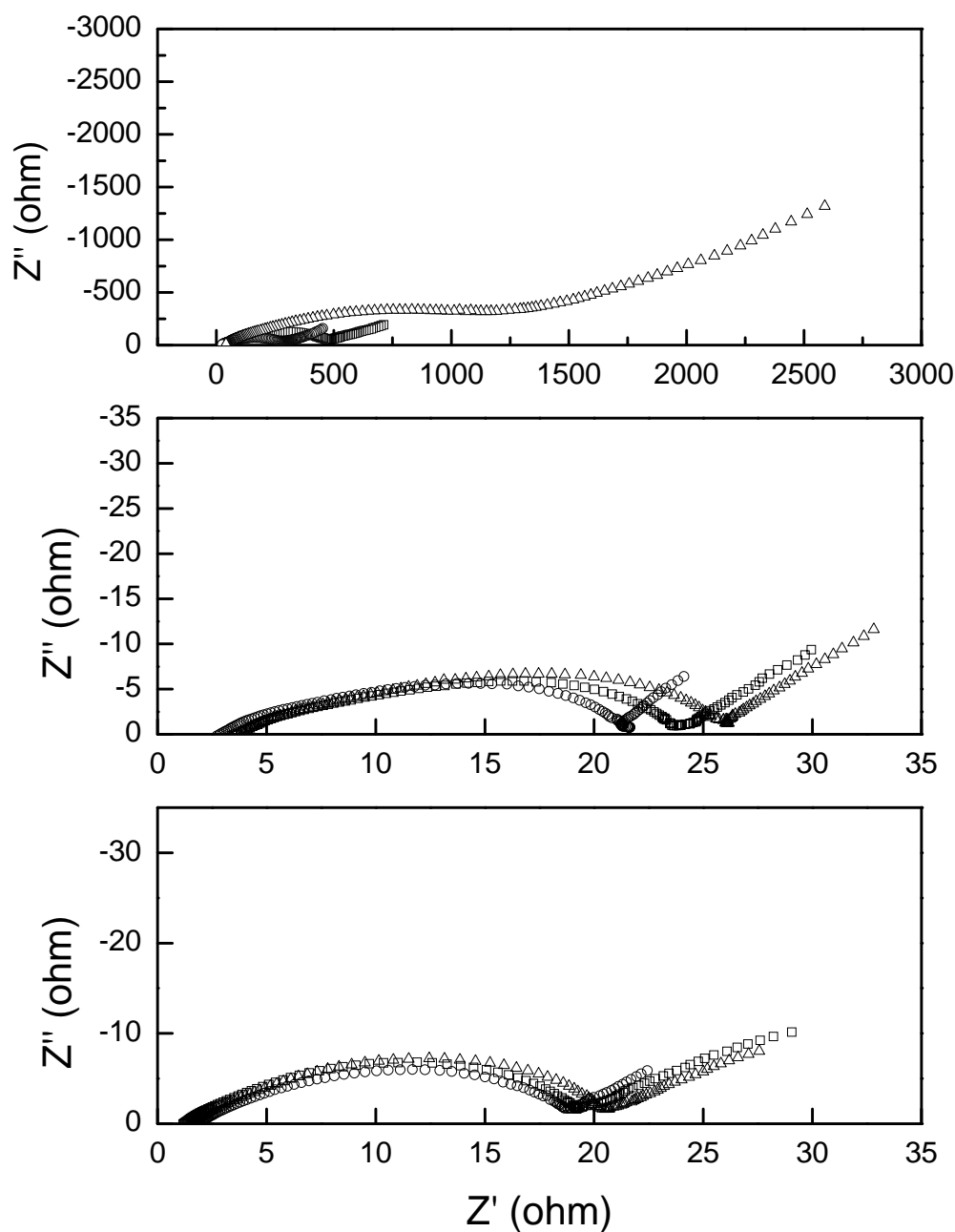


Fig. 4-7 Ac impedance spectra for the bare Sn electrode (top), MWNT-Sn electrode (center), and MWNT-SnNi electrode (bottom).  $\circ$ : after 5 cycles;  $\blacksquare$ : after 10 cycles;  $\triangle$ : after 20 cycles.

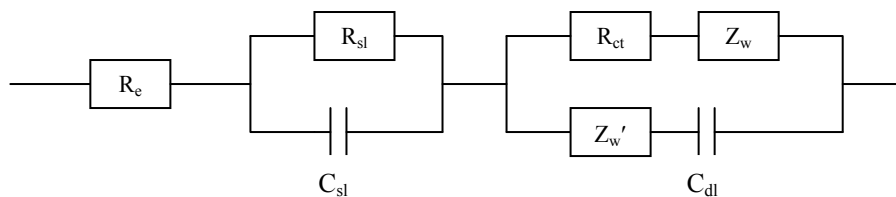


Fig. 4-8 Equivalent circuit for the bare Sn and MWNT-Sn/SnNi nanocomposite electrodes.

Across the surface layer, the ion transport may be represented by the insertion-ion resistance,  $R_{sl}$ , and the surface-layer capacitance,  $C_{sl}$ .  $R_e$  is the solution resistance of the cell,  $R_{ct}$  is the anode charge-transfer resistance, and  $Z_w$  is the Warburg impedance. Table 4-2 lists the results calculated from ac impedance spectra based on the equivalent circuit shown in Fig. 4-8 using ZView 2.3C software. For the bare Sn electrode, the charge transfer resistance ( $R_{ct}$ ) significantly increases with increasing cycle number, while  $R_{sl}$  also slightly increases with cycling.

Table 4-2 Results of ac impedance analysis of the bare Sn, MWNT-Sn, and MWNT-SnNi electrodes.

Electrodes	$R_{sl}$			$R_{ct}$		
	5 cycles	10 cycles	20 cycles	5 cycles	10 cycles	20 cycles
Sn	124	170	293	215	418	1382
MWNT-Sn	6.8	5.6	7.1	16.4	17.6	21.5
MWNT-SnNi	4.3	4.6	4.4	17.3	17.6	17.7

Generally, for the anode of a lithium ion battery, the value of  $R_{ct}$  reflects the compaction of particles in the composite anode, i.e. the extent of interparticle contacts such as MWNT-carbon, MWNT-MWNT, Sn-carbon and MWNT-Sn or MWNT-SnNi, etc.  $R_{sl}$  is the resistance that occurs when ions transfer through the surface layer, i.e. the passivation film caused by the reaction between the electrode and electrolyte. Therefore, the increase in the diameter of the semicircle for the bare Sn electrode is mainly ascribed to an increase in the interparticle contact resistance, which is induced by cracking or crumbling of the particles during cycling. On the other hand, the cracking or crumbling of particles creates fresh electrode/electrolyte interface, on which new SEI film could form during cycling afterwards, which leads to an increase in  $R_{sl}$ . Therefore, high irreversible capacity and low charge/discharge efficiency can be observed for the bare Sn electrode. For the MWNT-Sn nanocomposite electrode, although the  $R_{ct}$  slightly increases with increasing cycle number,  $R_{sl}$  is very stable, which indicates that there is not much fresh electrode/electrolyte interface formed during cycling, i.e. no obvious cracking and crumbling of particles. Therefore, the integrity of the electrode was preserved for repeated lithium insertion and extraction. Compared with the MWNT-Sn electrode, the changes in  $R_{sl}$  and  $R_{ct}$  with cycling for the MWNT-SnNi electrode were even smaller, meaning that the cyclability and the charge/discharge efficiency of MWNT-SnNi are even better. All of these can be explained by the buffering effects of Ni and MWNT in the nanocomposite electrode. The inactive component Ni can absorb the volume change in the local SnNi domain, while the MWNT can buffer the volume expansion in the macrodomain. Consequently, the integrity of the MWNT-SnNi electrode was perfectly preserved. This appears to be a good way to improve the electrochemical stability of MWNT supported nanocomposite anodes. We believe that

this approach to anode materials for lithium ion batteries warrants significant further work. The optimization of MWNT-supported intermetallic composites is being conducted in our Laboratory through tuning the components and material processing.

#### **4.4 Conclusion**

MWNT-Sn and MWNT-SnNi nanocomposites were prepared by a chemical reduction procedure. A high reversible capacity, high charge/discharge efficiency, and fairly good cyclability were achieved for the MWNT-Sn and MWNT-SnNi electrodes. They are intended to utilize the ductile MWNT matrix to buffer the volume expansion in the macrodomain and the inactive Ni component in MWNT-SnNi to absorb the volume change in the local SnNi domain. A reaction model was proposed for the lithiation and de-lithiation processes in the MWNT-Sn and MWNT-SnNi electrodes in lithium ion cells.

## **CHAPTER 5. MESOPOROUS CARBON-TIN NANOCOMPOSITES AS ANODE MATERIALS FOR THE LI-ION BATTERY**

### **5.1 Introduction**

Carbon-based materials have been used extensively as electrode materials for power sources such as lithium ion batteries, fuel cells, and supercapacitors. Since these energy conversion and storage devices have a large market in personal electric devices, stationary residential power, and hybrid electric vehicles (HEVs), much research effort has been focused on the carbon based electrode materials, especially on the nanostructured carbons, such as carbon nanotubes (CNTs), carbon aerogels (CAs), and mesoporous carbons (MCs).

Mesoporous carbons with high surface areas and large pore volumes are employed in various areas of science and technology, including gas and water purification, separation, catalyst support, and energy storage and conversion [220]. Tin-based materials have been widely investigated as anodes for Li-ion batteries since 1997 [117]. Tin oxides are thought to have a two-step reaction with lithium [119]. The initial step involves the irreversible reduction of tin oxide to tin metal particles in a lithium oxide matrix. The second step is the reversible alloying of the  $\text{Li}^+$  into the tin metal. For tin metal, this alloying causes a large volume expansion, resulting in disruption of the material and the eventual loss of capacity. To get good cycling performance, one of the solutions is to use a ‘buffer matrix’ to avoid volume expansion during the lithium alloying and de-alloying processes [221-223].

Therefore, we report here the synthesis of mesoporous carbon-tin nanocomposites as a new type of anode for Li-ion batteries. When we dope tin nanoparticles into the as-prepared mesoporous carbon, especially into the mesopores of the mesoporous carbon materials, the pore structures can act as a matrix to suppress the volume changes of the tin during the lithium alloying and de-alloying processes. Based on this idea, we prepared mesoporous carbon-tin nanocomposite through a two step approach.

## **5.2 Synthesis and characterization of MC-Sn nanocomposite**

### **5.2.1 Synthesis of the mesoporous carbon**

Based on a direct synthesis method for mesoporous carbon [224], sucrose (99% A.C.S. Reagent), aqueous sodium silicate solution (containing ~14% NaOH and ~27% SiO<sub>2</sub>) from Aldrich, and hydrochloric acid (37 wt.% in water) from Merck were used. Firstly, 50 g of sucrose was dissolved in a solution mixture containing 20-50 ml of silicate solution and 20 ml of distilled water solution at 50-80 °C. After complete dissolution, the HCl solution was added, producing a dark brown solution. This mixture was kept for 1 day in a convection oven at 80-100 °C to achieve evaporation of residual water and further polymerization. For carbonization, the mixture was heated under nitrogen atmosphere from room temperature to 200 °C at a heating rate of 3 °C min<sup>-1</sup>, kept at that temperature for 12 h, and then heated further to 850 °C at a heating rate of 5 °C min<sup>-1</sup> and maintained at that temperature for 3 h. The resulting carbon/silica composites were stirred in a 2 M NaOH boiling solution for 5 h to remove the silica template, and the

final carbon materials were retrieved by centrifuge. Large area standardless energy dispersive spectroscopy (EDS) analysis showed that silica was successfully removed down to less than 1 wt% through this process.

### 5.2.2 Mesoporous carbon-tin nanocomposite

Mesoporous carbon-tin nanocomposite was then prepared by reductive precipitation of tin nanoparticles on the as-prepared mesoporous carbon. 50 ml of precipitation agent solution containing 5 g/L NaOH (Merck, 2 M) and 6.25 g L<sup>-1</sup> NaBH<sub>4</sub> (Aldrich, 98%) was added dropwise to 150 ml of tin precursor containing 1.5 g L<sup>-1</sup> SnCl<sub>2</sub>·2H<sub>2</sub>O (Aldrich, A.C.S.) and 3 g/L trisodium citrate dehydrate (Na<sub>3</sub>C<sub>6</sub>H<sub>5</sub>O<sub>7</sub>·2H<sub>2</sub>O) (Aldrich, A.C.S.) under strong stirring. When the reaction finished, the products were separated by centrifuge and carefully washed with distilled water, followed by drying in a vacuum oven overnight at 120°C [225].

### 5.2.3 Microstructure characterization

The as-prepared mesoporous carbon has a unique pore size, with a diameter around 20 nm as measured by Transmission Electron Microscopy (TEM) (Fig. 5-1(a)), as well as a high specific surface area of 381.03 m<sup>2</sup>g<sup>-1</sup> from Brunauer-Emmett-Teller (BET) measurements. TEM images of the mesoporous carbon-tin nanocomposite have given visible evidence that the tin nanoparticles occupy both the pores and the surface of the mesoporous carbon (Fig. 5-1(b)). Tin nanoparticles with diameters around 10-15 nm have homogeneously decorated the mesoporous carbon, and there are no visible spare pores left. X-ray diffraction shows the amorphous state of the mesoporous carbon and

the mesoporous carbon-tin nanocomposite (Fig. 5-2). Large area standardless EDS analysis indicates that the tin nanoparticles are about 18 wt% of the total composite.

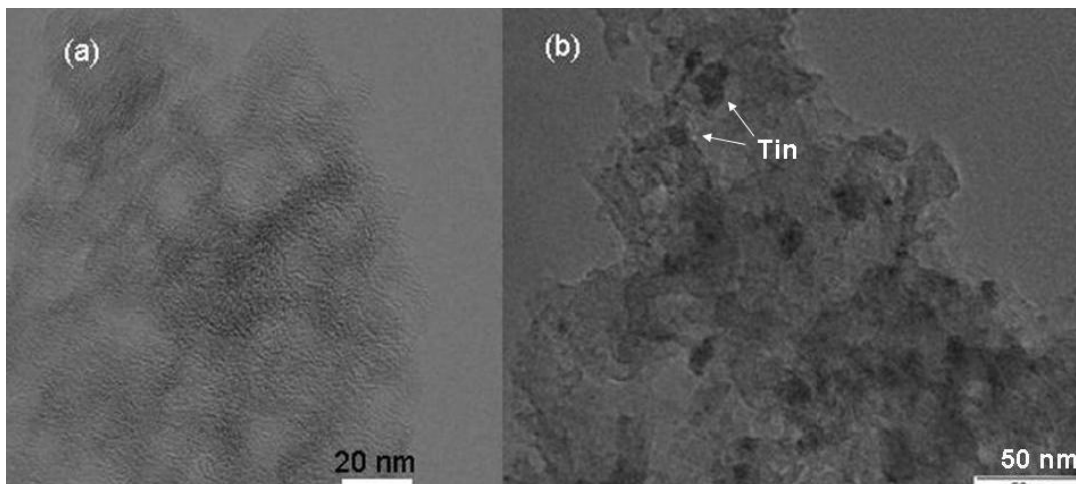


Fig. 5-1 TEM images of the as-prepared samples: (a) TEM image of mesoporous carbon, (b) TEM image of the mesoporous carbon-tin nanocomposite.

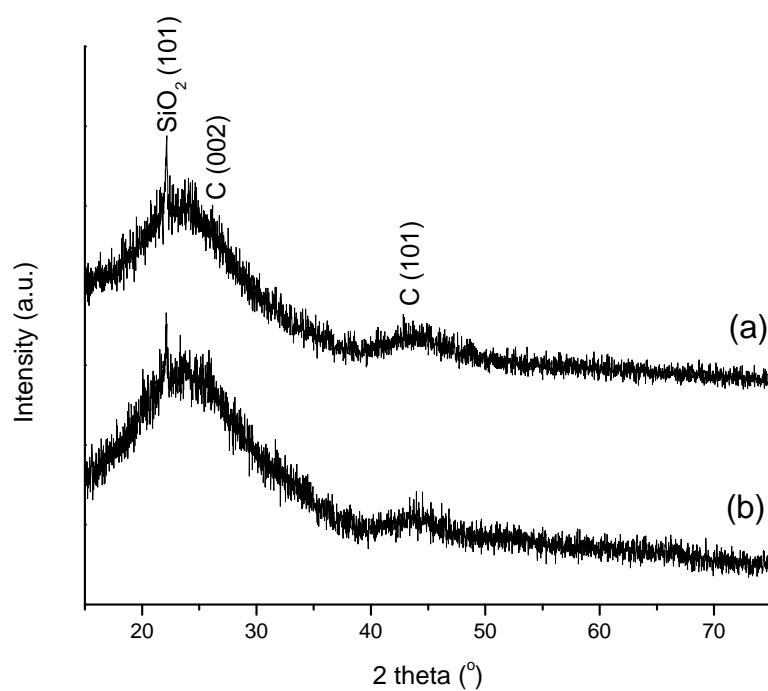


Fig. 5-2 XRD pattern of (a) mesoporous carbon and (b) the mesoporous carbon-tin nanocomposite.

### 5.3 Electrochemical testing of nanocomposite electrodes

Fig. 5-3(a) shows the first three consecutive cyclic voltammograms of the mesoporous carbon-tin nanocomposite at a scan rate of  $0.1 \text{ mV s}^{-1}$ . The first cycle reflects an irreversible reaction with a reduction peak at around 0.5 V. During the following cycles, there are no visible peaks corresponding to the reversible lithium alloying and de-alloying processes. Fig. 5-3(b) shows the first three charge/discharge curves. It can be observed that the initial coulombic efficiency (irreversible capacity:  $1269 \text{ mAh g}^{-1}$ ) is very poor. A solid electrolyte interface (SEI) film is thought to be formed on the surface of the nanocomposite during the first discharging process [226, 227]. Another reason for the poor coulombic efficiency is the large irreversible lithium ion insertion capacity contributed by the mesoporous carbon content. However, after the first cycle, the mesoporous carbon based nanocomposite exhibited excellent cycle stability, with nearly 100% cycle efficiency. The reversible capacity is  $358.26 \text{ mAh g}^{-1}$  after 200 cycles, which is 96.1% of the first cycle reversible capacity ( $372.83 \text{ mAh g}^{-1}$ ) (Fig. 5-3(c)). The capacity fade rate was only 0.0195% per cycle, which is comparable to the performance of commercially available graphite-based anodes. In general, when charging to 0.9 V, Sn-based anodes often display very poor cyclability ( $\sim 3\%$  capacity loss per cycle) [228]. To the best of our knowledge, the cycle stability of the as-prepared mesoporous carbon-tin nanocomposite is better than in any other work reported before [222, 223].

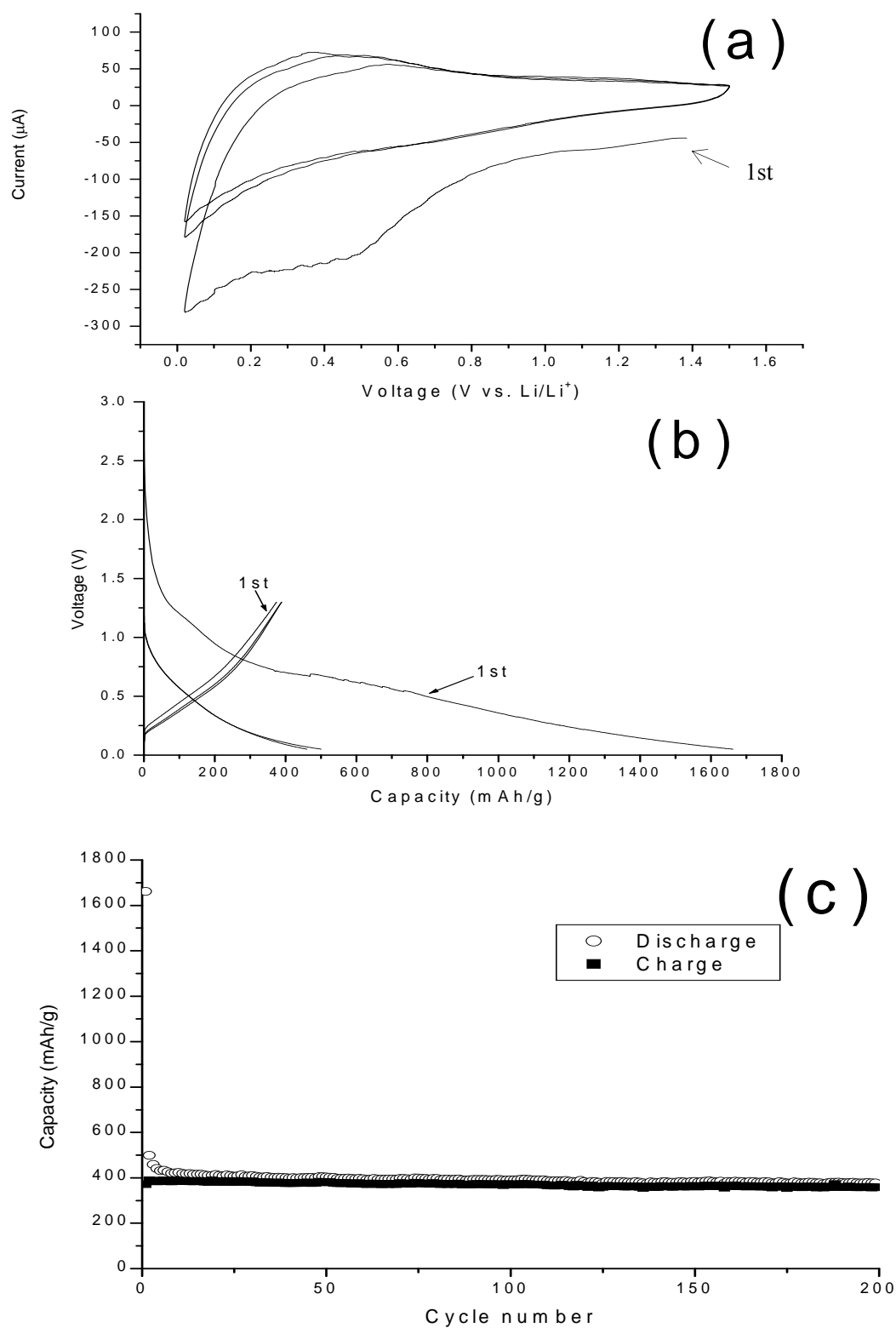


Fig. 5-3 Electrochemical properties of the mesoporous carbon-tin nanocomposite: (a) cyclic voltammograms of the as-prepared nanocomposite, (b) the first three charge/discharge curves, (c) cycling performance.

There are no visible cracks on the electrode even after 200 cycles, as is shown by the SEM images (Fig. 5-4).

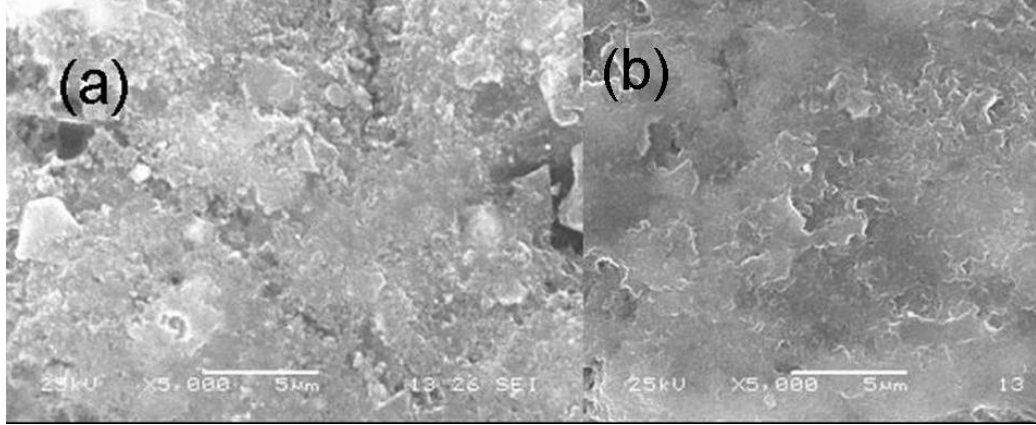


Fig. 5-4 SEM images of mesoporous carbon based tin inset nanocomposite electrode: (a) before cycling, (b) after cycling for 200 times.

On measuring the charge/discharge capacity of mesoporous carbon without tin nanoparticles, we found that it exhibits a reversible capacity of  $243 \text{ mAh g}^{-1}$  during the first cycle (Fig. 5-5).

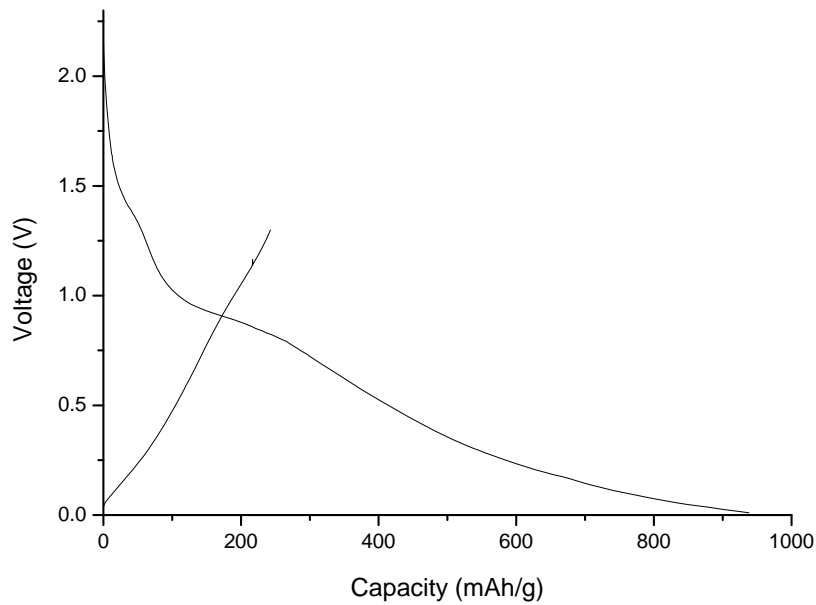


Fig. 5-5 The first charge/discharge curves of bare mesoporous carbon anode.

Since the capacity of the as-prepared nanocomposite with the tin nanoparticles (18% Sn + 82% C) is  $372 \text{ mAh g}^{-1}$  during the first cycle, by subtracting the capacity of the mesoporous carbon component, the reversible capacity delivered by the tin nanoparticles (18 wt%) was estimated to be  $173 \text{ mAh g}^{-1}$ . Therefore, the specific capacity of Sn in the composite electrode was calculated to be  $959.7 \text{ mAh g}^{-1}$ , which amounts to an impressive 96.9% of the theoretical value ( $990 \text{ mAh/g}$ ). This shows the beneficial effect of the mesoporous carbon on the enhanced electrochemical performance of the Sn electrode, which may be attributed to the following factors: (i) the mesoporous structure of the carbon limits the mobility of the Sn insets during cycling and prevents the agglomeration of tin particles, resulting in significantly improved cyclability, surpassing previous reports on Sn-based anodes [228-230]; (ii) the mesoporous structure of carbon buffers well against local volume changes in the Li-Sn alloying and de-alloying cycles; (iii) the mesoporous carbon matrix is responsible for significant improvement to the electric conductivity of the composites; and (iv) the porosity and the large surface area of the nanocomposite are favorable for the diffusion of lithium ions, providing more active sites. A proposed schematic diagram of the mesoporous carbon-tin nanocomposite is shown in Fig. 5-6. As there are some defect sites on both the surface and in the pores of the mesoporous carbon, tin nanoparticles tend to decorate on these sites. During the lithiation and de-lithiation processes, small amounts of the tin nanoparticles isolated on the surface of the mesoporous carbon are broken because of their large volume changes during Li-Sn alloying and de-alloying cycles, while other tin nanoparticles inside the pores or protruding from the pores are preserved. The strategy of using a mesoporous structure to prevent the rapid capacity fading of Sn anode may also be used in overcoming similar problems in other Li-alloying electrode materials such as Si and Sb.

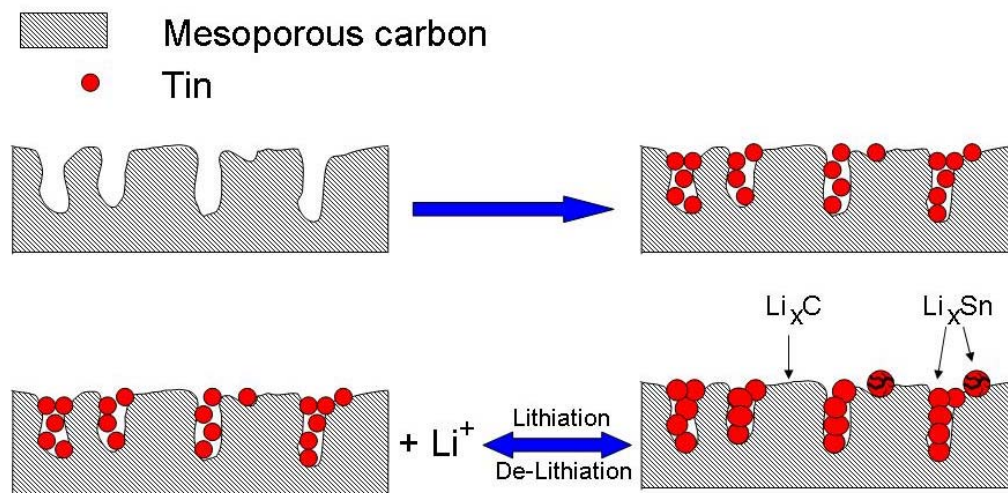


Fig. 5-6 Schematic diagram of mesoporous carbon-tin nanocomposite.

## 5.4 Conclusion

Mesoporous carbon-tin nanocomposite is a promising candidate for use as an anode material for the lithium ion battery. The tin nanoparticles occupy the mesopores of the as-prepared mesoporous carbons, and thus the mesoporous structure of the carbon effectively buffers the volume changes during the Li-Sn alloying and de-alloying cycles, increases the electrical conductivity, and enhances lithium ion transport in the nanocomposite anodes. This provides reversible lithium alloying with tin so that 96.1% of capacity is retained after 200 non-restricted charge/discharge cycles. Although the reversible capacity of the as-prepared composite electrodes is only  $372.83 \text{ mAh g}^{-1}$  due to the relatively low tin content, it is still slightly higher than the real capacity of graphite anodes ( $350 \text{ mAh/g}$ ). Further study will aim at improving the tin loading to obtain higher capacity.

## **CHAPTER 6. TITANIA NANOTUBE SUPPORTED TIN ANODES FOR LITHIUM INTERCALATION**

### **6.1 Introduction**

Inorganic one-dimensional materials, especially oxides and hydrous oxides, have achieved great attention recently. Among them, there is much interest in various applications of titanium based materials as catalyst supports, photocatalysts, semiconductors, gas sensors, and materials for solar energy conversion or lithium ion batteries [231-235]. It has been reported that titania has a higher reversibility and insertion ratio than other compact materials in lithium ion batteries [236, 237]. Moreover, tin metal and oxides have been widely studied after having been discovered as anodes for the lithium ion battery [117, 119]. However, they suffer from capacity fading during the alloying and de-alloying processes with lithium. In previous studies, we tried to use carbon nanotubes to suppress the volume changes during the tin alloying and de-alloying processes [221]. Tin materials were decorated on the surface of the carbon nanotubes, and tangled tubes suppressed the volume expansion. Herein, we report the synthesis of a tin and titania nanotube composite as a novel anode material for lithium ion batteries. Titania nanotubes act as a matrix to suppress the volume expansion of the tin anodes. The relative invariance of the titania nanotube framework and the stability of the morphology provide good retention of charge/discharge capacity on cycling.

## **6.2 Synthesis and characterization of titania nanotube supported tin**

### **6.2.1 Synthesis of the titania nanotube supported tin anodes**

Titania nanotubes were prepared by a previously reported procedure [238]. The  $\text{TiO}_2$  nanoparticles were synthesized by a co-deposition method. After aging, rinsing and desiccation at 90 °C for 6 h in vacuum, anatase  $\text{TiO}_2$  powder were obtained. Then the powders were calcined in a muffle furnace at 110 °C. As-prepared anatase phase  $\text{TiO}_2$  powder (0.15 g) was mixed with 50 ml of NaOH aqueous solution (10 M). The mixture was then encased in a Teflon autoclave, sonicated for 5 min, and heated by microwave irradiation in a reactor at a power of 195 W for 90 min. The products were washed thoroughly with distilled water until the pH value reached 7, then filtered and dried in vacuum at 90 °C. Tin nanoparticles were prepared by reductive precipitation [225]. A precipitation agent solution (50 ml) containing 5 g/L NaOH (Merck, 2 M) and 6.25 g/L  $\text{NaBH}_4$  (Aldrich, 98%) was added dropwise to 150 ml of tin precursor containing 1.5 g/L  $\text{SnCl}_2 \cdot 2\text{H}_2\text{O}$  (Aldrich, A.C.S.) and 3 g/L trisodium citrate dehydrate ( $\text{Na}_3\text{C}_6\text{H}_5\text{O}_7 \cdot 2\text{H}_2\text{O}$ ) (Aldrich, A.C.S.) with 220 mg titania nanotubes under strong stirring. When the reaction finished, the products were separated by centrifuge and carefully washed with distilled water, followed by drying in a vacuum furnace overnight at 120 °C.

### **6.2.2 Characterization of the titania nanotube supported tin anodes**

Fig. 6-1 shows transmission electron microscopy (TEM) images of the titania nanotube supported tin anodes. Based on a previous study [238], the as-prepared titania nanotubes

have diameters of about 12 nm and lengths from around 50 nm to several microns (Fig. 6-1(a)). Their presence in the current investigation was confirmed by selected area electron diffraction (inset, Fig. 6-1(b)) and X-ray diffraction (discussed later). The mechanism for the microwave synthesis of titania nanotubes is proposed to be related to the as-prepared protonic titanate, since titania, either anatase or rutile, does not exhibit a lamellar feature, contradicting the observations of well-resolved layered walls in the nanotubes. Although the accurate composition of protonic titanate is still unknown, the rolling formation mechanism is well accepted, that is, two-dimensional nanosheets of  $\text{TiO}_6$  octahedra connect in an edge-sharing manner with each other, and then roll up into multiwall spiral nanotubes, with  $\text{H}_2\text{O}$  loosely attached in the interlayer space [239, 240]. From the TEM images (Fig. 6-1), tin particles (also confirmed to be present by EDS spot analysis) can be found on the surface of the titania nanotubes. Some of the tin particles tended to agglomerate to form relatively big particles, however, most of them had a characteristic small particle size (around 10 nm) and were well decorated on the titania nanotubes (Fig. 6-1(b)–(d)). Some of the tubes have overlapped and joined together (Fig. 6-1(b) and (c)). The tubal morphology of titania nanotubes is stably retained (Fig. 6-1(b)–(d)).

From the SEM images (Fig. 6-2), it also can be seen that the tubal nanostructure is well maintained. Large area standardless EDS analysis indicates that the tin particles are about 9.5 wt% of the total composite. A trace amount of oxygen was also found in the EDS spectrum from Sn particles (Fig. 6-1(e)), which may come from absorbed air or a small amount of  $\text{SnO}_2$  particles in the composite. However, as the atomic ratio of O and Sn is far lower than two, the tin atoms in the composite mainly exist as tin, not tin oxide.

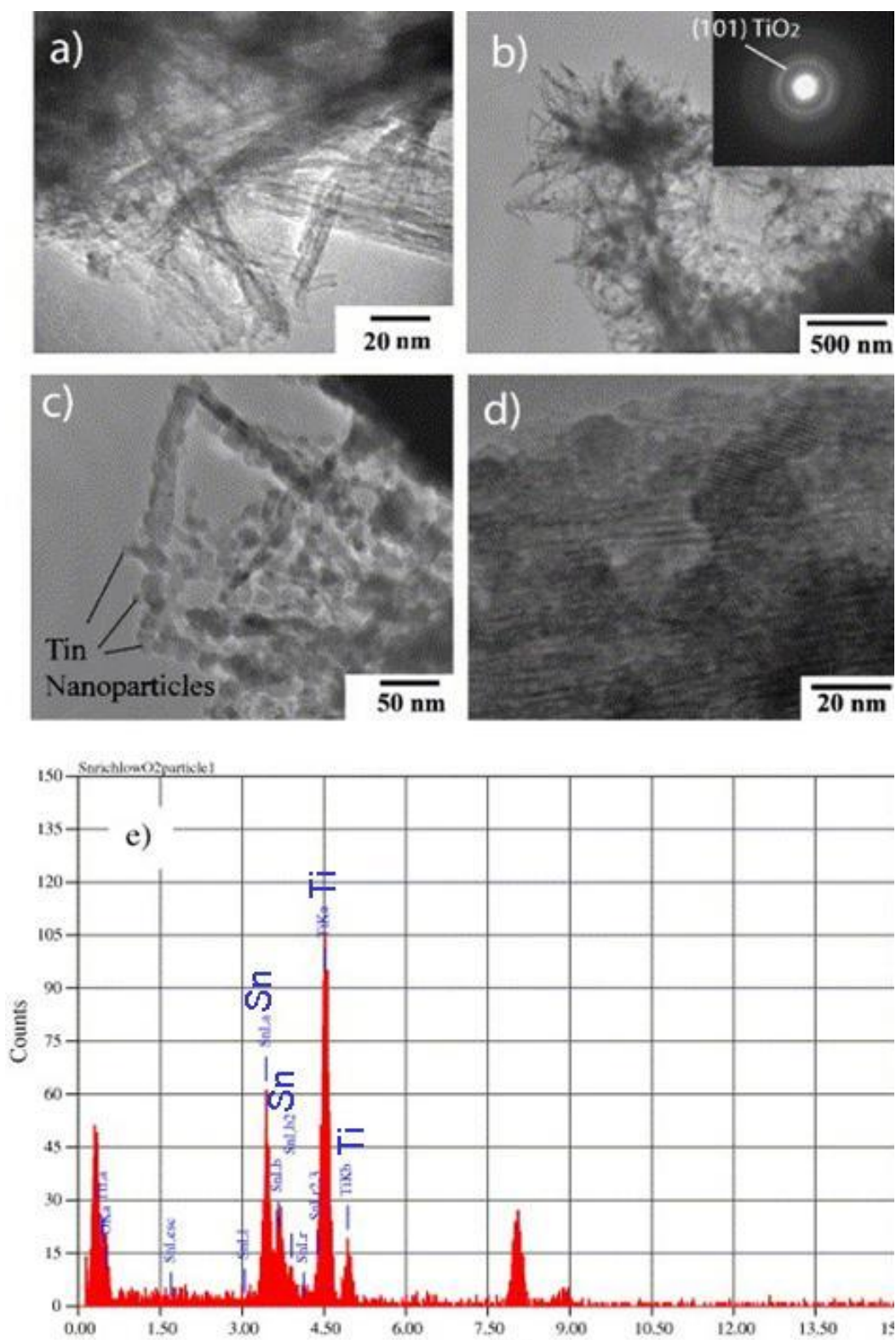


Fig. 6-1 TEM images of (a) the bare titania nanotubes, (b–d) titania nanotube supported tin anodes at different magnifications (inset in (b) is a selected area diffraction pattern from a large region), and (e) the EDS spectrum from a Sn particle.

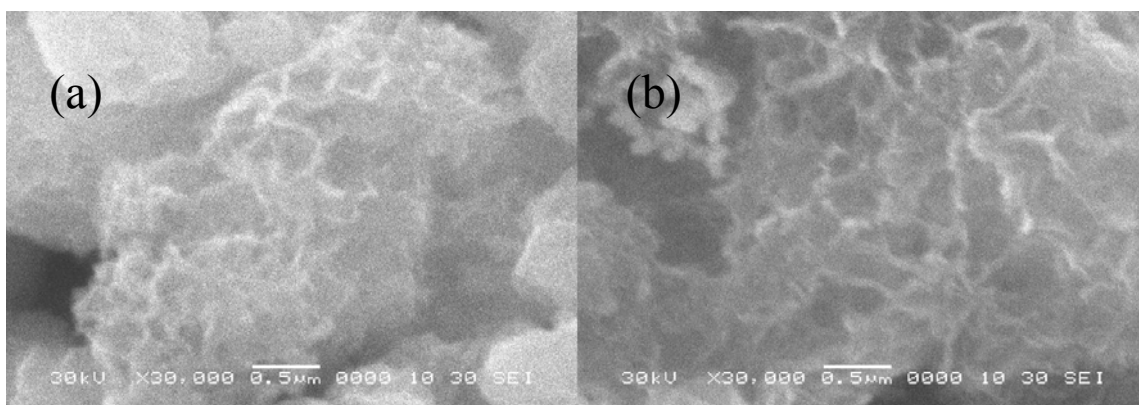


Fig. 6-2 SEM images of (a) the bare titania nanotubes and (b) titania nanotube supported tin anodes.

The XRD patterns of the as-prepared titania nanotubes without tin particles are shown in Fig. 6-3(a). After the tin inset insertion procedure, there are no obvious tin peaks, as can be seen in Fig. 6-3(b), and all the peaks can be indexed to anatase titania nanotubes. This may be because the tin inset grains are too small to be detected by X-ray diffraction.

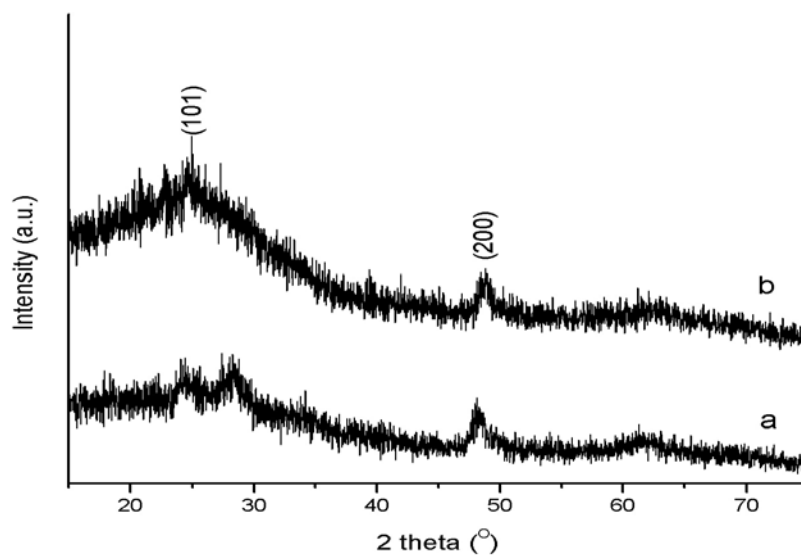


Fig. 6-3 XRD patterns of (a) the bare titania nanotubes and (b) titania nanotube supported tin anodes.

### 6.3 Electrochemical properties of titania nanotube supported tin anodes

Fig. 6-4 shows the charge/discharge curves and the cycling performance of an electrode made of titania nanotube supported tin using the constant current charge/discharge mode. For comparison purposes, the cycling performance of the bare  $\text{TiO}_2$  nanotube electrode and a bare nanocrystalline Sn electrode are also shown in Fig. 6-4. (Sn nanoparticles were synthesized by the same method but in the absence of  $\text{TiO}_2$  nanotubes.) The bare  $\text{TiO}_2$  nanotube electrode is relatively stable on cycling, but with limited capacity. The bare nanocrystalline Sn anode has a higher initial reversible capacity (600 mA h/g), however, its capacity fades rapidly on cycling. Furthermore, this value is still much lower than the theoretical capacity (990 mA h/g) of the bare Sn electrode. Therefore, it is not appropriate to use nanocrystalline Sn alone as an electrode in Li-ion cells. In contrast, the Sn/ $\text{TiO}_2$  composite electrodes demonstrate superior cyclability compared to the bare nano-Sn electrodes. The initial reversible capacity of the electrode is 281 mA h/g, while 203 mA h/g remains after 50 cycles. By carefully comparing the cycling performance of Sn/ $\text{TiO}_2$  with that of the bare  $\text{TiO}_2$  nanotube electrode, it is found that the cycling stability of Sn/ $\text{TiO}_2$  is slightly better than that of the Sn-free  $\text{TiO}_2$  nanotube electrode. The results demonstrate that the tubal nanostructure of  $\text{TiO}_2$  can effectively buffer the volume expansion of the tin particles during alloying and de-alloying with lithium. In the meanwhile, the Sn coating on the surface of the  $\text{TiO}_2$  nanotubes can suppress the deterioration of the  $\text{TiO}_2$  electrode during  $\text{Li}^+$  intercalation/de-intercalation cycling. For the Sn/ $\text{TiO}_2$  nanotube electrodes, there are no clear potential plateaus during the charge/discharge process. The loss due to the irreversible capacity in the first cycle is very high. This first cycle loss is due to the formation of the electrochemically inert  $\text{Li}_2\text{O}$

to the solid electrolyte interface (SEI) film, to a certain fraction of the lithium ions that are strongly trapped in the dangling bonds, and to the imperfection of the surface structure [231].

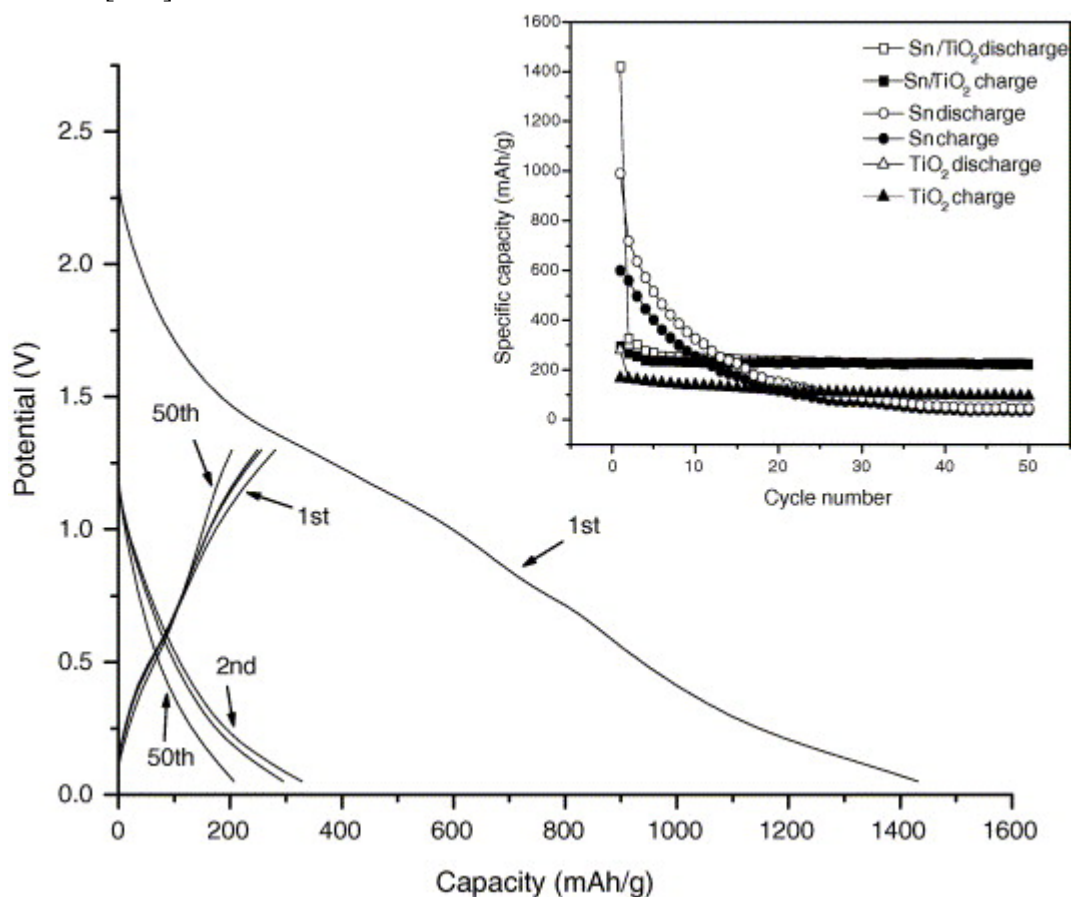


Fig. 6-4 The charge/discharge curves of titania nanotube supported tin anodes and the cycle performance (inset) of TiO<sub>2</sub> nanotube supported tin, and TiO<sub>2</sub> nanotube electrodes.

The Li-ion electrochemistry at the tin oxide anode can be described in two steps, which can be expressed as follows ([119] and [117]):  $4\text{Li}^+ + \text{SnO}_2 + 4\text{e}^- \rightarrow \text{Sn} + 2\text{Li}_2\text{O}$ ;  $x\text{Li}^+ + \text{Sn} + x\text{e}^- \leftrightarrow \text{Li}_x\text{Sn}$  ( $0 \leq x \leq 4.4$ ). Tin oxides first decompose into a Li<sub>2</sub>O matrix and Sn metal, then the tin particles alloy and de-alloy with lithium ions. The dramatic volume changes associated with the insertion/de-insertion of lithium ions in the structure

inevitably pulverize the alloy particles. The consequent loss of connectivity with the conducting additive particles causes poor cyclability in practice. For titania nanotubes, the lithium insertion/extraction to/from  $\text{TiO}_2$  (anatase) proceeds according to the following reversible reaction:  $\text{TiO}_2 + x\text{Li}^+ + xe^- \leftrightarrow \text{Li}_x\text{TiO}_2$ . The maximum  $x$  for the reversible reaction of normal crystalline anatase  $\text{TiO}_2$  at room temperature is reported to be 0.5 [241], which corresponds to a capacity of 168 mA h/g. During the insertion process, the crystal structure of  $\text{Li}_x\text{TiO}_2$  changes from tetragonal  $\text{Li}_{0.05}\text{TiO}_2$  to orthorhombic  $\text{Li}_{0.5}\text{TiO}_2$ , which causes the coexistence of the two phases for  $0.05 < x < 0.5$  and gives a constant potential of about 2 V vs.  $\text{Li}/\text{Li}^+$  in this region [242]. The columbic efficiency of the titania nanotube supported tin anodes tends to be 100% after the first cycle, indicating the good reversibility of the lithium intercalation process and the consequent cyclability.

Fig. 6-5 shows cyclic voltammograms (CVs) of a titania nanotube and tin composite electrode. For comparison purposes, CV curves of bare  $\text{TiO}_2$  nanotube anode and bare Sn anode are also shown. The lithium insertion potential in the  $\text{TiO}_2$  nanotube electrode is around 0.7 V vs. the  $\text{Li}/\text{Li}^+$  reference electrode, whereas the potential for lithium de-intercalation is at about 1.0 V. We think that the presence of interstitial  $\text{TiO}_2$  and the strong binding with inserted lithium give rise to the large hysteresis. For the bare Sn electrode, the irreversible peak of electrolyte decomposition in the first cycle above 1.0 V can be clearly seen. There are roughly three pairs of other cathodic/anodic peaks that can be observed. A shoulder at about 0.5 V vs.  $\text{Li}/\text{Li}^+$  is also present on the negative-potential side of the anodic peak at 0.65 V vs.  $\text{Li}/\text{Li}^+$ . These peaks originate from the phase transitions between  $\text{Li}_2\text{Sn}$ ,  $\text{LiSn}$ ,  $\text{Li}_7\text{Sn}_3$ ,  $\text{Li}_5\text{Sn}_2$ , and  $\text{Li}_{22}\text{Sn}_5$ , respectively

[218]. However, the cyclic voltammogram of the Sn/TiO<sub>2</sub> nanocomposite electrode is totally different from those of the Sn or TiO<sub>2</sub> nanotube electrodes. Only one anodic peak (0.6 V) was observed in the cyclic voltammogram of Sn/TiO<sub>2</sub> nanotube composite electrode. The reason for this phenomenon is not clear yet, but the CV curves of Sn/TiO<sub>2</sub> are quite similar to those of SnNi anodes that we previously studied [221]. It seems that as long as Sn particles are dispersed in an electrochemically inactive matrix or a matrix with electrochemical activity in a different voltage range, the sharp peaks in their CV curves can be barely seen. For the same reason, the anodic peak in the CV of TiO<sub>2</sub> anode can hardly be seen in the CV of Sn/TiO<sub>2</sub> anode either. The total charging–discharging behavior of Sn/TiO<sub>2</sub> can be explained by the following reaction:



The dramatic decrease in the discharge capacity during the first few cycles is related to the nanoscale morphology changes in the TiO<sub>2</sub> [243]. This kind of surface morphology change may mainly be due to the traces of water adsorbed on the surface due to the large specific surface area of the titania nanotubes. These trace amounts of water will be consumed by the side reaction occurring over the low voltage range in the cathodic branch. Consequently, this side reaction may result in a relatively large first discharge capacity, but the influence will be eliminated because of the consumption of the traces of water during the subsequent cycling. The consumption of this surface adsorbed water will reveal the fresh surface of the TiO<sub>2</sub> nanotubes, which will ensure good cyclability and rate capacity of the electrode [244]. From the second cycle, the cathodic or anodic curves remain unchanged, suggesting excellent cycling stability for this new anode.

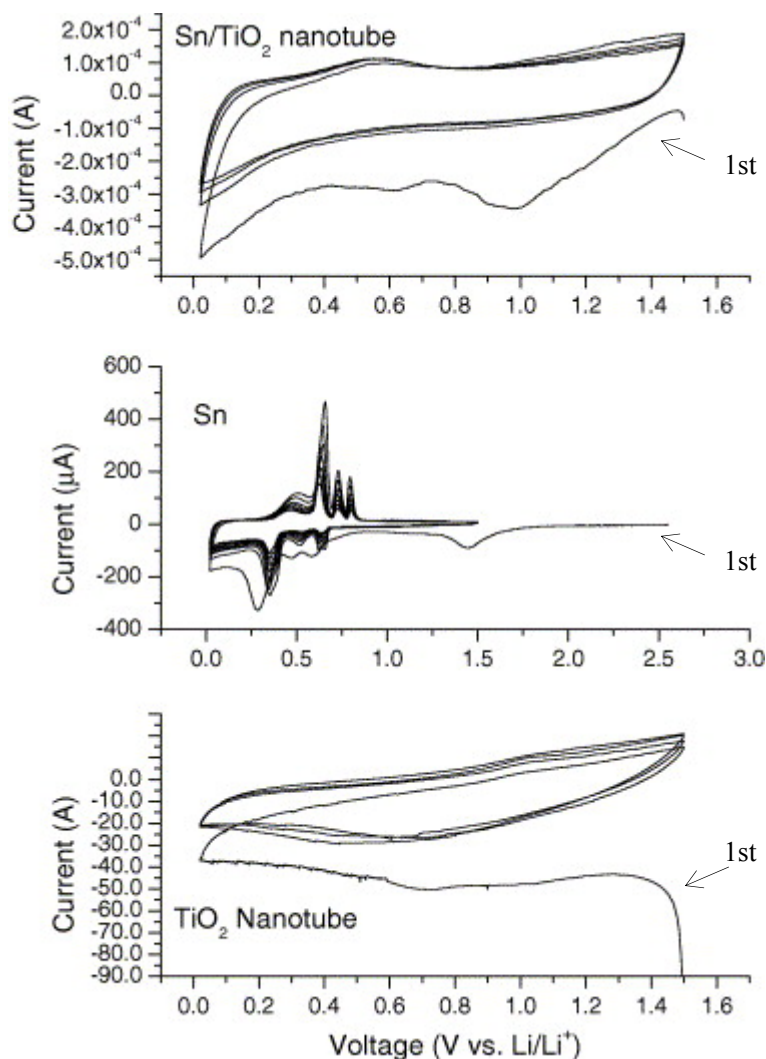


Fig. 6-5 Cyclic voltammograms of TiO<sub>2</sub> nanotube supported tin, tin, and TiO<sub>2</sub> nanotube anodes.

Moreover, to investigate the electrochemical behavior of the Sn/TiO<sub>2</sub> nanotube composite electrodes in detail, they were charged/discharged over different voltage ranges. The variation of discharge capacity with cycle number over different voltage ranges is shown in Fig. 6-6. With the cut-off voltage increasing, the capacity increases, but the cycling stability of the composite electrode decreases. When the composite electrodes were cycled between 0.05 and 2.0 V, they had a capacity of around 550 mA h/g in the second cycle and delivered a capacity of 312 mA h/g after 50 cycles, which is quite promising compared to other anode materials. Since the tin particles in the

titania nanotubes represent only 9.5 wt%, to increase the reversible capacity for lithium intercalation, subsequent work will aim at improving the extent of decoration and reducing the presence of agglomerated particles decorated on the surfaces.

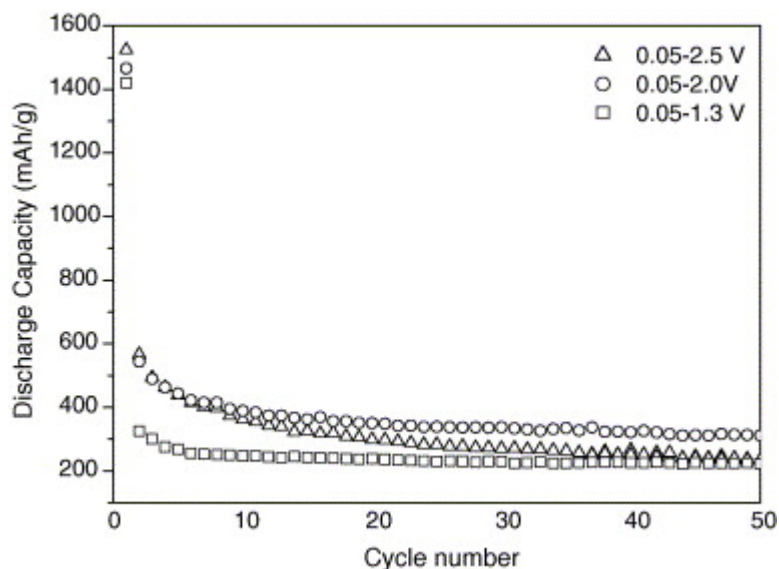


Fig. 6-6 Discharge capacity vs. cycle number for titania nanotube supported tin anodes.

## 6.4 Conclusion

Novel titania nanotube supported tin anodes were prepared for lithium ion batteries. The unique tin nanoparticles are well decorated on the titania nanotubes. The reversible capacity retained is 312 mA h/g (cycled between 0.05 and 2.0 V) and 203 mA h/g (cycled between 0.05 and 1.3 V) after 50 cycles, respectively, with nearly 100% cycle efficiency. The tubal nanostructure can suppress the volume expansion of the tin particles during alloying and de-alloying with lithium. The cyclic performance for lithium intercalation is improved by this new tin and titania composite.

## **CHAPTER 7. NOVEL IONIC LIQUID SUPPORTED SYNTHESIS OF PLATINUM BASED ELECTROCATALYSTS ON MULTIWALLED CARBON NANOTUBES**

### **7.1 Introduction**

Direct methanol fuel cells (DMFC) have recently been attracting great interest for their potential as clean and mobile power sources. Noble metals, such as Pt, Ru or PtRu alloys, supported on high surface area carbons are typically used as electrocatalysts for DMFCs. As noble metals are expensive, the synthesis of these metal particles as electrocatalytic materials with uniform size and good dispersion on the carbon supports has thus become essential.

Many investigators have demonstrated that carbon nanotubes (CNTs) can be used as catalyst supports [171, 172, 175, 245, 246]. Quinn et al. [247] recently described the electrodeposition of noble metal nanoparticles on carbon nanotubes under potential control. The metal particles can decorate the external walls of the CNTs, resulting in hybrid materials with high electrocatalytic activity. Since the CNTs are chemically inert, it is essential to activate their surfaces. Chemical treatments are common methods to generate functional groups on CNTs [176, 248-250]. Generation of functional groups on the surface of CNTs can improve the reactivity and provides an avenue for further chemical modification of the carbon nanotubes, such as by ion adsorption, metal deposition, and grafting reactions. It has been found that the chemical modification of

the surface of CNTs by using  $\text{HNO}_3$  or a  $\text{H}_2\text{SO}_4$ – $\text{HNO}_3$  mixture can improve the metal dispersion. However, it is difficult to decorate metal nanoparticles on the surface of CNTs so that they have uniform size and good dispersion. One of the reasons is that the metal nanoparticles are spontaneously formed at the defect sites on the surface of the CNTs. Moreover, carbon nanotubes tend to agglomerate without any pretreatments.

In this chapter, Pt nanoparticle decorated CNTs have been successfully synthesized by using novel ionic liquid (IL) modified CNTs. ILs are liquids at room temperature and represent a new series of non-aqueous, but polar solvents, which are non-volatile, exhibit high conductivities, and have no vapor pressure [251-255]. The monodispersed Pt nanoparticles on modified CNTs were prepared by a microwave-heated polyol process, which has been demonstrated to be an effective way to prepare polymer stabilized metal nanoparticles, such as Pt, Ag, Au, and Pd [51, 183, 186, 187]. Ethylene glycol is commonly used as the solvent due to its high dielectric constant (41.4 at 298 K) and dielectric loss, and because it can be rapidly heated by microwave radiation. Fast heating rates can accelerate the formation of the Pt nanoparticles, and the uniform microwave irradiation provides more homogeneous circumstances for the nucleation and growth of the Pt nanoparticles.

## **7.2 Synthesis and characterization of the Pt/CNT nanocomposite**

### **7.2.1 Microwave heated synthesis of Pt/CNTs**

The multiwalled CNTs were prepared by catalytic CVD using nanosized cobalt as the catalyst [221]. The CNTs were purified in concentrated  $\text{HNO}_3$  at 393 K for 2 h. Pt/CNT catalysts were synthesized from a microwave heated  $\text{H}_2\text{PtCl}_6$  ethylene glycol (EG) solution containing ionic liquids. 1-Ethyl-3-methylimidazolium bis(trifluoromethylsulfonyl)imide ( $\text{EMI} \cdot \text{TFSI}$ ) and 1-butyl-3-methylimidazolium bis(trifluoromethylsulfonyl)imide ( $\text{BMI} \cdot \text{TFSI}$ ) were synthesized as described previously [256]. The schematic structure of  $\text{EMI} \cdot \text{TFSI}$  is shown in Fig. 7-1. The ionic liquids were dried at 100 °C by bubbling nitrogen through them in a conical flask on a hot plate for 3 h before using. In a typical procedure, 0.05 M  $\text{H}_2\text{PtCl}_6$  solution was obtained by dissolving 1 g of  $\text{H}_2\text{PtCl}_6 \cdot 6\text{H}_2\text{O}$  (Aldrich, A.C.S. Reagent) in 38.6 ml EG (Aldrich). 1 ml of this solution was mixed with 10 ml ionic liquid, 25 ml of EG, and 0.4 ml of 0.4 M KOH in a beaker. The CNTs were pretreated with  $\text{HNO}_3$  (0.04 g) and then sonicated in the mixed solution. The beaker was placed in the center of a household microwave oven and heated for 20 s under microwave power of 800 W, at which point Pt particles were reduced from the solution [187]. The as-prepared suspension was filtered, and the residue was washed with acetone and de-ionized water. The products were dried in a vacuum oven at 393 K overnight.

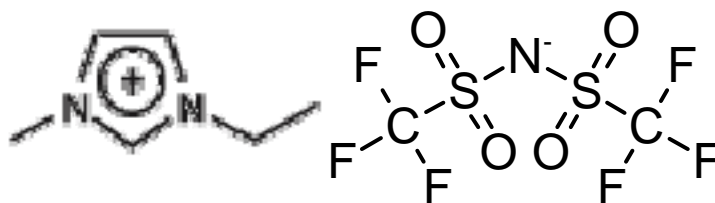


Fig. 7-1 Schematic structure of 1-ethyl-3-methylimidazolium bis(trifluoromethylsulfonyl)imide ( $\text{EMI} \cdot \text{TFSI}$  or  $\text{EMI} \cdot \text{TfSA}$ ) ionic liquid (IL).

### 7.2.2 Characterization of the Pt/CNT nanocomposites

Since the CNTs prepared by the catalytic CVD method are accompanied by many other types of carbon particles, it is essential to use a strong oxidant to purify the raw carbon nanotubes. The CNTs used in this work were pretreated with  $\text{HNO}_3$  at 393 K, which could result in many functional groups, such as carboxyl, hydroxyl, and carbonyl groups, on the surface of the CNTs. By a coordination reaction or an in-exchange reaction, platinum ions interact with and attach to these functional groups on the surface of the oxidized CNTs, and then these functional nucleation precursors are reduced to Pt nanoparticles by a microwave-heated process. Fig. 7-2 shows the X-ray diffraction patterns obtained from the microwave synthesized Pt/CNTs and commercial Pt/C (Vulcan XC-72) catalysts (Johnson Matthew). The diffraction peaks at  $2\theta = 26.5^\circ$  can be attributed to the graphite structure (0 0 2) of the CNTs, while a rather broad peak at  $2\theta = 25^\circ$  can be indexed to XC-72 carbon in the case of the commercial Pt/C catalyst. The results also show that the Pt on both the XC-72 and CNT supports has a face centered cubic structure and has major peaks at around  $2\theta = 39.7^\circ$  (1 1 1),  $46.2^\circ$  (2 0 0),  $67.4^\circ$  (2 2 0), and  $81.2^\circ$  (3 1 1). The mean particle size can be estimated using Scherrer's formula based on the (2 2 0) peak (Table 7-1). It is well known that the smaller metal particles exhibit higher electrocatalytic activity because of their higher specific surface area. The sample of microwave synthesized Pt/CNTs without ionic liquid support (Fig. 7-2(d)) has bigger Pt particles compared to the others. The sample of microwave synthesized Pt/CNTs with BMI · TFSI ionic liquid support (Fig. 7-2(b)) shows good agreement with the commercially obtained catalyst (Fig. 7-2(a)). The EMI · TFSI supported synthesized sample (Fig. 7-2(c)) has an even smaller particle size. Therefore,

EMI · TFSI was used in the following parts as the default ionic liquid. These results suggest that the ionic liquid contributes to the formation of small Pt particles in the microwave-heated polyol process.

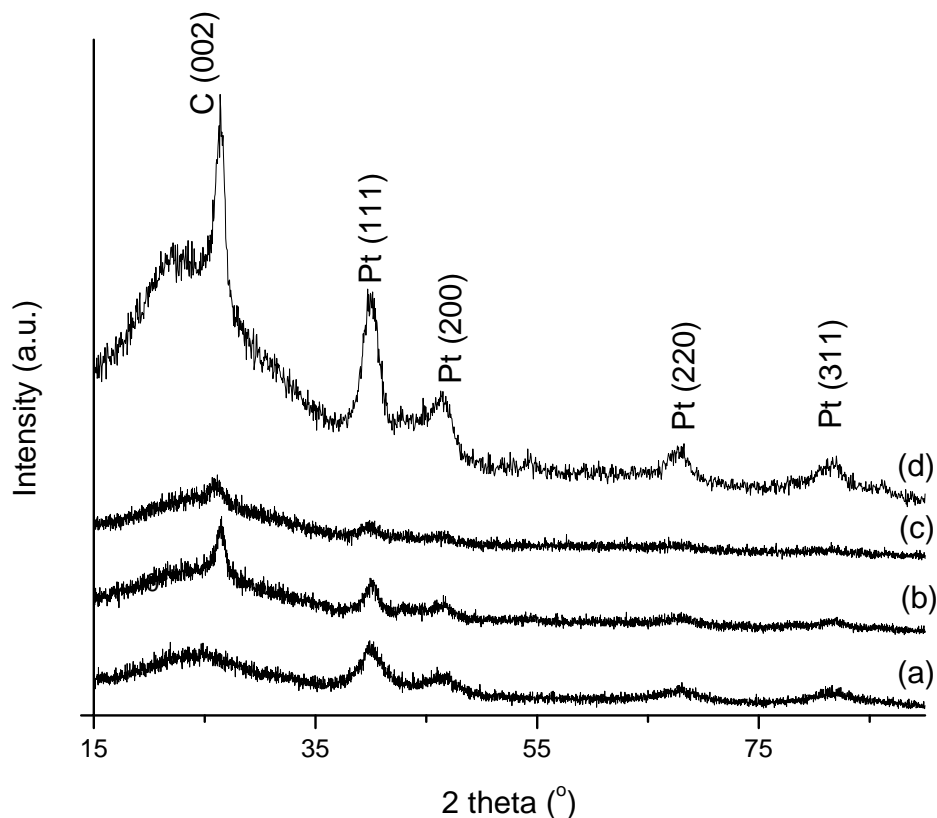


Fig. 7-2 XRD patterns of Platinum based catalysts (a) commercial Pt/C (JM); (b) BMI · TFSI IL supported synthesized Pt/CNTs; (c) EMI · TFSI IL supported synthesized Pt/CNTs; (d) as-prepared Pt/CNTs without IL support.

Table 7-1 Pt nanoparticle sizes calculated by Scherrer's formula based on the XRD pattern (220) peak.

Sample	Commercial Pt/C	Bare Synthesized Pt/CNT	BMI.TFSI-Pt/CNT	EMI.TFSI-Pt/CNT
Mean particle size (nm)	3.10	8.55	6.21	3.13

The general distribution of Pt nanoparticles on the surfaces of the CNTs is shown in the TEM bright-field, dark-field, and selected area electron diffraction (SAED) patterns in Fig. 7-3, and in the SEM images and X-ray maps of Fig. 7-4. The surfaces of the CNTs were decorated by individual Pt nanoparticles, such as those shown in the bright-field dark-field pair, Fig. 7-3(a) and (b), and in the high resolution dark field image (Fig. 7-3(d)), with average particle sizes around 3–6 nm. All the dark-field images in Fig. 7-3 were obtained using part of the first spotty  $(1\ 1\ 1)_{\text{Pt}}$  ring indicated in the inset SAED patterns, resulting in a minor fraction of the Pt particles showing up in the associated dark-field images. Dark-field imaging also revealed regions with uniform rows of nanoparticles located on the nanotube edges, such as those shown in Fig. 7-3(c). Many of the Pt particles were uniformly dispersed on the defect sites of the CNTs. It is believed that much of the catalytic activity, electron transfer, and chemical reactivity of carbon electrodes takes place at surface defect sites and, in particular, at edge-plane defect sites [257].

The multiwalled carbon nanotubes consist of several concentric tubes of graphite fitted one inside the other (high resolution inset, Fig. 7-3(d)). As the axis of the graphite planes is at an angle to the nanotube itself, a high proportion of the graphite sheets must terminate at the surface of the tube, giving rise to a large number of edge-plane or edge-plane-like defect sites along the surface of the tube. The electrocatalytic properties of carbon nanotubes are suggested to result from these edge-plane-like sites, which occur at the open ends of the nanotubes [258].

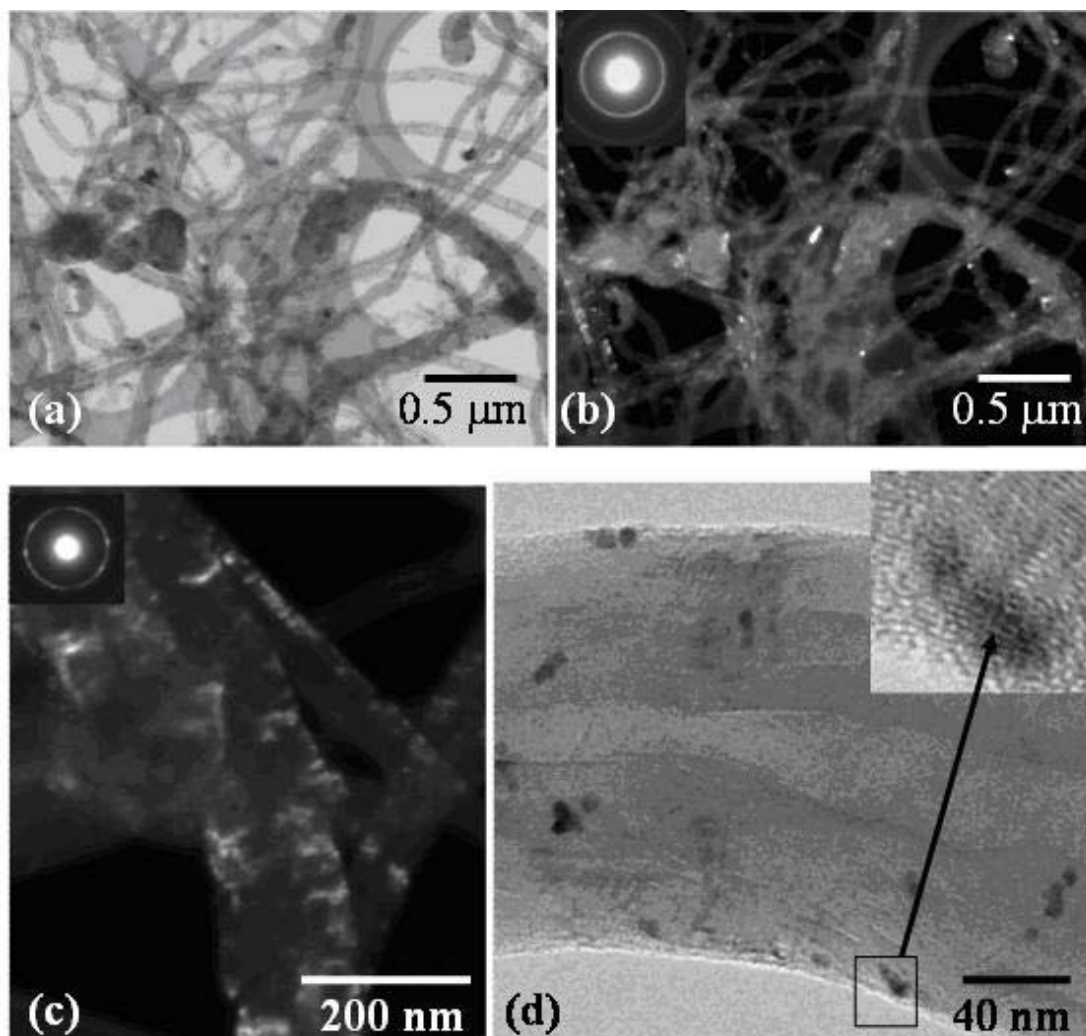


Fig. 7-3 TEM images of Pt nanoparticles decorated on the IL (EMI · TFSI)-modified multiwalled carbon nanotubes: (a) bright-field image and (b) associated dark-field image, (c) higher magnification dark-field image showing Pt particles decorating both sides of the CNTs, (d) bright-field image showing individual Pt particles and carbon nanotube lattice fringes (inset image). Dark-field images (b) and (c) were obtained using Pt (1 1 1) reflections of the first spotty ring in the SAED patterns (inset at the top right of the dark-field images).

By comparing the SEM images, it can be seen that the pristine CNTs curl in some specific parts (Fig. 7-4(a)), while the CNTs in the IL-supported synthesis system exhibit ‘untangled’ morphology (Fig. 7-4(b)). Moreover, by using energy dispersive

spectroscopy (EDS) mapping, it was found that the Pt/CNT sample synthesized with the ionic liquid support has the better dispersion (Fig. 7-4(c) and (d)). There are some brighter areas in Fig. 7-4(c) compared to Fig. 7-4(d), indicating the agglomeration of Pt nanoparticles on the bare Pt/CNT catalysts. The amount of Pt nanoparticle catalyst loaded on the CNT supports was also estimated by semi-quantitative EDS (Table 7-2).

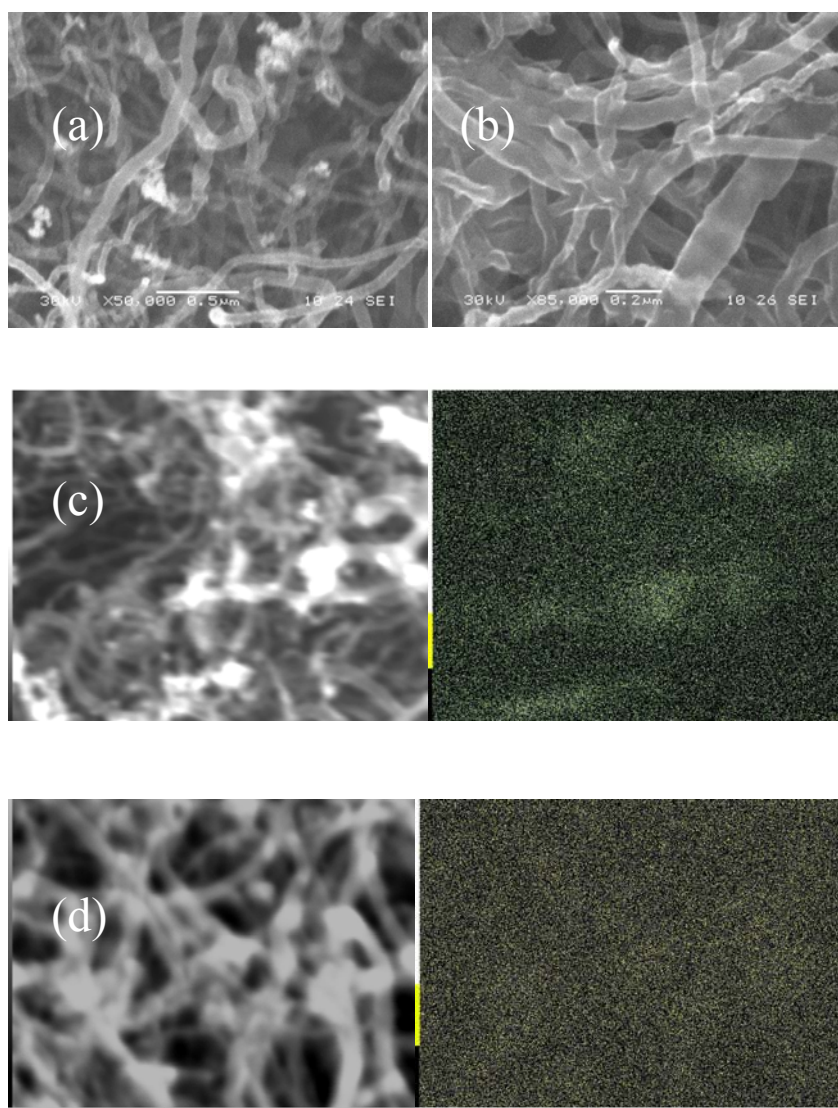


Fig. 7-4 SEM secondary electron images and associated Pt X-ray maps obtained from Pt/CNT samples prepared, (a) and (c), without IL support; (b) and (d) were prepared with the EMI · TFSI ionic liquid support.

Table 7-2 Amount of the Pt nanoparticle catalyst loaded on the CNT supports, as estimated by standardless EDS analysis of large sample areas.

Catalysts	Pt/ wt%	C/ wt%
Bare Pt/CNT	2.91	97.09
IL-supported Pt/CNT	5.75	94.25

CNTs with an untangled structure are supposed to be more suitable for uniform decoration of Pt particles on the surface of multiwalled CNTs. Therefore, ionic liquids and the microwave-heated polyol process are suggested as suitable to improve the Pt particle dispersion and suppress CNT tangling. This may be due to the higher degree of disorder of the CNTs in the IL-supported synthesis system, which has been proved from the Raman spectra (Fig. 7-5). Two main peaks were observed at around 1324 and 1574  $\text{cm}^{-1}$ , which are designated as the D band and G band [259]. For the IL-supported Pt/CNT sample, there is another shoulder band at about 1620  $\text{cm}^{-1}$ , which may be related to the upward shift of the G band. The relative intensity ratio of the D and G bands,  $I_D/I_G$ , is known to depend on the structural characteristics of carbon [260]. The ratio can give information about the perfection of the graphite layer structure, reflecting the properties of the edge plane or boundary of the graphite crystal faces. As the  $I_D/I_G$  ratio increases, the defect structure increases and the degree of graphitization becomes less [261]. The  $I_D/I_G$  ratios are listed in Table 7-3. The IL-supported Pt/CNT has the highest  $I_D/I_G$  ratio, indicating that the CNTs in the ionic liquid support synthesis system have more defect sites and a lower degree of graphitization.

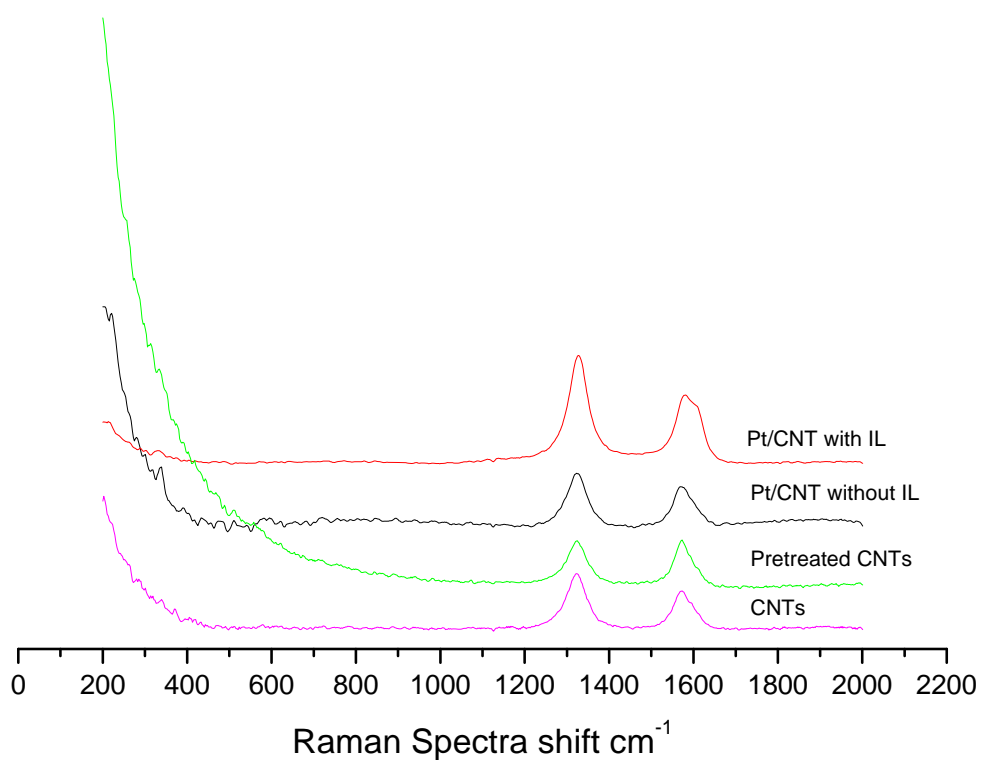


Fig. 7-5 Raman shifts of (a) as-prepared CNTs, (b) acid pretreated CNTs, (c) bare Pt/CNTs prepared without IL support, and (d) IL supported synthesized Pt/CNTs.

Table 7-3 The intensity ratio of the D and G bands ( $I_D/I_G$ ) obtained from the Raman shift.

Samples	$I_D/I_G$
CNTs	1.48
Acid Treated CNTs	1.00
Bare Pt/CNTs	1.41
IL-supported Pt/CNTs	1.59

### 7.3 Electrochemical properties of Pt/CNTs

Cyclic voltammetry (CV) is one of the most common techniques in electrochemical studies of fuel cell reactions. Fig. 7-6 shows the cyclic voltammetry results on the Pt/CNTs synthesized with and without IL support and on the commercial Pt/C catalyst. There are two ways to express the catalytic activity, which are mass activity and specific activity. The mass activity has more practical value in fuel cells, since the costs of the electrodes depend on the amount of Pt used, while the specific activity just shows the Pt electrocatalytic activity on the particle surface. So in this Chapter, the CV plot is presented with the ordinate in milliamperes per milligram of Pt. It can be seen that the IL-supported Pt/CNT catalyst produced the highest specific current in the hydrogen region. This result is believed to be due to the high dispersion of the IL-supported Pt/CNT catalysts. The specific electrochemical surface area (ECA) of Pt (sometimes referred to as the real Pt catalyst surface area) was calculated by integrating the CV curves in the hydrogen absorption region, by assuming that the charge per real  $\text{cm}^2$  of Pt with monolayer adsorption of hydrogen is  $210 \mu\text{C}/\text{cm}^2$  [262]. From the calculation results in Table 7-4, the specific electrochemical surface area of our IL-supported Pt/CNT catalyst is 21% higher than that of the commercial Pt/C (Vulcan XC72) catalyst. It is believed that this approach to Pt/CNT catalyst warrants significant further work. Higher Pt loading catalysts are being produced in our laboratory through tuning the preparation parameters.

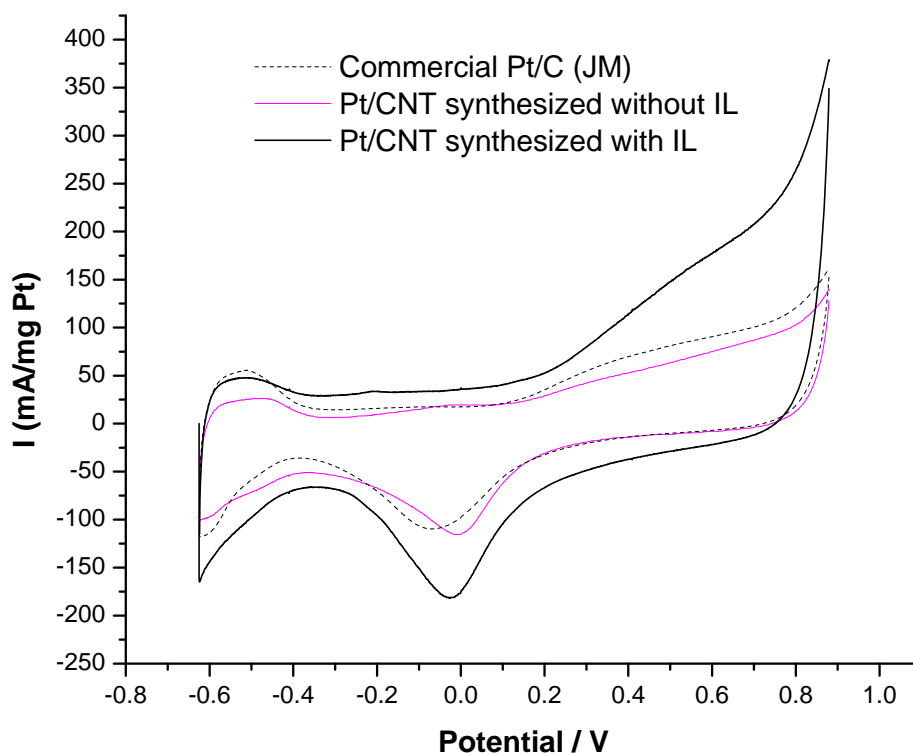


Fig. 7-6 Cyclic voltammograms obtained from synthesized Pt/CNT catalyst with and without IL support, and from the commercial catalyst in 0.5 M H<sub>2</sub>SO<sub>4</sub>. The scans were performed at room temperature, and the scan rate was 50 mV/s.

Table 7-4 The Specific Electrochemical Surface Area (ECA) of catalysts as determined by hydrogen electroadsorption.

Catalysts	$m_{\text{sample}}/\mu\text{g}$	$Q_{\text{H}}^{\text{a}}/\text{mC}$	$\text{SE}^{\text{b}}/\text{cm}^2$	$\text{ECA}^{\text{c}}/\text{m}^2\cdot\text{g}^{-1}$
Commercial Pt/C	4	0.662	3.15	78.8
IL-supported Pt/CNT	0.7	0.140	0.67	95.7

<sup>a</sup>  $Q_{\text{H}}$ : charge exchange during the electroadsorption of hydrogen. <sup>b</sup> SE: real surface area obtained by calculating from  $\text{SE} (\text{cm}^2) = Q_{\text{H}} (\text{mC}) / 0.21 (\text{mC}/\text{cm}^2)$ . <sup>c</sup> ECA: specific electrochemical surface area obtained per gram of catalyst.

## 7.4 Conclusion

Good quality electrocatalysts often depend on their synthesis technique. Highly uniform dispersion of the metal particles is the basic requirement for carbon supported Pt catalysts. Compared to the previous technique for the synthesis of Pt-based carbon nanotube electrocatalysts, novel ionic liquids are likely to contribute to the formation of small Pt particles and suppress the agglomeration and tangling of the as-prepared CNTs. The Pt/CNTs prepared in this work seem to be promising electrocatalysts for direct methanol fuel cells

## **CHAPTER 8. PREPARATION OF POROUS CARBON SUPPORTED Pt NANOCOMPOSITES FOR DIRECT METHANOL FUEL CELLS**

### **8.1 Introduction**

Among the different types of fuel cells, the direct methanol fuel cell (DMFC) is currently at the forefront, because it is directly fed with liquid fuel, which is easy to store and transport. However, low temperature operation requires highly efficient electrocatalysts, which consist of Pt and precious metals supported on high surface area carbons. It is those attractive features of high electrical conductivity, chemical stability, and low cost which make the carbon materials the leading contenders for precious metal catalyst supports [144]. Most researchers have studied a few well characterized forms of carbon black, and recently it has been recognized that different forms of carbon can affect the dispersion of the Pt particles [263]. The development of new carbon supports is one approach towards the production of new electrocatalysts for fuel cells, and these have been developed by many researchers, with the types researched including mesoporous carbon materials [220, 264], carbon nanotubes [187, 265], carbon cryogels [266, 267], and carbon aerogels [268, 269].

Porous carbon materials, in particular, are attracting great attention for their high electrical conductivity, high surface area, and mesoporosity with narrow pore size. Recently, various mesoporous carbon materials have been fabricated using different kinds of mesoporous silica materials as templates [224, 270, 271]. In this work,

mesoporous carbon prepared by removing the mesoporous silica templates is referred to as MC. In addition, carbon aerogels (CAs) have been reported as mesoporous materials with high surface areas and few micropores, which are formed during the pyrolysis of resorcinol-formaldehyde (RF) aerogels [272]. The mesopores of CA are very uniform, although granulated activated carbons have a wide pore size distribution from the micropore to the macropore ranges. Both the MCs and the CAs were applied as platinum catalyst supports for direct methanol fuel cells in this study.

By using the cyclic voltammetry (CV) technique, platinum dispersion and the specific electrochemical surface area of the catalysts were examined and compared. The subsequent tests showed that the Pt/CA catalyst had good methanol oxidation activity, indicating that Pt/CA is suitable as a new alternative type of electrocatalyst for the direct methanol fuel cell.

## **8.2 Synthesis and characterization of porous carbon Pt nanocomposites**

### **(a) Synthesis of the mesoporous carbon (MC)**

The synthesis procedure for mesoporous carbon was described in section 5.2.1.

### **(b) Synthesis of the carbon aerogel (CA)**

The preparation of organic aerogels and their carbonized derivatives was first described by Pekala in 1989 [272]. Briefly, resorcinol (1, 3-dihydroxy benzene) and formaldehyde (RF) were mixed in a 1:2 molar ratio. Deionized or distilled water was used as a diluent

to control the final gel concentration. After a homogeneous precursor formed, sodium carbonate was added as a catalyst. The mixture was then poured into glass vials (10 cm length and 2 cm internal diameter) and kept at around 85 °C for several hours. The cross linked RF gel rods were cut into 5 mm diameter pellets and immersed in acetone for 72 h to remove the water inside the pores. The subsequent drying process with supercritical carbon dioxide (SCCO<sub>2</sub>) ( $T_c = 30\text{ °C}$ ,  $P_c = 7.4\text{ MPa}$ ) is a very important process for generating mesopores in the RF aerogels. The RF hydrogel was placed in a 10<sup>3</sup> cm<sup>3</sup> stainless steel reactor with acetone and dried with SCCO<sub>2</sub>. The liquid CO<sub>2</sub> continuously flowed into the reactor at a rate of 3.0 cm<sup>3</sup>/min under a pressure of 10 MPa; for the first 3 h, the acetone was gradually exchanged for carbon dioxide at 25 °C, and for the following 10 h, the hydrogels were dried at 45 °C. The pressure was then gradually reduced to atmospheric pressure at 45 °C for the last 2 h. Finally, the reactor was cooled to room temperature [273]. Then, the RF aerogels were pyrolyzed in a tube furnace in flowing N<sub>2</sub> (800 cm<sup>3</sup>/min) by heating them up to 1050 °C with a heating rate of 1 °C/min and a soak time of 3 h.

#### (c) Preparation and characterization of Pt/MC and Pt/CA nanocomposites

The Pt/MC and Pt/CA nanocomposites were synthesized by a microwave irradiation method [274]. In a typical procedure, H<sub>2</sub>PtCl<sub>6</sub>·6H<sub>2</sub>O was mixed with ethylene glycol (EG) and KOH, with the different porous carbon particles suspended in the solution. Then they were heated for 20 to 40 seconds in a household microwave at a power of 800 W. The as-prepared products were separated by centrifuge and washed with acetone and de-ionized water. Then they were dried in a vacuum oven at 393 K overnight. The

morphologies of the Pt nanoparticles dispersed on the surface of the mesoporous carbon or carbon aerogel were investigated by scanning electron microscopy (SEM) using a JEOL JSM-6460A instrument, with additional semi-quantitative information obtained using large area standardless EDS analysis. Transmission electron microscopy (TEM) was performed using a JEOL JEM 2011. TEM samples were dispersed on lacey carbon support films. The nitrogen adsorption-desorption isotherms were measured using a Micromeritics ASAP 2010 analyzer. The pore size was calculated by the Barrett-Joyner-Hallenda (BJH) method based on the desorption branch of the nitrogen sorption isotherms.

From the TEM image of Fig. 8-1(a), the as-prepared mesoporous carbon has a unique pore structure with pore diameters around 2-5 nm. The inset selected area electron diffraction (SAED) pattern shows two rings, indicating C(002) and C(101) diffraction. For the Pt/MC catalyst (Fig. 8-1(b)), the Pt nanoparticles were decorated on some defect sites on the MC surface and tended to agglomerate. Moreover, some Pt surface may be buried in the mesopores, since the pore size of MC is of a comparable small size. The Pt particle size in either the Pt/MC catalyst or the Pt/CA catalyst prepared by using the microwave heated polyol process is around 3-6 nm (Fig. 8-1(b) and (d)). Pt nanoparticles were well dispersed on the surface of the as-prepared carbon aerogels (Fig. 8-1(c)). Compared to MC, the shape of the CA surface is quite smooth, and the diameter of the primary carbon particle is large compared to that of the Pt particles.

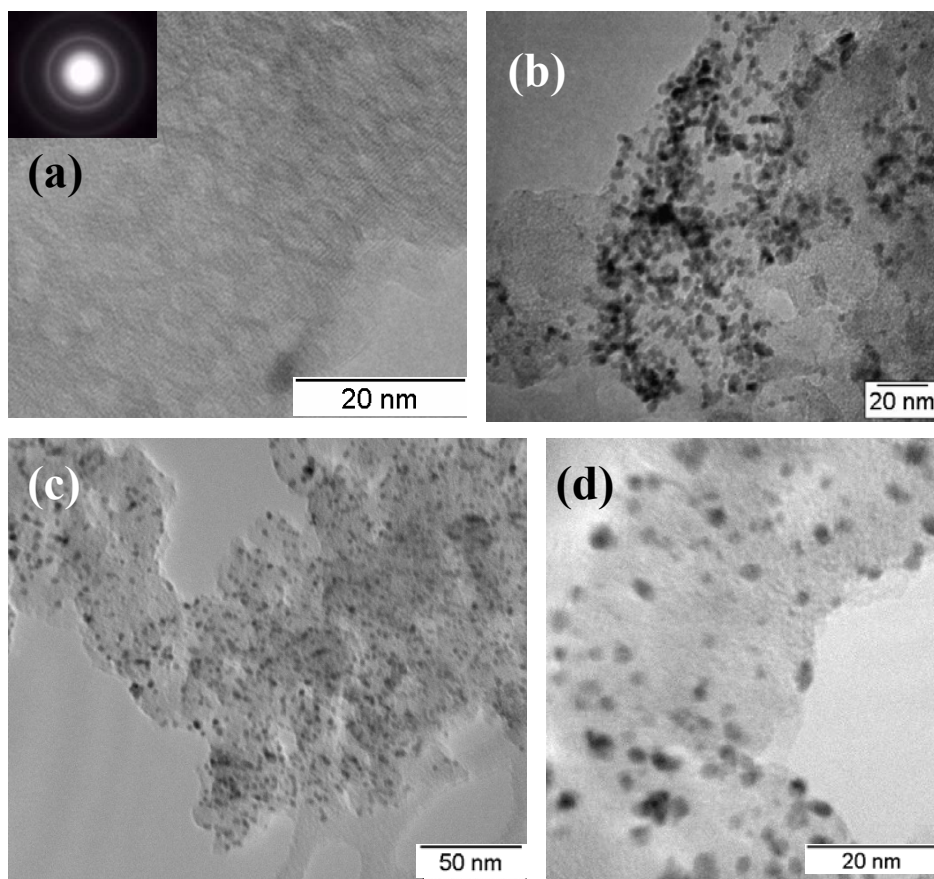


Fig. 8-1 TEM images of (a) MC and corresponding SAED pattern (inset), (b) Pt/MC, and (c), (d) Pt/CA.

Both the Pt/MC and the Pt/CA catalysts show similar morphology from SEM investigation (Fig. 8-2). While carbon aerogels have bigger granulated particles compared to mesoporous carbons, large area standardless EDS analysis indicates that the platinum nanoparticles are about 3.3 wt% of Pt/MC and 2.5 wt% of Pt/CA, respectively.

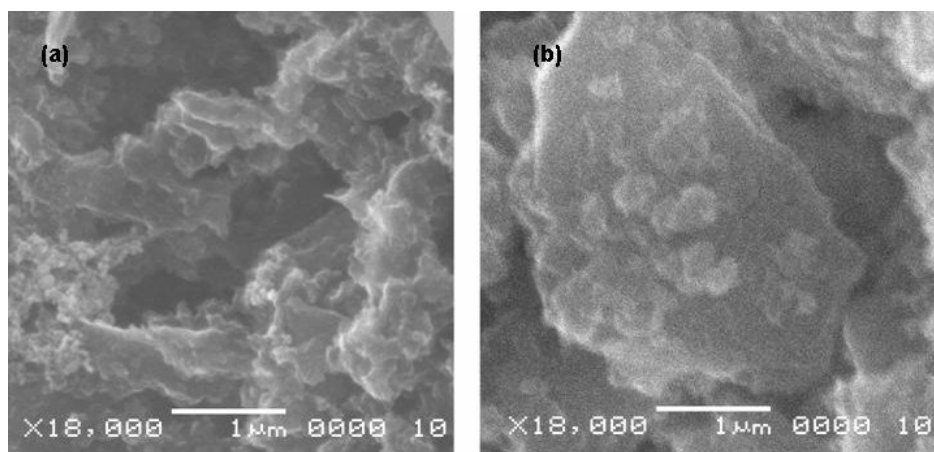


Fig. 8-2 SEM images of Pt/MC (a) and Pt/CA (b).

### 8.3 Electrochemical properties of porous carbon Pt nanocomposites

Fig. 8-3 shows cyclic voltammetry (CV) test results on the Pt/MC and Pt/CA catalysts. Commercial Pt/C (Vulcan XC-72 carbon supported 20% Pt, Johnson Matthew) was also tested for comparison. Determining the platinum electrochemical surface for the Pt/MC and Pt/CA catalysts is one major issue of this work. From Table 8-1, it can be clearly seen that the active surface area of platinum on carbon aerogels is much larger than for mesoporous carbon supported catalysts and is actually 32% higher than for the commercial Pt/C catalyst. The differences in the platinum active areas mean that the accessibility of the electrolyte to the platinum surface atoms for Pt/CA catalyst is much greater than for Pt/MC catalyst. The high electrochemical surface area of the Pt/CA catalyst is owed to better platinum dispersion compared to the Pt/MC catalyst and indicates a higher fraction of Pt atoms on the surface of carbon aerogels with respect to the platinum loading. The platinum active areas measured from cyclic voltammetry correlate with the platinum particle dispersion observed from TEM micrographs. Pt/MC catalyst shows very low Pt active surface areas from CV measurements. One possible reason is that the surfaces of Pt nanoparticles are occluded by being partially buried in the pores of MCs, which are relatively small (2-5 nm), as measured from TEM images (Fig. 8-1(a)). The Pt particle aggregation on the MCs, which is visible in TEM micrographs (Fig. 8-1(b)), is another reason. The platinum nanoparticles dispersed irregularly on the mesoporous carbon surfaces could then be only partially wetted by the liquid electrolyte during the electrochemical reactions. Therefore, only the Pt/CA

catalyst in this study is suitable as a new type of electrocatalyst for direct methanol fuel cells.

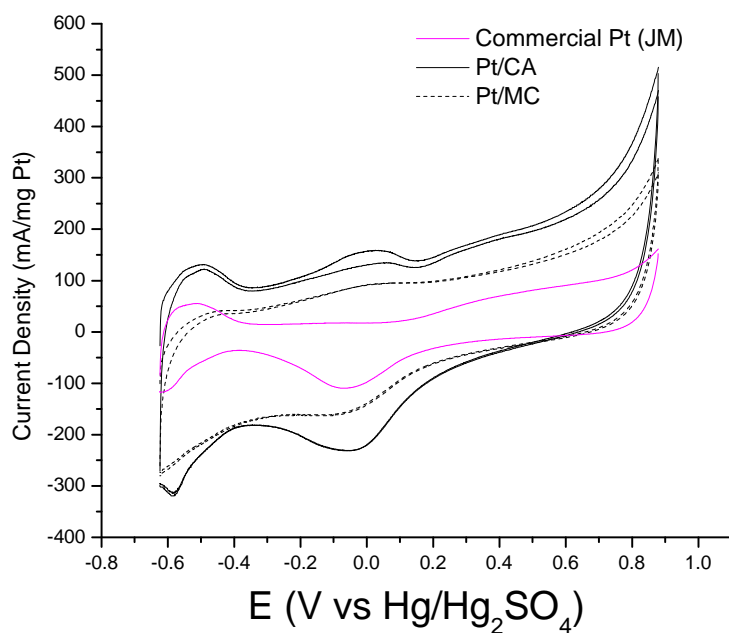


Fig. 8-3 CV curves of the Pt/MC, Pt/CA, and commercial Pt/C in 0.5 M H<sub>2</sub>SO<sub>4</sub>. The scan rate was 50 mV/s at room temperature.

Table 8-1 The specific electrochemical surface area (ECA) of Pt/MC, Pt/CA, and commercial Pt/C catalysts as determined by hydrogen electroadsorption.

	$m_{\text{sample}}/\mu\text{g}$	$Q_{\text{H}}/\text{mC}$	$\text{SE}/\text{cm}^2$	$\text{ECA}/\text{m}^2\text{g}^{-1}$
Commercial Pt/C	4	0.673	3.205	80.12
Pt/MC	0.33	0.00764	0.0364	11.03
Pt/CA	1	0.223	1.062	106.2

To further evaluate the reasons why Pt/CA catalyst can exhibit high electrochemical activity, nitrogen adsorption-desorption studies were implemented. Fig. 8-4 shows the N<sub>2</sub> sorption isotherms of the as-prepared carbon aerogels, with the inset revealing that

the pore size distribution is centered at around 8 nm. The BJH desorption pore size distribution consistently reveals a relatively narrow pore size range. The carbon aerogels have a unique particle size and limited pore range, plus they have a relatively large primary carbon particle size and smooth surface. All of these can contribute to their functioning as good catalyst supports. Both adsorption and desorption isotherms show significant nitrogen uptake at relative pressures above 0.7, which can be attributed to the mesopores of the CAs. The pore structure in the Pt/CA catalyst may enhance the specific activity, since the mesopore network can facilitate the transport of methanol and the reaction products, such as CO<sub>2</sub> [275].

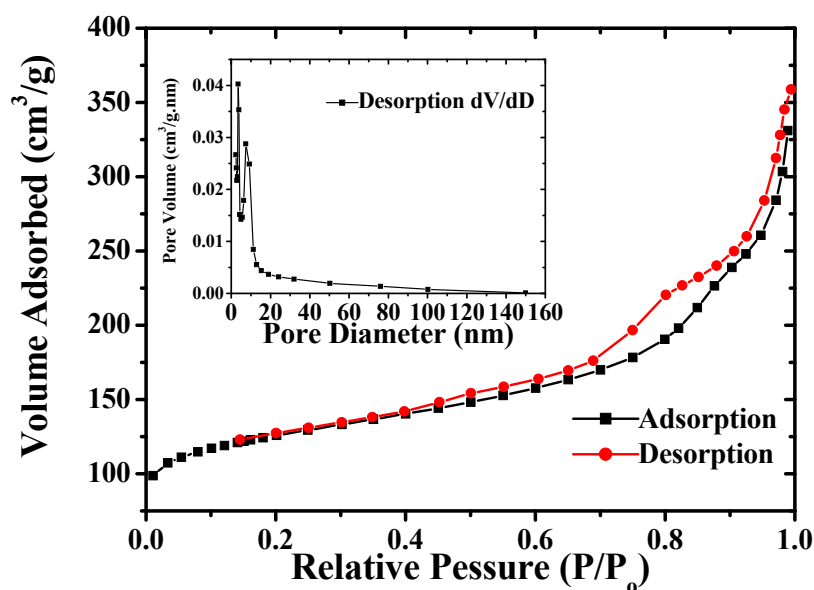


Fig. 8-4 N<sub>2</sub> sorption isotherms of the carbon aerogel and corresponding BJH pore size distribution (inset) derived from the desorption branch of the carbon aerogel.

The methanol oxidation current density for the Pt/CA catalyst was evaluated by cyclic voltammetry measurements. Fig. 8-5 shows the CV curve of the Pt/CA catalyst in a 0.5 M H<sub>2</sub>SO<sub>4</sub> solution with 1 M CH<sub>3</sub>OH in the potential range from -0.2 V to 1.0 V at a scan

rate of 50 mV/s. The features are consistent with the data in most of the literature [187, 274-276]. The methanol oxidation current was normalized to the amount of Pt loading on the CAs. During the first forward scan, the onset potential of methanol oxidation for Pt/CA catalyst was 0.46 V. The current density increased dramatically, and the peak potential was observed at 0.67 V, which can be attributed to methanol electro-oxidation on the Pt/CA catalyst. The specific peak current density was 500 mA/mg in the first cycle and 477 mA/mg in the second. During the reverse scan, the peak current density was 355 mA/mg at 0.45 V, which is associated with the reactivation of oxidized Pt. All of the above results indicate that Pt/CA is suitable as a new type of electrocatalyst for direct methanol fuel cells.

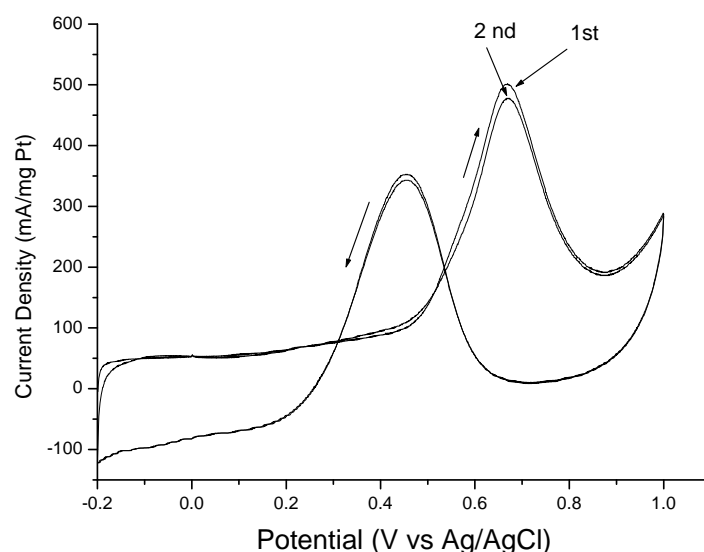


Fig. 8-5 Cyclic voltammetry of Pt/CA electrode in 1 M CH<sub>3</sub>OH/ 0.5 M H<sub>2</sub>SO<sub>4</sub> solution at room temperature, at a scan rate of 50 mV/s.

## 8.4 Conclusion

Two different types of porous carbon materials were prepared and studied as electrocatalyst supports for direct methanol fuel cells in this study. By using the silica

template method, mesoporous carbon (MC) materials were applied as Pt electrocatalyst supports, but due to the Pt nanoparticle aggregation and low electrochemical surface areas, The Pt/MC catalyst in this study was found to be unsuitable for use as an electrocatalyst in direct methanol fuel cells. At the same time, carbon aerogel (CA) materials synthesized by using the organic aerogel carbonization method demonstrated good electrocatalytic properties towards methanol oxidation. The Pt/CA catalyst has a higher specific electrochemical surface area compared to the commercial Pt/C catalyst, which indicated that it is suitable as an alternative electrocatalyst for direct methanol fuel cells.

## **CHAPTER 9. METHANOL TOLERANT Pt/FeO<sub>x</sub>/C NANOCOMPOSITE CATHODES FOR DIRECT METHANOL FUEL CELLS**

### **9.1 Introduction**

Pt based electrocatalysts have been widely used as oxygen reduction cathode materials for direct methanol fuel cells (DMFCs). However, due to the methanol permeation from anode to cathode through the membrane, methanol can be electro-oxidized to CO, which can poison the cathode under some conditions, so it is crucial to find a methanol tolerant cathode electrocatalyst for the oxygen reduction reaction (ORR). Platinum based metal alloys have been studied as oxygen reduction electrocatalysts in direct methanol fuel cells. Pt/M (M is Cr, Co, Ni, Fe, etc.) exhibited better electrocatalytic activity for ORR than pure Pt [277-281]. Additionally, Pt/MO<sub>x</sub> (M is Ti, W) has also been investigated for ORR and shown higher methanol tolerant performance [146, 282, 283].

Since electro-oxidized CO from methanol blocks the Pt surface on the electrocatalysts, further promotion of CO electro-oxidation to CO<sub>2</sub> is required for both cathode and anode electrocatalysts in DMFCs. The alloying of other metal components with Pt has been a favored method, and the most active catalytic system for CO tolerant anodes is Pt/Ru alloy. It has been suggested that the promotion of CO electro-oxidation through the activation of water by the ruthenium component in the surface (to provide the oxidant in a bifunctional mechanism) and an electronic effect of Ru on Pt ensuring lower mean coverage of CO are two possible mechanisms [284-286]. Pt-Fe/mordenite catalysts

exhibited remarkable preferential oxidation of CO [287]. CO adsorbed on a Pt site can react with O preserved on a Fe site through the surface diffusion of both of the reactants via a bifunctional mechanism [288]. Pt/Fe alloys were prepared as electrocatalysts for direct methanol fuel cells by using an impregnation method or modified polyol process [289, 290]. In this work, we successfully designed and prepared a Pt/FeO<sub>x</sub>/C nanocomposite system by a two step chemical reduction process. In this system, Pt sites and Fe sites are close enough for the CO electro-oxidation reaction to take place via the bifunctional mechanism by which CO tolerance is afforded. This study suggests that for the Pt based electrocatalysts, metal oxides like iron oxides can provide more active sites compared to pure Pt to absorb oxygen species to avoid CO poisoning.

## 9.2 Synthesis and characterization of Pt/FeO<sub>x</sub>/C nanocomposites

The Pt/FeO<sub>x</sub>/C nanocomposites were prepared by a two step reduction process. In a typical procedure, 0.45 g carbon black (Vulcan XC-72) in 100 ml de-ionized water was heated to 75 °C and kept at that temperature under reflux for 30 min with constant stirring, after which a solution of FeCl<sub>2</sub>·4H<sub>2</sub>O (0.18 g in 25 ml of de-ionized water) was added. The obtained mixture was vigorously stirred for 30 min at 75-80 °C, followed by the addition of a reducing agent, consisting of NaBH<sub>4</sub> (0.523 g) and NaOH (37 mg) dissolved in 50 ml de-ionized water, at a rate of 2 ml/min using a peristaltic pump until the pH reached 11. Then the reaction conditions were kept constant for 30 min, completing the reduction process. The as-prepared FeO<sub>x</sub>/C nanocomposite was centrifuged, washed with de-ionized water until the pH reached 7, and then dried overnight at 90 °C under vacuum. 0.1 g of the as-prepared FeO<sub>x</sub>/C nanocomposite was

added to 25 ml of 0.002 M H<sub>2</sub>PtCl<sub>6</sub> aqueous solution. The reduction process followed the same procedure outlined above. When the reduction reaction was completed, the Pt/FeO<sub>x</sub>/C was centrifuged, washed thoroughly with de-ionized water and ethanol, and then dried overnight at 90 °C under vacuum.

The morphologies and distributions of Pt and iron oxides on the surfaces of the active carbon (Vulcan XC72) are shown in the TEM bright field and dark field images of Fig. 9-1(a) and (b). It can be seen that small Pt nanoparticles were decorated on the spherical active carbon surface, while iron oxide particles were relatively larger. To further identify the components of the as-prepared samples, the selected area electron diffraction (SAED) pattern and EDS spectrum are presented in Fig. 9-1(c) and (d). The spotty rings of the Pt (111) and the FeO<sub>x</sub> (311), (220), (211), and (111) reflections in the SAED pattern are evidence for the presence of Pt/FeO<sub>x</sub> nanocomposite, in agreement with the XRD data shown in Fig. 9-2. The crystalline phase of the iron oxide can not be distinguished unambiguously between maghemite  $\gamma$ -Fe<sub>2</sub>O<sub>3</sub> (39-1346) and magnetite Fe<sub>3</sub>O<sub>4</sub> (19-0629), because of similar *d* spacings for these two iron oxides [291]. The EDS spectrum also shows trace amounts of Pt and Fe in Fig. 9-1(d), and large area standardless EDS analysis indicates that the Pt:FeO<sub>x</sub>:C weight ratio is around 6:14:80.

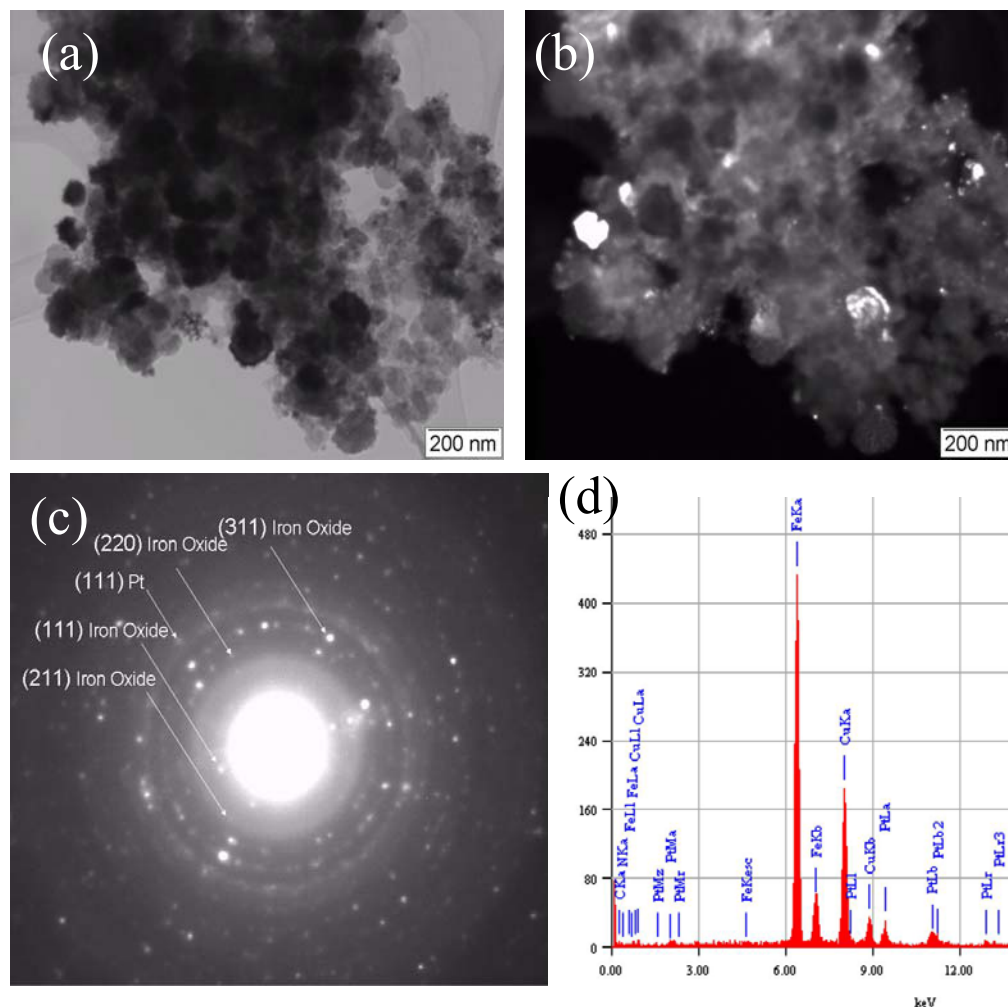


Fig. 9-1 TEM bright and dark field images of as-prepared Pt/ FeO<sub>x</sub>/C nanocomposite (a) and (b).

SAED patterns (c) and EDS spectrum (d) of Pt/FeO<sub>x</sub>/C nanocomposite.

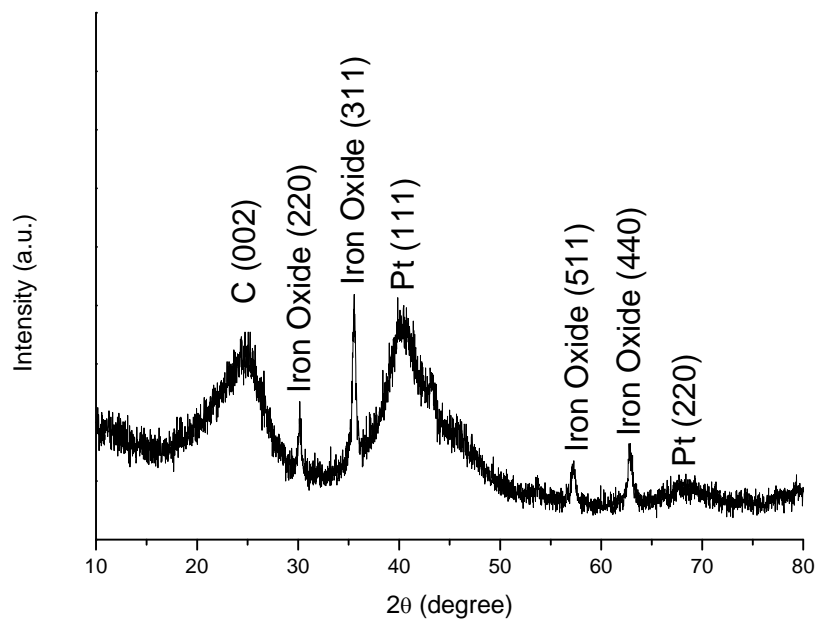


Fig. 9-2 XRD pattern of Pt/ FeO<sub>x</sub>/C nanocomposite.

The chemically disordered nature of Pt nanoparticles is confirmed with the identification of fcc Pt (111) and (200) planes in the HRTEM image shown in Fig. 9-3(a). Pt nanoparticles are randomly oriented on the active carbon surface, but have good crystallinity, since the HRTEM image shows uniform lattice fringes across the particles. Normally, in platinum alloy catalysts, the crystal structure and the lattice parameter of platinum are changed by alloying with transition metals at high temperature [292], while in this study the lattice parameters of platinum were unchanged. Pt nanoparticles were located at neighboring sites to FeO<sub>x</sub> (inset image of Fig. 9-3(a)). To further identify the phase in the nanocomposite, a dark field TEM image of Pt nanoparticles was obtained by using Pt (111) reflections of the spotty ring in the selected area electron diffraction (SAED) pattern (inset image of Fig. 9-3 (b)). Similarly, FeO<sub>x</sub> nanoparticles were identified by using the FeO<sub>x</sub> (311) reflection in the SAED pattern (inset in Fig. 9-3(c)). Since the permeation of methanol from the anode to the cathode causes poisoning of Pt and the methanol oxidation process in direct methanol fuel cells (DMFC) involves a Pt-(CO)<sub>ads</sub> intermediate [293], the promotion of CO electro-oxidation on Pt surfaces can improve the electrocatalytic activities of the cathode catalyst in DMFCs. According to mechanism studies of the preferential oxidation of CO [287] in the Pt/FeO<sub>x</sub>/C system, CO adsorbed on Pt sites can react with O preserved on Fe sites once they are close enough for surface diffusion. As we can see from Fig. 9-3, Pt and FeO<sub>x</sub> nanoparticles are located at ‘neighbor sites’, which are close enough to react to release fresh Pt sites. So Pt/FeO<sub>x</sub>/C cathode can continuously act as an oxygen reduction electrocatalyst, self-avoiding CO poisoning of Pt. Thus, Pt/FeO<sub>x</sub>/C nanocomposites are promising methanol tolerant cathodes for the oxygen reduction reaction.

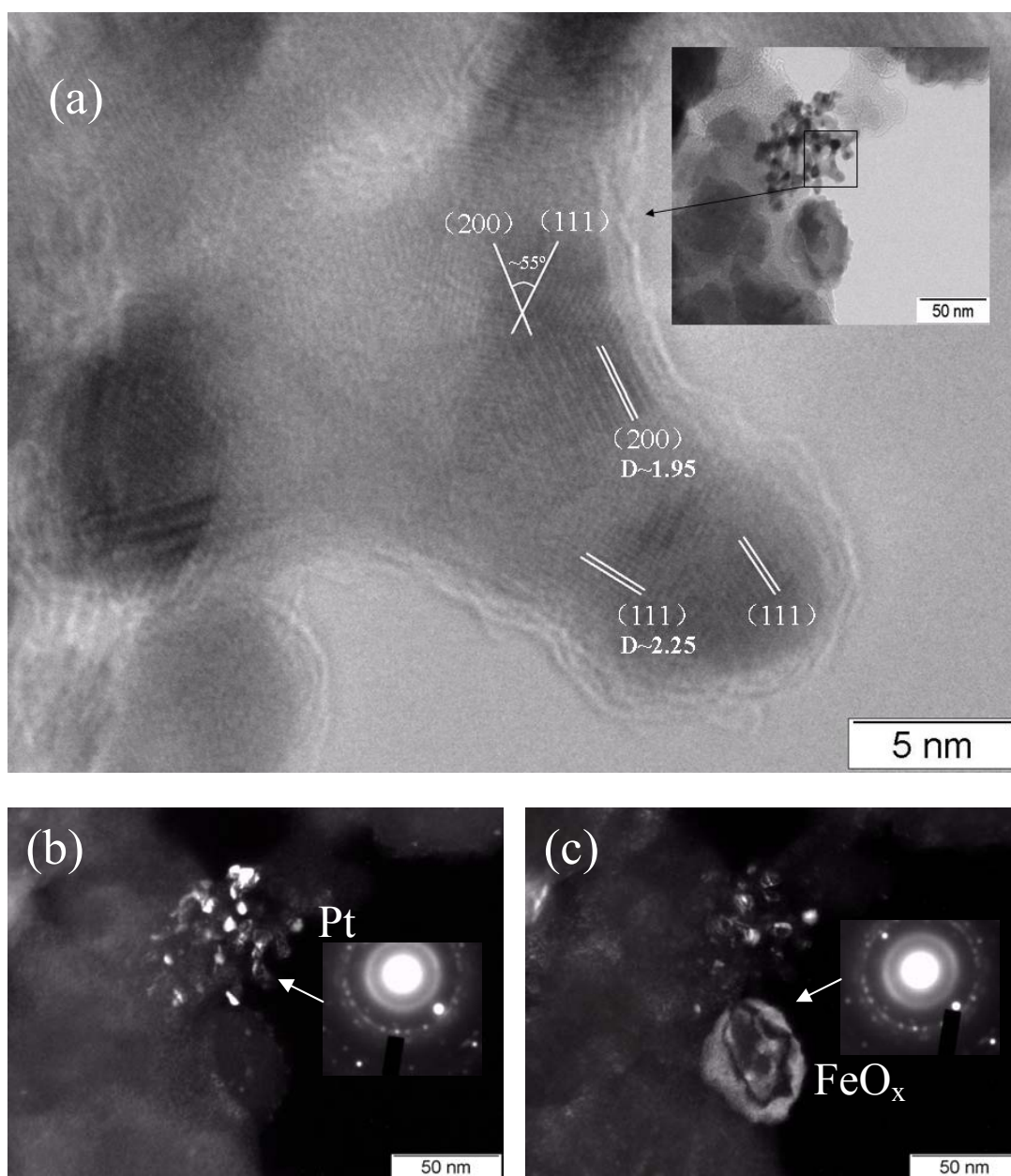


Fig. 9-3 (a) HRTEM image of as-prepared Pt/FeO<sub>x</sub>/C nanocomposite suggests that Pt particles are randomly oriented. The inset shows a bright field TEM image corresponding to (c) and (d).. (b) The dark field image was obtained by using Pt (111) reflections of the indicated spotty ring in the SAED pattern (inset image). (c) Dark field image with FeO<sub>x</sub> (311) reflections in the SAED pattern (inset image).

### 9.3 Electrochemical properties of Pt/FeO<sub>x</sub>/C nanocomposites

Fig. 9-4 compares the open circuit potential losses caused by methanol poisoning for Pt/FeO<sub>x</sub>/C electrocatalyst. The open potential losses are high because the effect of methanol poisoning is significant in the activation of the overpotential region related to oxygen reduction kinetics [282]. The potential loss increases with increasing methanol concentration. Nevertheless, the potential loss for the Pt/FeO<sub>x</sub>/C catalyst is smaller compared to commercial Pt/C catalysts, especially at higher methanol concentrations. Thus, FeO<sub>x</sub> suppresses methanol poisoning in the catalyst to some extent, and the Pt/FeO<sub>x</sub>/C nanocomposite shows improved tolerance of the cathode to methanol.

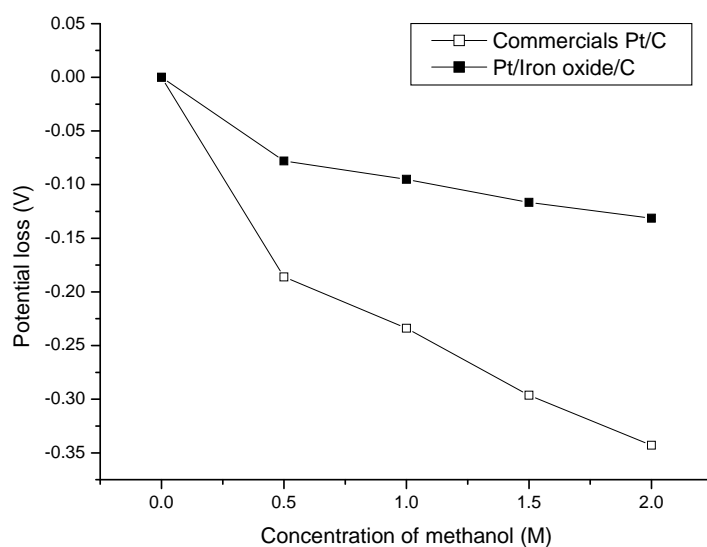


Fig. 9-4 Relationship between the open circuit voltage (OCV) loss due to the methanol poisoning of the Pt/FeO<sub>x</sub>/C nanocomposite and the concentration of methanol in 0.5 M H<sub>2</sub>SO<sub>4</sub> electrolyte.

Hydrodynamic voltammetry is one of the most common techniques in electrochemical studies to estimate the number of electrons consumed during the course of the O<sub>2</sub> reduction reactions [294]. Fig. 9-5 shows the linear sweep voltammetry results for

oxygen reduction in the as-prepared samples in O<sub>2</sub>-saturated 0.5 M H<sub>2</sub>SO<sub>4</sub>. There is no well-defined limiting current plateau for the oxygen reduction on the Pt/FeO<sub>x</sub>/C electrocatalysts. The absence of a well-defined limiting current can be due to the combined kinetic-diffusion control of the reaction or the dependence on the potential of the number of electrons consumed per O<sub>2</sub> molecule [295]. The Koutecky-Levich (K-L) equation [296] was used to analyze the data of Fig. 9-6.

$$\frac{1}{I} = \frac{1}{I_k} + \frac{1}{I_d} = -\frac{1}{nFAkC_{O_2}^0} - \frac{1}{0.62nFAD_{O_2}^{2/3}\nu^{-1/6}C_{O_2}^0\omega^{1/2}} \quad (9-1)$$

where  $I$  is the measured current,  $I_k$  and  $I_d$  are the kinetic and diffusion-limited currents, respectively,  $k$  is the rate constant for O<sub>2</sub> reduction,  $F$  is the Faraday constant (96484 C mol<sup>-1</sup>),  $A$  is the electrode area (cm<sup>2</sup>),  $\omega$  is the rotation rate (rad s<sup>-1</sup>),  $C_{O_2}^0$  is the concentration of oxygen in 0.5 M H<sub>2</sub>SO<sub>4</sub> ( $1.13 \times 10^{-6}$  mol cm<sup>-3</sup>),  $D_{O_2}$  is the diffusion coefficient of O<sub>2</sub> ( $1.93 \times 10^{-5}$  cm<sup>2</sup> s<sup>-1</sup>), and  $\nu$  is the kinematic viscosity of the solution (0.0095 cm<sup>2</sup> s<sup>-1</sup>).

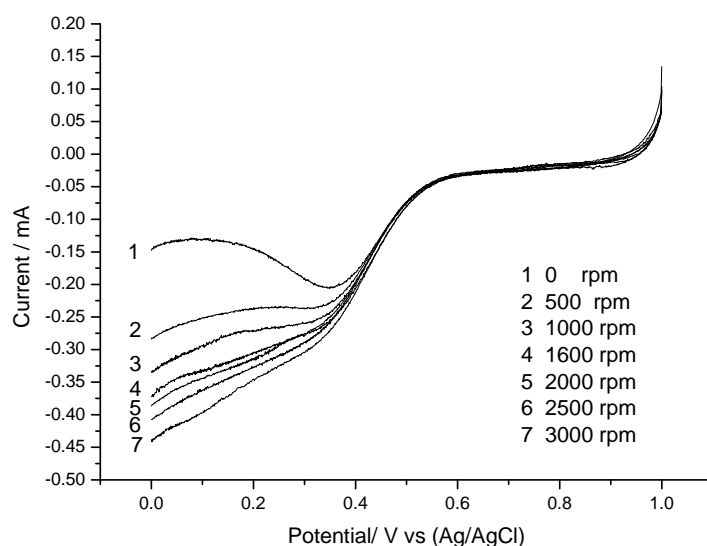


Fig. 9-5 Oxygen reduction on a 4 mm diameter glassy carbon electrode in O<sub>2</sub>-saturated 0.5 M H<sub>2</sub>SO<sub>4</sub> at a scan rate of 20 mV/s. The rotation rate was from 0 rpm to 3000 rpm.

Fig. 9-6 shows typical K-L plots for the O<sub>2</sub> reduction at the Pt/FeO<sub>x</sub>/C nanocomposite. The potential dependence of  $n$  on the applied potential for oxygen reduction was calculated from these results using equation (9-1). The results are shown in Table 9-1. It was found the oxygen reduction by Pt/FeO<sub>x</sub>/C electrocatalyst follows a direct reduction path, in which O<sub>2</sub> is reduced directly to H<sub>2</sub>O through a four electron transfer process.

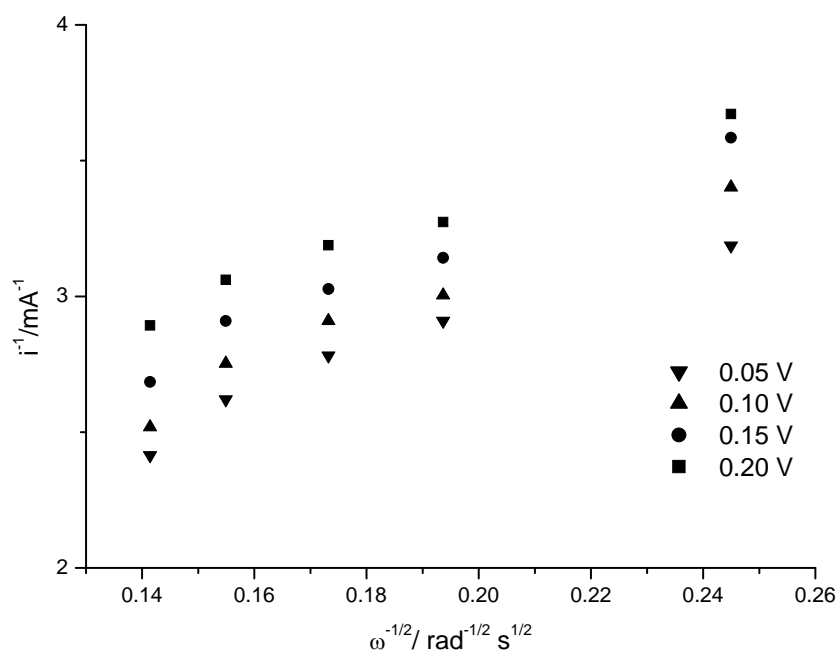


Fig. 9-6 K-L plots for oxygen reduction on a glassy carbon electrode in 0.5 M H<sub>2</sub>SO<sub>4</sub> at various potentials.

Table 9-1 The number of electrons exchanged per molecule of O<sub>2</sub> for the applied potential.

	E/V vs. (Ag/AgCl)	1/ I <sub>k</sub> (mA <sup>-1</sup> )	n
1	0.05	-1.500	4.24
2	0.10	-1.471	3.92
3	0.15	-1.586	3.67
4	0.20	-1.918	4.19

## 9.4 Conclusion

In summary, a methanol tolerant Pt/FeO<sub>x</sub>/C cathode for direct methanol fuel cells was prepared by a two step chemical reduction process. The as-prepared nanocomposite shows an improved methanol tolerance compared to the commercial Pt/C cathode. Pt nanoparticles are randomly oriented on the active carbon surface, and FeO<sub>x</sub> nanoparticles with relatively bigger particle sizes are located at neighboring sites to the Pt. CO intermediates that tend to poison Pt can react with O species absorbed on Fe sites to release Pt sites. Therefore, Pt/FeO<sub>x</sub>/C nanocomposite is a new alternative methanol tolerant cathode for oxygen reduction reactions in direct methanol fuel cells.

## **CHAPTER 10. GENERAL CONCLUSIONS**

### **10.1 Review of this study**

Investigations on novel nanocomposite prepared by various liquid-phase synthesis methods for lithium ion battery anodes or for direct methanol fuel cell electrocatalysts have been presented in the previous chapters. There are mainly two groups of inorganic nanocomposites, which are tin based nanocomposites for lithium ion battery anodes and platinum based nanocomposites for direct methanol fuel cells:

#### **10.1.1 Tin based nanocomposites for lithium ion battery anodes**

For lithium ion battery anodes, many efforts have been aimed at finding potential substitutes for carbon based materials. Tin based materials have been a popular candidate material for lithium ion battery anodes ever since it was discovered. In this study, different kinds of tin based nanocomposites were prepared by liquid-phase chemical reduction methods, and their electrochemical properties for lithium ion batteries were examined in detail.

Nanocrystalline multi-wall carbon nanotube (MWNT)-Sn and MWNT-SnNi composite anode materials were prepared by chemical reduction of  $\text{SnCl}_2$  and  $\text{NiCl}_2$  precursors in the presence of MWNTs. Microscope observations showed that the Sn and SnNi particles are homogeneously dispersed on the surface of the MWNTs and in the MWNT

matrix. The electrochemical performance of MWNT-Sn and MWNT-SnNi nanocomposites has been investigated by charge/discharge tests, cyclic voltammetric experiments, and the ac impedance technique. The MWNT-Sn and MWNT-SnNi anodes demonstrated a high first discharge capacity (570 and 512 mAh g<sup>-1</sup> for MWNT-Sn and MWNT-SnNi anodes, respectively), high charge/discharge efficiency in the first cycle (77.5% and 84.1% for MWNT-Sn and MWNT-SnNi anodes, respectively), and good cyclability (0.99 loss%/cycle for MWNT/SnNi anode). A reaction model has been proposed to explain the reaction mechanisms of lithium insertion and extraction in the MWNT-Sn and MWNT-SnNi electrodes.

A new mesoporous carbon-tin (MC-Sn) nanocomposite has been successfully prepared via a two-step co-precipitation method. From the transmission electron microscopy (TEM) observations, the tin nanoparticles were decorated on the as-prepared mesoporous carbons. The mesoporous structure of the carbon can effectively buffer the volume changes during the Li-Sn alloying and de-alloying cycles. The as-prepared MC-Sn nanocomposite electrodes exhibited extremely good cycling stability, with the specific capacity of Sn in the composite electrode calculated to be 959.7 mAh g<sup>-1</sup>, which amounts to an impressive 96.9% of the theoretical value (990 mAh g<sup>-1</sup>). The reversible capacity after 200 cycles is 96.1% of the first cycle reversible capacity, i.e. the capacity fade rate is only 0.0195% per cycle, which is even better than that of commercial graphite-based anodes.

A new type of nanostructured titania nanotube supported tin anode was prepared for lithium ion batteries. The as-prepared titania nanotubes were in the anatase phase with diameters of about 12 nm. Tin nanoparticles were dramatically decorated on the titania nanotubes and had a particle size of about 10 nm. This new structure promises good retention of reversible capacity on cycling for lithium intercalation. By charge/discharge measurements, the reversible capacity of the titania nanotube supported tin anode for lithiation and de-lithiation was found to be 312 mAh g<sup>-1</sup> (cycled between 0.05 and 2.0 V) and 203 mAh g<sup>-1</sup> (cycled between 0.05 and 1.3 V) after 50 cycles with around 100% columbic efficiency.

### **10.1.2 Pt based nanocomposites for DMFC electrocatalysts**

For electrocatalysts of direct methanol fuel cells (DMFCs), active carbon supported platinum catalysts are commonly used nowadays. Different carbon supports or secondary metal components were attempted to synthesize Pt based nanocomposites by using liquid-phase synthesis methods to achieve better electrocatalytic performance for DMFC in this study.

Novel ionic liquids (ILs) were used to prepare carbon nanotube (CNT) supported platinum catalysts by using the microwave assisted polyol process for direct methanol fuel cells. The CNTs were pretreated in acid to obtain functional groups to promote the adherence of Pt nanoparticles. Ionic liquids added to the reaction system appeared to have contributed to the formation of homogeneous small Pt particles and to the

suppression of the agglomeration of CNTs. The Pt/CNT electrocatalyst for direct methanol fuel cells was studied by cyclic voltammetry measurements. The results show that the ionic liquid had a significant impact on the surface of the as-prepared CNTs and that there is a strong interaction between ionic liquids and CNTs.

Two different types of Pt nanocomposites with porous carbon support were prepared for direct methanol fuel cell anode catalysts. By using the microwave assisted polyol process, Pt nanoparticles were decorated on as-prepared mesoporous carbon (MC) and carbon aerogel (CA). The Pt/CA nanoparticles had a quite homogeneous dispersion of Pt nanoparticles, while Pt particles on mesoporous carbon tend to agglomerate on some defect sites. The specific electrochemical surface areas of the Pt/CA and Pt/MC nanocomposites were studied by cyclic voltammetry measurements. The results showed that Pt/CA nanocomposites had good electrocatalytic performance towards the methanol oxidation reaction for direct methanol fuel cells.

A Pt/FeO<sub>x</sub>/C nanocomposite was synthesized by a two step impregnation method by using sodium borohydride as the reducing reagent. Morphologies and identifications of the as-prepared platinum and iron oxides in the nanocomposites were investigated by transmission electron microscopy (TEM) and X-ray diffraction analysis. The mechanism by which iron oxides in the nanocomposite promote methanol tolerance was discussed in detail. Methanol tolerant performance as an oxygen reduction electrocatalyst was studied for the as-prepared Pt/FeO<sub>x</sub>/C nanocomposite.

## **10.2 Suggestions for future study**

For lithium ion battery anodes, although a series of studies on the physical, structural and electrochemical properties of tin based nanocomposite anode materials have been carried out in the present studies, the specific capacity is not as high as expected, due to the low loading amount of tin in the nanocomposites. Thus, further work should be addressed to increasing the loading amounts of tin particles. It should also be noted that the characterisation of the electrode performance has focused on the specific capacity, cycle life, and rate capability. Other performance parameters of the electrode, such as high temperature behaviour and thermodynamic properties, have not been considered. It is therefore suggested that efforts should be made on the parameters mentioned above in order to further understand and improve the performance of the electrodes.

For direct methanol fuel cells, although the electrochemical activities of the as-prepared Pt nanocomposite are promising, single cell tests with a methanol liquid feed are still very much needed for further research. Moreover, due to the high cost of Pt, the replacement of Pt based electrocatalysts with lower cost materials would be highly desirable. It would be more advisable to seek alternative cathode catalysts, considering the much larger electrochemical losses on Pt at the cathode than at the anode, where the difficult oxygen reduction reaction (ORR) requires higher Pt loading. A possible solution is the development of Fe or Co based electrocatalysts for ORR, especially the catalysts prepared with low cost metals and nitrogen precursors.

## REFERENCES

1. Cushing, B.L., Kolesnichenko, V.L., O'Connor, C.J., (2004) Chem. Rev., vol. 104, pp. 3893
2. Roucoux, A., Schulz, J., Patin, H., (2002) Chem. Rev., vol. 102, pp. 3757
3. Boutonnet, M., Kizling, J., Stenius, P., Maire, G., (1982) Colloids and Surfaces, vol. 5, pp. 209
4. Tan, Y., Dai, X., Li, Y., Zhu, D., (2003) Journal of Materials Chemistry, vol. 13, pp. 1069
5. Yonezawa, T., Sutoh, M., Kunitake, T., (1997) Chemistry Letters, vol. 26, pp. 619
6. Yonezawa, T., Onoue, S., Kimizuka, N., (2000) Langmuir, vol. 16, pp. 5218
7. Chow, G.M., Ambrose, T., Xiao, J.Q., Twigg, M.E., Baral, S., Ervin, A.M., Qadri, S.B., Feng, C.R., (1992) Nanostructured Materials, vol. 1, pp. 361
8. van Wonterghem, J., Morup, S., Koch, C.J.W., Charles, S.W., Wells, S., (1986) Nature, vol. 322, pp. 622
9. Harris, V.G., Kaatz, F.H., Browning, V., Gillespie, D.J., Everett, R.K., Ervin, A.M., Elam, W.T., Edelstein, A.S., (1994) Journal of Applied Physics, vol. 75, pp. 6610
10. Brust, M., Walker, M., Bethell, D., Schiffrin, D.J., Whyman, R., (1994) Chemical Communications, vol. 7, pp. 801
11. Weisbecker, C.S., Merritt, M.V., Whitesides, G.M., (1996) Langmuir, vol. 12, pp. 3763
12. Porter, L.A., Ji, D., Westcott, S.L., Graupe, M., Czernuszewicz, R.S., Halas, N.J., Lee, T.R., (1998) Langmuir, vol. 14, pp. 7378
13. Yonezawa, T., Kunitake, T., (1999) Colloids and Surfaces A: Physicochemical and Engineering Aspects, vol. 149, pp. 193
14. Green, M., O'Brien, P., (2000) Chemical Communications, vol. 3, pp. 183
15. Xu, W., Liu, W., Zhang, D., Xu, Y., Wang, T., Zhu, D., (2002) Colloids and Surfaces A: Physicochemical and Engineering Aspects, vol. 204, pp. 201
16. Corbierre, M.K., Cameron, N.S., Sutton, M., Mochrie, S.G.J., Lurio, L.B., Ruhm, A., Lennox, R.B., (2001) J. Am. Chem. Soc., vol. 123, pp. 10411
17. Prasad, B.L.V., Stoeva, S.I., Sorensen, C.M., Klabunde, K.J., (2003) Chem. Mater., vol. 15,

## References

- pp. 935
18. Brown, L.O., Hutchison, J.E., (1997) *J. Am. Chem. Soc.*, vol. 119, pp. 12384
  19. Ingram, R.S., Hostetler, M.J., Murray, R.W., (1997) *J. Am. Chem. Soc.*, vol. 119, pp. 9175
  20. Hostetler, M.J., Green, S.J., Stokes, J.J., Murray, R.W., (1996) *J. Am. Chem. Soc.*, vol. 118, pp. 4212
  21. Nuss, S., Bottcher, H., Wurm, H., Hallensleben, M.L., (2001) *Angewandte Chemie International Edition*, vol. 40, pp. 4016
  22. Tour, J.M., Jones, L., Pearson, D.L., Lamba, J.J.S., Burgin, T.P., Whitesides, G.M., Allara, D.L., Parikh, A.N., Atre, S., (1995) *J. Am. Chem. Soc.*, vol. 117, pp. 9529
  23. Andres, R.P., Bielefeld, J.D., Henderson, J.I., Janes, D.B., Kolagunta, V.R., Kubiak, C.P., Mahoney, W.J., Osifchin, R.G., (1996) *Science*, vol. 273, pp. 1690
  24. Stoeva, S., Klabunde, K.J., Sorensen, C.M., Dragieva, I., (2002) *J. Am. Chem. Soc.*, vol. 124, pp. 2305
  25. Chen, S., Kimura, K., (1999) *Langmuir*, vol. 15, pp. 1075
  26. Han, M.Y., Quek, C.H., Huang, W., Chew, C.H., Gan, L.M., (1999) *Chem. Mater.*, vol. 11, pp. 1144
  27. Reetz, M.T., Helbig, W., (1994) *J. Am. Chem. Soc.*, vol. 116, pp. 7401
  28. Rodriguez-Sanchez, L., Blanco, M.C., Lopez-Quintela, M.A., (2000) *J. Phys. Chem. B*, vol. 104, pp. 9683
  29. Mohamed, M.B., Wang, Z.L., El-Sayed, M.A., (1999) *J. Phys. Chem. A*, vol. 103, pp. 10255
  30. Asenjo, J., Amigo, R., Krotenko, E., Torres, F., Tejada, J., Brillas, E., Sardin, G., (2001) *Journal of Nanoscience and Nanotechnology*, vol. 1, pp. 441
  31. Huang, H.H., Ni, X.P., Loy, G.L., Chew, C.H., Tan, K.L., Loh, F.C., Deng, J.F., Xu, G.Q., (1996) *Langmuir*, vol. 12, pp. 909
  32. Adriana, S.A., Jose, D.A., Waldemar, A.A.M., Maria, C.M.A., (2000) *Journal of Applied Physics*, vol. 87, pp. 4352
  33. Gu, Y., Li, G., Meng, G., Peng, D., (2000) *Materials Research Bulletin*, vol. 35, pp. 297
  34. Li, J.-G., Ikegami, T., Wang, Y., Mori, T., (2002) *Journal of the American Ceramic Society*,

## References

- vol. 85, pp. 2376
35. Xiang, L., Deng, X.Y., Jin, Y., (2002) *Scripta Materialia*, vol. 47, pp. 219
36. Du, Y., Fang, J., Zhang, M., Hong, J., Yin, Z., Zhang, Q., (2002) *Materials Letters*, vol. 57, pp. 802
37. Borse, P.H., Kankate, L.S., Dassenoy, F., Vogel, W., Urban, J., Kulkarni, S.K., (2002) *Journal of Materials Science: Materials in Electronics*, vol. 13, pp. 553
38. Kuo, P.C., Tsai, T.S., (1989) *Journal of Applied Physics*, vol. 65, pp. 4349
39. Tang, Z.X., Sorensen, C.M., Klabunde, K.J., Hadjipanayis, G.C., (1991) *Journal of Colloid and Interface Science*, vol. 146, pp. 38
40. Rojas, T.C., Ocana, M., (2002) *Scripta Materialia*, vol. 46, pp. 655
41. Chinnasamy, C.N., Jeyadevan, B., Perales-Perez, O., Shinoda, K., Tohji, K., Kasuya, A., (2002) *Magnetics, IEEE Transactions on*, vol. 38, pp. 2640
42. Li, J., Dai, D., Zhao, B., Lin, Y., Liu, C., (2002) *Journal of Nanoparticle Research*, vol. 4, pp. 261
43. Wu, K.T., Kuo, P.C., Yao, Y.D., Tsai, E.H., (2001) *Magnetics, IEEE Transactions on*, vol. 37, pp. 2651
44. Mizushima, K., Jones, P.C., Wiseman, P.J., Goodenough, J.B., (1980) *Materials Research Bulletin*, vol. 15, pp. 783
45. Chen, H., Qiu, X., Zhu, W., Hagenmuller, P., (2002) *Electrochemistry Communications*, vol. 4, pp. 488
46. Deb, P., Biswas, T., Sen, D., Basumallick, A., Mazumder, S., (2002) *Journal of Nanoparticle Research*, vol. 4, pp. 91
47. O'Brien, S., Brus, L., Murray, C.B., (2001) *J. Am. Chem. Soc.*, vol. 123, pp. 12085
48. Caruntu, D., Remond, Y., Chou, N.H., Jun, M.J., Caruntu, G., He, J., Goloverda, G., O'Connor, C., Kolesnichenko, V., (2002) *Inorg. Chem.*, vol. 41, pp. 6137
49. Pastoriza-Santos, I., Liz-Marzan, L.M., (2002) *Langmuir*, vol. 18, pp. 2888
50. Fievet, F., Lagier, J.P., Figlarz, M., (1989) *MRS Bulletin*, vol. 24, pp. 29
51. Yu, W., Tu, W., Liu, H., (1999) *Langmuir*, vol. 15, pp. 6

## References

52. Tsuji, M., Hashimoto, M., Tsuji, T., (2002) *Chemistry Letters*, vol. 31, pp. 1232
53. Tu, W., Liu, H., (2000) *Chem. Mater.*, vol. 12, pp. 564
54. Palchik, O., Avivi, S., Pinkert, D., Gedanken, A., (1999) *Nanostructured Materials*, vol. 11, pp. 415
55. Zhu, J., Palchik, O., Chen, S., Gedanken, A., (2000) *J. Phys. Chem. B*, vol. 104, pp. 7344
56. Palchik, O., Zhu, J., Gedanken, A., (2000) *Journal of Materials Chemistry*, vol. 10, pp. 1251
57. Palchik, O., Kerner, R., Gedanken, A., Weiss, A.M., Slifkin, M.A., Palchik, V., (2001) *Journal of Materials Chemistry*, vol. 11, pp. 874
58. Grisaru, H., Palchik, O., Gedanken, A., Palchik, V., Slifkin, M.A., Weiss, A.M., (2002) *Journal of Materials Chemistry*, vol. 12, pp. 339
59. Kerner, R., Palchik, O., Gedanken, A., (2001) *Chem. Mater.*, vol. 13, pp. 1413
60. Suslick, K.S., (1990) *Science*, vol. 247, pp. 1439
61. Flint, E.B., Suslick, K.S., (1991) *Science*, vol. 253, pp. 1397
62. Suslick, K.S., Hammerton, D.A., Cline, R.E., (1986) *J. Am. Chem. Soc.*, vol. 108, pp. 5641
63. Suslick, K.S., Choe, S.-B., Cichowlas, A.A., Grinstaff, M.W., (1991) *Nature*, vol. 353, pp. 414
64. Suslick, K.S., Fang, M., Hyeon, T., (1996) *J. Am. Chem. Soc.*, vol. 118, pp. 11960
65. Grinstaff, M.W., Salamon, M.B., Suslick, K.S., (1993) *Physical Review B*, vol. 48, pp. 269
66. Gonsalves, K.E., Rangarajan, S.P., Garcia-Ruiz, A., Law, C.C., (1996) *Journal of Materials Science Letters*, vol. 15, pp. 1261
67. Shafi, K.V.P.M., Koltypin, Y., Gedanken, A., Prozorov, R., Balogh, J., Lendvai, J., Felner, I., (1997) *J. Phys. Chem. B*, vol. 101, pp. 6409
68. Liang, J., Jiang, X., Liu, G., Deng, Z., Zhuang, J., Li, F., Li, Y., (2003) *Materials Research Bulletin*, vol. 38, pp. 161
69. Pang, G., Xu, X., Markovich, V., Avivi, S., Palchik, O., Koltypin, Y., Gorodetsky, G., Yeshurun, Y., Buchkremer, H.P., Gedanken, A., (2003) *Materials Research Bulletin*, vol. 38, pp. 11
70. Zheng, X., Xie, Y., Zhu, L., Jiang, X., Yan, A., (2002) *Ultrasonics Sonochemistry*, vol. 9, pp.

## References

311

71. Hoar, T.P., Schulman, J.H., (1943) *Nature*, vol. 152, pp. 102
72. Schulman, J.H., Riley, D.P., (1948) *Journal of Colloid Science*, vol. 3, pp. 383
73. Lisiecki, I., Pileni, M.P., (1993) *J. Am. Chem. Soc.*, vol. 115, pp. 3887
74. Lisiecki, I., Pileni, M.P., (1995) *J. Phys. Chem.*, vol. 99, pp. 5077
75. Carpenter, E.E., Sims, J.A., Wienmann, J.A., Zhou, W.L., Connor, C.J.O., (2000) *Journal of Applied Physics*, vol. 87, pp. 5615
76. Carpenter, E.E., Kumbhar, A., Wiemann, J.A., Srikanth, H., Wiggins, J., Zhou, W., O'Connor, C.J., (2000) *Materials Science and Engineering A*, vol. 286, pp. 81
77. O'Connor, C.J., Seip, C.T., Carpenter, E.E., Li, S., John, V.T., (1999) *Nanostructured Materials*, vol. 12, pp. 65
78. Yener, D.O., Giesche, H., (2001) *Journal of the American Ceramic Society*, vol. 84, pp. 1987
79. Zhang, Z.J., Wang, Z.L., Chakoumakos, B.C., Yin, J.S., (1998) *J. Am. Chem. Soc.*, vol. 120, pp. 1800
80. Yener, D.O., Giesche, H., (1999) *Ceramic Transactions*, vol. 94, pp. 407
81. Kumar, P., Pillai, V., Bates, S.R., Shah, D.O., (1993) *Materials Letters*, vol. 16, pp. 68
82. Pang, Y.-X., Bao, X., (2002) *Journal of Materials Chemistry*, vol. 12, pp. 3699
83. Hayashi, M., Uemura, H., Shimanoe, K., Miura, N., Yamazoe, N., (1998) *Electrochemical and Solid-State Letters*, vol. 1, pp. 268
84. Pillai, V., Kumar, P., Multani, M.S., Shah, D.O., (1993) *Colloids and Surfaces A: Physicochemical and Engineering Aspects*, vol. 80, pp. 69
85. Porta, F., Bifulco, C., Fermo, P., Bianchi, C.L., Fadoni, M., Prati, L., (1999) *Colloids and Surfaces A: Physicochemical and Engineering Aspects*, vol. 160, pp. 281
86. Lu, C.-H., Wang, H.-C., (2003) *Journal of Materials Chemistry*, vol. 13, pp. 428
87. Palla, B.J., Shah, D.O., Garcia-Casillas, P., Matutes-Aquino, J., (1999) *Journal of Nanoparticle Research*, vol. 1, pp. 215
88. Rajamathi, M., Seshadri, R., (2002) *Current Opinion in Solid State and Materials Science*,

## References

- vol. 6, pp. 337
89. Cansell, F., Chevalier, B., Demourgues, A., Etourneau, J., Even, C., Garrabos, Y., Pessey, V., Petit, S., Tressaud, A., Weill, F., (1999) *Journal of Materials Chemistry*, vol. 9, pp. 67
  90. Zhang, Z., Han, M., (2003) *Chemical Physics Letters*, vol. 374, pp. 91
  91. Jana, N.R., Gearheart, L., Murphy, C.J., (2001) *Chem. Mater.*, vol. 13, pp. 2313
  92. Schmid, G., Lehnert, A., Malm, J.-O., Bovin, J.-O., (1991) *Angewandte Chemie International Edition in English*, vol. 30, pp. 874
  93. Yu, H., Gibbons, P.C., Kelton, K.F., Buhro, W.E., (2001) *J. Am. Chem. Soc.*, vol. 123, pp. 9198
  94. Zanella, R., Giorgio, S., Henry, C.R., Louis, C., (2002) *J. Phys. Chem. B*, vol. 106, pp. 7634
  95. Fangli, Y., Peng, H., Chunlei, Y., Shulan, H., Jinlin, L., (2003) *Journal of Materials Chemistry*, vol. 13, pp. 634
  96. Harrison, M.T., Kershaw, S.V., Rogach, A.L., Kornowski, A., Eychmuller, A., Weller, H., (2000) *Advanced Materials*, vol. 12, pp. 123
  97. Pileni, M.P., (1998) *Crystal Research and Technology*, vol. 33, pp. 1155
  98. Brown, K.R., Natan, M.J., (1998) *Langmuir*, vol. 14, pp. 726
  99. Meldrum, F.C., Wade, V.J., Nimmo, D.L., Heywood, B.R., Mann, S., (1991) *Nature*, vol. 349, pp. 684
  100. Douglas, T., Young, M., (1998) *Nature*, vol. 393, pp. 152
  101. Douglas, T., Strable, E., Willits, D., Aitouchen, A., Libera, M., Young, M., (2002) *Advanced Materials*, vol. 14, pp. 415
  102. Mirkin, C.A., Letsinger, R.L., Mucic, R.C., Storhoff, J.J., (1996) *Nature*, vol. 382, pp. 607
  103. Loweth, C.J., Caldwell, W.B., Peng, X., Alivisatos, A.P., Schultz, P.G., (1999) *Angewandte Chemie International Edition*, vol. 38, pp. 1808
  104. Braun, E., Eichen, Y., Sivan, U., Ben-Yoseph, G., (1998) *Nature*, vol. 391, pp. 775
  105. Lee, S.-W., Mao, C., Flynn, C.E., Belcher, A.M., (2002) *Science*, vol. 296, pp. 892
  106. Mucic, R.C., Storhoff, J.J., Mirkin, C.A., Letsinger, R.L., (1998) *J. Am. Chem. Soc.*, vol. 120, pp. 12674

## References

107. Bashir, R., (2001) Superlattices and Microstructures, vol. 29, pp. 1
108. Storhoff, J.J., Mirkin, C.A., (1999) Chem. Rev., vol. 99, pp. 1849
109. Seidel, R., Mertig, M., Pompe, W., (2002) Surface and Interface Analysis, vol. 33, pp. 151
110. Dujardin, E., Peet, C., Stubbs, G., Culver, J.N., Mann, S., (2003) Nano Lett., vol. 3, pp. 413
111. Hench, L.L., West, J.K., (1990) Chem. Rev., vol. 90, pp. 33
112. Nishi, Y., (2000) Macromolecular Symposia, vol. 156, pp. 187
113. Scrosati, B., (2005) The Chemical Record, vol. 5, pp. 286
114. Auburn, J.J., Barberio, Y.L., (1987) Journal of The Electrochemical Society, vol. 134, pp. 638
115. Nishi, Y., (2001) The Chemical Record, vol. 1, pp. 406
116. Endo, M., Nishimura, Y., Takahashi, T., Takeuchi, K., Dresselhaus, M.S., (1996) Journal of Physics and Chemistry of Solids, vol. 57, pp. 725
117. Idota, Y., Kubota, T., Matsufuji, A., Maekawa, Y., Miyasaka, T., (1997) Science, vol. 276, pp. 1395
118. Courtney, I.A., McKinnon, W.R., Dahn, J.R., (1999) Journal of The Electrochemical Society, vol. 146, pp. 59
119. Courtney, I.A., Dahn, J.R., (1997) Journal of the Electrochemical Society, vol. 144, pp. 2045
120. Li, H., Huang, X., Chen, L., (1999) Journal of Power Sources, vol. 81-82, pp. 340
121. Chouvin, J., Olivier-Fourcade, J., Jumas, J.C., Simon, B., Biensan, P., Fernandez Madrigal, F.J., Tirado, J.L., Perez Vicente, C., (2000) Journal of Electroanalytical Chemistry, vol. 494, pp. 136
122. Chouvin, J., Branci, C., Sarradin, J., Olivier-Fourcade, J., Jumas, J.C., Simon, B., Biensan, P., (1999) Journal of Power Sources, vol. 81-82, pp. 277
123. Orel, B., Lavrencic-Stankgar, U., Crnjak-Orel, Z., Bukovec, P., Kosec, M., (1994) Journal of Non-Crystalline Solids, vol. 167, pp. 272
124. Takahashi, Y., Wada, Y., (1990) Journal of The Electrochemical Society, vol. 137, pp. 267
125. Santilli, C.V., Pulcinelli, S.H., Brito, G.E.S., Briois, V., (1999) J. Phys. Chem. B, vol. 103,

## References

- pp. 2660
126. Ayouchi, R., Martin, F., Ramos Barrado, J.R., Martos, M., Morales, J., Sanchez, L., (2000) Journal of Power Sources, vol. 87, pp. 106
  127. Brousse, T., Retoux, R., Herterich, U., Schleich, D.M., (1998) Journal of The Electrochemical Society, vol. 145, pp. 1
  128. Retoux, R., Brousse, T., Schleich, D.M., (1999) Journal of The Electrochemical Society, vol. 146, pp. 2472
  129. Nam, S.C., Kim, Y.H., Cho, W.I., Cho, B.W., Chun, H.S., Yun, K.S., (1999) Electrochemical and Solid-State Letters, vol. 2, pp. 9
  130. Yu, Y., Chen, C.H., Shi, Y., (2007) Advanced Materials, vol. 19, pp. 993
  131. Huang, F., Yuan, Z., Zhan, H., Zhou, Y., Sun, J., (2003) Materials Letters, vol. 57, pp. 3341
  132. Xiao, Y.W., Lee, J.Y., Yu, A.S., Liu, Z.L., (1999) Journal of The Electrochemical Society, vol. 146, pp. 3623
  133. Madrigal, F.J.F., Vicente, C.P., Tirado, J.L., (2000) Journal of The Electrochemical Society, vol. 147, pp. 1663
  134. Troup, J.M., Clearfield, A., (1977) Inorg. Chem., vol. 16, pp. 3311
  135. Elidrissi Moubtassim, M.L., Corredor, J.I., Tirado, J.L., Perez Vicente, C., (2001) Electrochimica Acta, vol. 47, pp. 489
  136. Moubtassim, M.L.E., Corredor, J.I., Lloris, J.M., Vicente, C.P., Tirado, J.L., (2002) Journal of The Electrochemical Society, vol. 149, pp. A1030
  137. Alcántara, Alcántara, R., Madrigal, F., Lavela, Lavela, P., Pérez, V., Pérez-Vicente, C., Tirado, Tirado, J., (2001) Journal of Solid State Electrochemistry, vol. 6, pp. 55
  138. Nagayama, M., Morita, T., Ikuta, H., Wakihara, M., Takano, M., Kawasaki, S., (1998) Solid State Ionics, vol. 106, pp. 33
  139. Wasmus, S., Kuver, A., (1999) Journal of Electroanalytical Chemistry, vol. 461, pp. 14
  140. Arico, A.S., Srinivasan, S., Antonucci, V., (2001) Fuel Cells, vol. 1, pp. 133
  141. Scott, K., Taama, W.M., Argyropoulos, P., (1999) Journal of Power Sources, vol. 79, pp. 43
  142. Scott, K., Taama, W., Cruickshank, J., (1997) Journal of Power Sources, vol. 65, pp. 159

## References

143. Liu, H., Song, C., Zhang, L., Zhang, J., Wang, H., Wilkinson, D.P., (2006) *Journal of Power Sources*, vol. 155, pp. 95
144. Yu, X., Ye, S., (2007) *Journal of Power Sources*, vol. 172, pp. 133
145. Savadogo, O., Beck, P., (1996) *Journal of The Electrochemical Society*, vol. 143, pp. 3842
146. Shim, J., Lee, C.-R., Lee, H.-K., Lee, J.-S., Cairns, E.J., (2001) *Journal of Power Sources*, vol. 102, pp. 172
147. Liu, G., Zhang, H., Zhai, Y., Zhang, Y., Xu, D., Shao, Z.-g., (2007) *Electrochemistry Communications*, vol. 9, pp. 135
148. Hills, C.W., Mack, N.H., Nuzzo, R.G., (2003) *J. Phys. Chem. B*, vol. 107, pp. 2626
149. Steigerwalt, E.S., Deluga, G.A., Cliffel, D.E., Lukehart, C.M., (2001) *J. Phys. Chem. B*, vol. 105, pp. 8097
150. Steigerwalt, E.S., Deluga, G.A., Lukehart, C.M., (2002) *J. Phys. Chem. B*, vol. 106, pp. 760
151. Fujiwara, N., Yasuda, K., Ioroi, T., Siroma, Z., Miyazaki, Y., (2002) *Electrochimica Acta*, vol. 47, pp. 4079
152. Dickinson, A.J., Carrette, L.P.L., Collins, J.A., Friedrich, K.A., Stimming, U., (2002) *Electrochimica Acta*, vol. 47, pp. 3733
153. Watanabe, M., Uchida, M., Motoo, S., (1987) *Journal of Electroanalytical Chemistry*, vol. 229, pp. 395
154. Radmilovic, V., Gasteiger, H.A., Ross, P.N., (1995) *Journal of Catalysis*, vol. 154, pp. 98
155. Castro Luna, A.M., Camara, G.A., Paganin, V.A., Ticianelli, E.A., Gonzalez, E.R., (2000) *Electrochemistry Communications*, vol. 2, pp. 222
156. Bensebaa, F., Patrito, N., Page, Y.L., L'Ecuyer, P., Wang, D., (2004) *Journal of Materials Chemistry*, vol. 14, pp. 3378
157. Liu, Z., Ling, X.Y., Lee, J.Y., Su, X., Gan, L.M., (2003) *Journal of Materials Chemistry*, vol. 13, pp. 3049
158. Wang, X., Hsing, I.M., (2002) *Electrochimica Acta*, vol. 47, pp. 2981
159. Kim, T., Takahashi, M., Nagai, M., Kobayashi, K., (2004) *Electrochimica Acta*, vol. 50, pp. 817

## References

160. Solla-Gullon, J., Vidal-Iglesias, F.J., Montiel, V., Aldaz, A., (2004) *Electrochimica Acta*, vol. 49, pp. 5079
161. Liu, Y., Qiu, X., Chen, Z., Zhu, W., (2002) *Electrochemistry Communications*, vol. 4, pp. 550
162. Crabb, E.M., Ravikumar, M.K., (2001) *Electrochimica Acta*, vol. 46, pp. 1033
163. Crabb, E.M., Marshall, R., Thompsett, D., (2000) *Journal of The Electrochemical Society*, vol. 147, pp. 4440
164. Crabb, E.M., Ravikumar, M.K., Qian, Y., Russell, A.E., Maniguet, S., Yao, J., Thompsett, D., Hurford, M., Ball, S.C., (2002) *Electrochemical and Solid-State Letters*, vol. 5, pp. A5
165. Takasu, Y., Kawaguchi, T., Sugimoto, W., Murakami, Y., (2003) *Electrochimica Acta*, vol. 48, pp. 3861
166. Uchida, M., Fukuoka, Y., Sugawara, Y., Ohara, H., Ohta, A., (1998) *Journal of The Electrochemical Society*, vol. 145, pp. 3708
167. Anderson, M.L., Stroud, R.M., Rolison, D.R., (2002) *Nano Lett.*, vol. 2, pp. 235
168. Park, G.-G., Yang, T.-H., Yoon, Y.-G., Lee, W.-Y., Kim, C.-S., (2003) *International Journal of Hydrogen Energy*, vol. 28, pp. 645
169. Rao, V., Simonov, P.A., Savinova, E.R., Plaksin, G.V., Cherepanova, S.V., Kryukova, G.N., Stimming, U., (2005) *Journal of Power Sources*, vol. 145, pp. 178
170. Wang, Z.-B., Yin, G.-P., Shi, P.-F., (2006) *Carbon*, vol. 44, pp. 133
171. Liu, Z., Lin, X., Lee, J.Y., Zhang, W., Han, M., Gan, L.M., (2002) *Langmuir*, vol. 18, pp. 4054
172. Wang, C., Waje, M., Wang, X., Tang, J.M., Haddon, R.C., Yan, Y.S., (2004) *Nano Lett.*, vol. 4, pp. 345
173. Matsumoto, T., Komatsu, T., Arai, K., Yamazaki, T., Kijima, M., Shimizu, H., Takasawa, Y., Nakamura, J., (2004) *Chemical Communications*, vol. 840
174. Tang, H., Chen, J.H., Huang, Z.P., Wang, D.Z., Ren, Z.F., Nie, L.H., Kuang, Y.F., Yao, S.Z., (2004) *Carbon*, vol. 42, pp. 191
175. Li, W., Liang, C., Qiu, J., Zhou, W., Han, H., Wei, Z., Sun, G., Xin, Q., (2002) *Carbon*, vol.

## References

- 40, pp. 791
176. Li, W., Liang, C., Zhou, W., Qiu, J., Zhou, Z.H., Sun, G., Xin, Q., (2003) *J. Phys. Chem. B*, vol. 107, pp. 6292
177. Li, W., Liang, C., Zhou, W., Qiu, J., Li, H., Sun, G., Xin, Q., (2004) *Carbon*, vol. 42, pp. 436
178. Che, G., Lakshmi, B.B., Martin, C.R., Fisher, E.R., (1999) *Langmuir*, vol. 15, pp. 750
179. Rajesh, B., Karthik, V., Karthikeyan, S., Ravindranathan Thampi, K., Bonard, J.M., Viswanathan, B., (2002) *Fuel*, vol. 81, pp. 2177
180. Rajesh, B., Ravindranathan Thampi, K., Bonard, J.M., Xanthopoulos, N., Mathieu, H.J., Viswanathan, B., (2003) *J. Phys. Chem. B*, vol. 107, pp. 2701
181. Girishkumar, G., Vinodgopal, K., Kamat, P.V., (2004) *J. Phys. Chem. B*, vol. 108, pp. 19960
182. Baughman, R.H., Zakhidov, A.A., de Heer, W.A., (2002) *Science*, vol. 297, pp. 787
183. Liu, Z., Lee, J.Y., Chen, W., Han, M., Gan, L.M., (2004) *Langmuir*, vol. 20, pp. 181
184. He, Z., Chen, J., Liu, D., Tang, H., Deng, W., Kuang, Y., (2004) *Materials Chemistry and Physics*, vol. 85, pp. 396
185. Lin, Y., Cui, X., Yen, C., Wai, C.M., (2005) *J. Phys. Chem. B*, vol. 109, pp. 14410
186. Komarneni, S., Li, D., Newalkar, B., Katsuki, H., Bhalla, A.S., (2002) *Langmuir*, vol. 18, pp. 5959
187. Chen, W., Zhao, J., Lee, J.Y., Liu, Z., (2005) *Materials Chemistry and Physics*, vol. 91, pp. 124
188. Serp, P., Corrias, M., Kalck, P., (2003) *Applied Catalysis A: General*, vol. 253, pp. 337
189. Han, K.I., Lee, J.S., Park, S.O., Lee, S.W., Park, Y.W., Kim, H., (2004) *Electrochimica Acta*, vol. 50, pp. 791
190. Sun, X., Li, R., Stansfield, B., Dodelet, J.P., Desilets, S., (2004) *Chemical Physics Letters*, vol. 394, pp. 266
191. Bessel, C.A., Laubernds, K., Rodriguez, N.M., Baker, R.T.K., (2001) *J. Phys. Chem. B*, vol. 105, pp. 1115
192. Park, K.W., Sung, Y.E., Han, S., Yun, Y., Hyeon, T., (2004) *J. Phys. Chem. B*, vol. 108, pp. 939

## References

193. Vinodgopal, K., Haria, M., Meisel, D., Kamat, P., (2004) *Nano Lett.*, vol. 4, pp. 415
194. Chan, K.-Y., Ding, J., Ren, J., Cheng, S., Tsang, K.Y., (2004) *Journal of Materials Chemistry*, vol. 14, pp. 505
195. Yu, J.S., Kang, S., Yoon, S.B., Chai, G., (2002) *J. Am. Chem. Soc.*, vol. 124, pp. 9382
196. Chai, G.S., Yoon, S.B., Yu, J.S., Choi, J.H., Sung, Y.E., (2004) *J. Phys. Chem. B*, vol. 108, pp. 7074
197. Raghuveer, V., Manthiram, A., (2004) *Electrochemical and Solid-State Letters*, vol. 7, pp.
198. Raghuveer, V., Manthiram, A., (2005) *Journal of the Electrochemical Society*, vol. 152, pp.
199. Chai, G.S., Yoon, S.B., Kim, J.H., Yu, J.-S., (2004) *Chemical Communications*, vol. 2766
200. Liu, Y.-C., Qiu, X.-P., Huang, Y.-Q., Zhu, W.-T., (2002) *Journal of Power Sources*, vol. 111, pp. 160
201. Liu, Y.C., Qiu, X.P., Huang, Y.Q., Zhu, W.T., (2002) *Carbon*, vol. 40, pp. 2375
202. Tirado, J.L., (2003) *Materials Science and Engineering: R: Reports*, vol. 40, pp. 103
203. Al-Hallaj, S., Selman, J.R., (2002) *Journal of Power Sources*, vol. 110, pp. 341
204. Mukai, S.R., Hasegawa, T., Takagi, M., Tamon, H., (2004) *Carbon*, vol. 42, pp. 837
205. Prem Kumar, T., Ramesh, R., Lin, Y.Y., Fey, G.T.-K., (2004) *Electrochemistry Communications*, vol. 6, pp. 520
206. Xie, J., Cao, G.S., Zhao, X.B., (2004) *Materials Chemistry and Physics*, vol. 88, pp. 295
207. Egashira, M., Takatsuji, H., Okada, S., Yamaki, J.-i., (2002) *Journal of Power Sources*, vol. 107, pp. 56
208. Mukaibo, H., Osaka, T., Reale, P., Panero, S., Scrosati, B., Wachtler, M., (2004) *Journal of Power Sources*, vol. 132, pp. 225
209. Flandrois, S., Simon, B., (1999) *Carbon*, vol. 37, pp. 165
210. Yazami, R., (2001) *Journal of Power Sources*, vol. 97-98, pp. 33
211. Alcantara, R., Lavela, P., Ortiz, G.F., Tirado, J.L., Stoyanova, R., Zhecheva, E., Merino, C., (2004) *Carbon*, vol. 42, pp. 2153
212. Wang, G.X., Ahn, J.-H., Lindsay, M.J., Sun, L., Bradhurst, D.H., Dou, S.X., Liu, H.K., (2001) *Journal of Power Sources*, vol. 97-98, pp. 211

## References

- 213. Shi, L., Li, H., Wang, Z., Huang, X., Chen, L., (2001) *Journal of Materials Chemistry*, vol. 11, pp. 1502
- 214. Mao, O., Dunlap, R.A., Dahn, J.R., (1999) *Journal of The Electrochemical Society*, vol. 146, pp. 405
- 215. Chen, W.X., Lee, J.Y., Liu, Z., (2003) *Carbon*, vol. 41, pp. 959
- 216. Dong, Q.F., Wu, C.Z., Jin, M.G., Huang, Z.C., Zheng, M.S., You, J.K., Lin, Z.G., (2004) *Solid State Ionics*, vol. 167, pp. 49
- 217. Wu, G.T., Wang, C.S., Zhang, X.B., Yang, H.S., Qi, Z.F., He, P.M., Li, W.Z., (1999) *Journal of The Electrochemical Society*, vol. 146, pp. 1696
- 218. Winter, M., Besenhard, J.O., (1999) *Electrochimica Acta*, vol. 45, pp. 31
- 219. Han, S.-C., Kim, K.-W., Ahn, H.-J., Ahn, J.-H., Lee, J.-Y., (2003) *Journal of Alloys and Compounds*, vol. 361, pp. 247
- 220. Joo, S.H., Choi, S.J., Oh, I., Kwak, J., Liu, Z., Terasaki, O., Ryoo, R., (2001) *Nature*, vol. 412, pp. 169
- 221. Guo, Z.P., Zhao, Z.W., Liu, H.K., Dou, S.X., (2005) *Carbon*, vol. 43, pp. 1392
- 222. Grigoriants, I., Sominski, L., Li, H., Ifargan, I., Aurbach, D., Gedanken, A., (2005) *Chemical Communications*, vol. 7, pp. 921
- 223. Fan, J., Wang, T., Yu, C., Tu, B., Jiang, Z., Zhao, D., (2004) *Advanced Materials*, vol. 16, pp. 1432
- 224. Han, S., Kim, M., Hyeon, T., (2003) *Carbon*, vol. 41, pp. 1525
- 225. Yang, J., Wachtler, M., Winter, M., Besenhard, J.O., (1999) *Electrochemical and Solid-State Letters*, vol. 2, pp. 161
- 226. Li, H., Shi, L., Wang, Q., Chen, L., Huang, X., (2002) *Solid State Ionics*, vol. 148, pp. 247
- 227. Kang, Y.-M., Kim, K.-T., Lee, K.-Y., Lee, S.-J., Jung, J.-H., Lee, J.-Y., (2003) *Journal of The Electrochemical Society*, vol. 150, pp. A1538
- 228. Wang, Y., Zeng, H.C., Lee, J.Y., (2006) *Advanced Materials*, vol. 18, pp. 645
- 229. Han, S., Jang, B., Kim, T., Oh, S.M., Hyeon, T., (2005) *Advanced Functional Materials*, vol. 15, pp. 1845

## References

230. Kim, E., Son, D., Kim, T.-G., Cho, J., Park, B., Ryu, K.-S., Chang, S.-H., (2004) *Angewandte Chemie*, vol. 116, pp. 6113
231. Lan, Y., Gao, X., Zhu, H., Zheng, Z., Yan, T., Wu, F., Ringer, S.P., Song, D., (2005) *Advanced Functional Materials*, vol. 15, pp. 1310
232. Yuan, Z.-Y., Su, B.-L., (2004) *Colloids and Surfaces A: Physicochemical and Engineering Aspects*, vol. 241, pp. 173
233. Armstrong, A.R., Armstrong, G., Canales, J., Garcia, R., Bruce, P.G., (2005) *Advanced Materials*, vol. 17, pp. 862
234. Armstrong, G., Armstrong, A.R., Canales, J., Bruce, P.G., (2006) *Electrochemical and Solid-State Letters*, vol. 9, pp. A139
235. Kim, G.-S., Seo, H.-K., Godble, V.P., Kim, Y.-S., Yang, O.B., Shin, H.-S., (2006) *Electrochemistry Communications*, vol. 8, pp. 961
236. Gao, X., Zhu, H., Pan, G., Ye, S., Lan, Y., Wu, F., Song, D., (2004) *J. Phys. Chem. B*, vol. 108, pp. 2868
237. Kavan, L., Gratzel, M., Rathousky, J., Zukalb, A., (1996) *Journal of The Electrochemical Society*, vol. 143, pp. 394
238. Wu, X., Jiang, Q.Z., Ma, Z.F., Fu, M., Shangguan, W.F., (2005) *Solid State Communications*, vol. 136, pp. 513
239. Ma, R., Bando, Y., Sasaki, T., (2003) *Chemical Physics Letters*, vol. 380, pp. 577
240. Wei, M., Konishi, Y., Zhou, H., Sugihara, H., Arakawa, H., (2005) *Solid State Communications*, vol. 133, pp. 493
241. Lindstrom, H., Sodergren, S., Solbrand, A., Rensmo, H., Hjelm, J., Hagfeldt, A., Lindquist, S.E., (1997) *J. Phys. Chem. B*, vol. 101, pp. 7717
242. Yamada, H., Yamato, T., Moriguchi, I., Kudo, T., (2004) *Solid State Ionics*, vol. 175, pp. 195
243. Kavan, L., Kalbac, M., Zukalova, M., Exnar, I., Lorenzen, V., Nesper, R., Graetzel, M., (2004) *Chem. Mater.*, vol. 16, pp. 477
244. Li, J., Tang, Z., Zhang, Z., (2005) *Electrochemical and Solid-State Letters*, vol. 8, pp. A316

## References

245. Planeix, J.M., Coustel, N., Coq, B., Brotons, V., Kumbhar, P.S., Dutartre, R., Geneste, P., Bernier, P., Ajayan, P.M., (1994) *J. Am. Chem. Soc.*, vol. 116, pp. 7935
246. J. Kong, M.G.C.H.D., (2001) *Advanced Materials*, vol. 13, pp. 1384
247. Quinn, B.M., Dekker, C., Lemay, S.G., (2005) *J. Am. Chem. Soc.*, vol. 127, pp. 6146
248. Jiang, L., Gao, L., (2003) *Carbon*, vol. 41, pp. 2923
249. Ellis, A.V., Vijayamohanan, K., Goswami, R., Chakrapani, N., Ramanathan, L.S., Ajayan, P.M., Ramanath, G., (2003) *Nano Lett.*, vol. 3, pp. 279
250. Yu, R., Chen, L., Liu, Q., Lin, J., Tan, K.L., Ng, S.C., Chan, H.S.O., Xu, G.Q., Hor, T.S.A., (1998) *Chem. Mater.*, vol. 10, pp. 718
251. Zhao, F., Wu, X., Wang, M., Liu, Y., Gao, L., Dong, S., (2004) *Anal. Chem.*, vol. 76, pp. 4960
252. Lee, J.K., Kim, M.J., (2002) *J. Org. Chem.*, vol. 67, pp. 6845
253. Barisci, J.N., Wallace, G.G., MacFarlane, D.R., Baughman, R.H., (2004) *Electrochemistry Communications*, vol. 6, pp. 22
254. Kosmulski, M., Osteryoung, R.A., Ciszewska, M., (2000) *Journal of The Electrochemical Society*, vol. 147, pp. 1454
255. Welton, T., (1999) *Chem. Rev.*, vol. 99, pp. 2071
256. Bonhote, P., Dias, A.P., Papageorgiou, N., Kalyanasundaram, K., Gratzel, M., (1996) *Inorg. Chem.*, vol. 35, pp. 1168
257. Banks, C.E., Davies, T.J., Wildgoose, G.G., Compton, R.G., (2005) *Chemical Communications*, vol. 7, pp. 829
258. Banks, C.E., Moore, R.R., Davies, T.J., Compton, R.G., (2004) *Chemical Communications*, vol. 16, pp. 1804
259. Yoshikawa, M., Katagiri, G., Ishida, H., Ishitani, A., Akamatsu, T., (1988) *Solid State Communications*, vol. 66, pp. 1177
260. Kastner, J., Pichler, T., Kuzmany, H., Curran, S., Blau, W., Weldon, D.N., Delamesiere, M., Draper, S., Zandbergen, H., (1994) *Chemical Physics Letters*, vol. 221, pp. 53
261. Wang, F.X., Gao, X.P., Lu, Z.W., Ye, S.H., Qu, J.Q., Wu, F., Yuan, H.T., Song, D.Y., (2004)

## References

- Journal of Alloys and Compounds, vol. 370, pp. 326
262. Liu, Z., Lee, J.Y., Han, M., Chen, W., Gan, L.M., (2002) Journal of Materials Chemistry, vol. 12, pp. 2453
263. Kim, M., Park, J.-N., Kim, H., Song, S., Lee, W.-H., (2006) Journal of Power Sources, vol. 163, pp. 93
264. Choi, W.C., Woo, S.I., Jeon, M.K., Sohn, J.M., Kim, M.R., Jeon, H.J., (2005) Advanced Materials, vol. 17, pp. 446
265. Zhao, Z.W., Guo, Z.P., Ding, J., Wexler, D., Ma, Z.F., Zhang, D.Y., Liu, H.K., (2006) Electrochemistry Communications, vol. 8, pp. 245
266. Babic, B.M., Vracar, L.M., Radmilovic, V., Krstajic, N.V., (2006) Electrochimica Acta, vol. 51, pp. 3820
267. Arbizzani, C., Beninati, S., Manferrari, E., Soavi, F., Mastragostino, M., (2007) Journal of Power Sources, vol. 172, pp. 578
268. Marie, J., Berthon-Fabry, S., Achard, P., Chatenet, M., Pradourat, A., Chainet, E., (2004) Journal of Non-Crystalline Solids, vol. 350, pp. 88
269. Smirnova, A., Dong, X., Hara, H., Vasiliev, A., Sammes, N., (2005) International Journal of Hydrogen Energy, vol. 30, pp. 149
270. Han, S., Hyeon, T., (1999) Chemical Communications, vol. 1955
271. Pang, J., Hu, Q., Wu, Z., Hampsey, J.E., He, J., Lu, Y., (2004) Microporous and Mesoporous Materials, vol. 74, pp. 73
272. Pekala, R.W., (1989) Journal of Materials Science, vol. 24, pp. 3221
273. Horikawa, T., Hayashi, J., Muroyama, K., (2004) Carbon, vol. 42, pp. 169
274. Chen, W.X., Lee, J.Y., Liu, Z., (2002) Chemical Communications, vol. 2588
275. Su, F., Zeng, J., Yu, Y., Lv, L., Lee, J.Y., Zhao, X.S., (2005) Carbon, vol. 43, pp. 2366
276. Zhu, J., Su, Y., Cheng, F., Chen, J., (2007) Journal of Power Sources, vol. 166, pp. 331
277. Mukerjee, S., Srinivasan, S., Soriaga, M.P., McBreen, J., (1995) Journal of the Electrochemical Society, vol. 142, pp. 1409
278. Paulus, U.A., Wokaun, A., Scherer, G.G., Schmidt, T.J., Stamenkovic, V., Radmilovic, V.,

## References

- Markovic, N.M., Ross, P.N., (2002) *J. Phys. Chem. B*, vol. 106, pp. 4181
279. Stamenkovic, V., Schmidt, T.J., Ross, P.N., Markovic, N.M., (2002) *J. Phys. Chem. B*, vol. 106, pp. 11970
280. Xu, Y., Ruban, A.V., Mavrikakis, M., (2004) *J. Am. Chem. Soc.*, vol. 126, pp. 4717
281. Toda, T., Igarashi, H., Uchida, H., Watanabe, M., (1999) *Journal of The Electrochemical Society*, vol. 146, pp. 3750
282. Xiong, L., Manthiram, A., (2004) *Electrochimica Acta*, vol. 49, pp. 4163
283. Chiu, H.C., Tseung, A.C.C., (1999) *Electrochemical and Solid-State Letters*, vol. 2, pp. 379
284. Koper, M.T.M., Lukkien, J.J., Jansen, A.P.J., van Santen, R.A., (1999) *J. Phys. Chem. B*, vol. 103, pp. 5522
285. Koper, M.T.M., Shubina, T.E., van Santen, R.A., (2002) *J. Phys. Chem. B*, vol. 106, pp. 686
286. Hayden, B.E., Rendall, M.E., South, O., (2003) *J. Am. Chem. Soc.*, vol. 125, pp. 7738
287. Kotobuki, M., Watanabe, A., Uchida, H., Yamashita, H., Watanabe, M., (2005) *Journal of Catalysis*, vol. 236, pp. 262
288. Yajima, T., Uchida, H., Watanabe, M., (2004) *J. Phys. Chem. B*, vol. 108, pp. 2654
289. Yuan, W., Scott, K., Cheng, H., (2006) *Journal of Power Sources*, vol. 163, pp. 323
290. Li, W., Zhou, W., Li, H., Zhou, Z., Zhou, B., Sun, G., Xin, Q., (2004) *Electrochimica Acta*, vol. 49, pp. 1045
291. Liu, C., Wu, X., Klemmer, T., Shukla, N., Weller, D., Roy, A.G., Tanase, M., Laughlin, D., (2005) *Chem. Mater.*, vol. 17, pp. 620
292. Shim, J., Yoo, D.-Y., Lee, J.-S., (2000) *Electrochimica Acta*, vol. 45, pp. 1943
293. Gurau, B., Viswanathan, R., Liu, R., Lafrenz, T., Ley, K., Smotkin, E., Reddington, E., Sapienza, A., Chan, B., Mallouk, T., Sarangapani, S., (1998) *J. Phys. Chem. B*, vol. 102, pp. 9997
294. El-Deab, M.S., Ohsaka, T., (2002) *Electrochimica Acta*, vol. 47, pp. 4255
295. Sarapuu, A., Tammeveski, K., Tenno, T.T., Sammelselg, V., Kontturi, K., Schiffrin, D.J., (2001) *Electrochemistry Communications*, vol. 3, pp. 446
296. Bard, A.J., Faulkner, L.R., *Electrochemical Methods*. 1980, New York: Wiley.

## LIST OF SYMBOLS

CV	Cyclic voltammetry
A.C. impedance	Alternating current impedance spectroscopy
SEM	Scanning electron microscope
TEM	Transmission electron microscope
HRTEM	High resolution transmission electron microscope
EDS	Electron dispersive spectroscopy
SAED	Selected area electron diffraction
XRD	X-Ray diffraction
BET	Brunauer-Emmett-Teller
Wt %	Weight percent
Mol %	Molar percent
$\text{mAh g}^{-1}$	Milli-ampere-hour per gram
$\text{mAh cm}^{-2}$	Milli-ampere-hour per square centimeter
ECA	Electrochemical surface area
SEI	Solid electrolyte interphase
Å	Angstrom
nm	Nanometer
$\mu\text{m}$	Micron

## LIST OF FIGURES

Fig. 3-1 Schematic diagram of experimental procedure.

Fig. 3-2 Schematic diagram of the configuration of the coin testing cell.

Fig. 3-3 Schematic diagram of the conventional three-electrode electrochemical cell.

Fig. 4-1 X-ray diffraction (XRD) patterns of (a) SnNi alloy; (b) MWNT-Sn nanocomposite; (c) Sn; and (d) MWNTs.

Fig. 4-2 SEM images of (a) SnNi; (b) MWNT-SnNi; (c) MWNT-Sn, and (d) typical TEM image of MWNT-Sn/SnNi nanocomposite.

Fig. 4-3 Cyclic voltammograms of (a) MWNT electrode; (b) the bare Sn electrode; (c) SnNi electrode; (d) MWNT-Sn electrode; and (e) MWNT-SnNi electrode.

Fig. 4-4 The discharge capacity vs. cycle number. The current density was 50 mA/g.

Fig. 4-5 The charge/discharge profiles in the first cycle for (a) bare MWNT electrode; (b) bare Sn electrode; (c) SnNi electrode; (d) MWNT-Sn electrode; and (e) MWNT-SnNi electrode.

Fig. 4-6 Schematic model of the lithiation and delithiation process in MWNT-Sn (top) and MWNT-SnNi (bottom) nanocomposites. For MWNT-Sn anode, most of the volume increases due to the formation of  $\text{Li}_x\text{Sn}$  alloys are buffered by the MWNT matrix, while the volume increases are effectively absorbed by the inactive component Ni in MWNT-SnNi on the local domain and further absorbed by the MWNT matrix on the macrodomain.

Fig. 4-7 Ac impedance spectra for the bare Sn electrode (top), MWNT-Sn electrode (center) and MWNT-SnNi electrode (bottom). ○: after 5 cycles; ■: after 10 cycles; △: after 20 cycles.

## List of Figures

Fig. 4-8 Equivalent circuit for the bare Sn and MWNT-Sn/SnNi nanocomposite electrodes.

Fig. 5-1 TEM images of the as-prepared samples: (a) TEM image of mesoporous carbon, (b) TEM image of the mesoporous carbon-tin nanocomposite.

Fig. 5-2 XRD pattern of (a) mesoporous carbon and (b) the mesoporous carbon-tin nanocomposite.

Fig. 5-3 Electrochemical properties of the mesoporous carbon-tin nanocomposites: (a) cyclic voltammograms of the as-prepared nanocomposites, (b) the first three charge/discharge curves, (c) cycling performance.

Fig. 5-4 SEM images of mesoporous carbon based tin inset nanocomposite electrodes: (a) before cycling, (b) after cycling for 200 times.

Fig. 5-5 The first charge/discharge curves of bare mesoporous carbon anode.

Fig. 5-6 Schematic diagram of mesoporous carbon-tin nanocomposite.

Fig. 6-1 TEM images of (a) the bare titania nanotubes, (b–d) titania nanotube supported tin anodes at different magnifications (inset in (b) is selected area diffraction pattern from a large region), and (e) the EDS spectrum from Sn particle.

Fig. 6-2 SEM images of (a) the bare titania nanotubes and (b) titania nanotube supported tin anodes.

Fig. 6-3 XRD patterns of (a) the bare titania nanotubes and (b) titania nanotube supported tin anodes.

Fig. 6-4 The charge/discharge curves of titania nanotube supported tin anodes, and cycle performance (inset) of  $\text{TiO}_2$  nanotube supported tin, tin, and  $\text{TiO}_2$  nanotube electrodes.

## List of Figures

Fig. 6-5 Cyclic voltammograms of  $\text{TiO}_2$  nanotube supported tin, tin, and  $\text{TiO}_2$  nanotube anodes.

Fig. 6-6 Discharge capacity vs. cycle number for titania nanotube supported tin anodes.

Fig. 7-1 Schematic structure of 1-ethyl-3-methylimidazolium

bis(trifluoromethylsulfonyl)imide ( $\text{EMI} \cdot \text{TFSI}$  or  $\text{EMI} \cdot \text{TFSA}$ ) ionic liquid (IL).

Fig. 7-2 XRD patterns of Platinum based catalysts (a) commercial Pt/C (JM); (b)

BMI  $\cdot$  TFSI IL supported synthesized Pt/CNTs; (c) EMI  $\cdot$  TFSI IL supported synthesized Pt/CNTs; (d) as prepared Pt/CNTs without IL support.

Fig. 7-3 TEM images of Pt nanoparticles decorated on the IL ( $\text{EMI} \cdot \text{TFSI}$ )-modified

multiwalled carbon nanotubes: (a) Bright-field image and (b) associated

dark-field image, (c) higher magnification dark-field image showing Pt particles

decorating either side of CNTs, (d) bright-field image showing individual Pt

particles and carbon nanotube lattice fringes (inset image). Dark-field images (b)

and (c) were obtained using Pt (1 1 1) reflections of first spotty in SAED patterns (inset top right of dark-field images).

Fig. 7-4 SEM secondary electron images and associated Pt X-ray maps obtained from

Pt/CNTs sample prepared, (a) and (c), without IL support; (b) and (d) prepared with the EMI  $\cdot$  TFSI ionic liquid support.

Fig. 7-5 Raman shifts of (a) as-prepared CNTs, (b) acid pretreated CNTs, (c) bare

Pt/CNTs prepared without IL support, and (d) IL supported synthesized Pt/CNTs.

Fig. 7-6 Cyclic voltammograms obtained from synthesized Pt/CNTs catalyst with and

without IL support, and from the commercial catalyst in 0.5 M  $\text{H}_2\text{SO}_4$ . The scan rate was performed at room temperature and the scan rate was 50 mV/s.

## List of Figures

Fig. 8-1 TEM images of (a) MC and SAED pattern (insert image), (b) Pt/MC, and (c), (d) Pt/CA.

Fig. 8-2 SEM images of Pt/MC (a) and Pt/CA (b).

Fig. 8-3 CV curves of the Pt/MC, Pt/CA, and commercial Pt/C in 0.5 M H<sub>2</sub>SO<sub>4</sub>. The scan rate was 50 mV/s at room temperature.

Fig. 8-4 N<sub>2</sub> sorption isotherms of the carbon aerogel and corresponding BJH pore size distribution (inset) derived from the desorption branch of the carbon aerogel.

Fig. 8-5 Cyclic voltammetry of Pt/CA electrode in 1 M CH<sub>3</sub>OH/ 0.5 M H<sub>2</sub>SO<sub>4</sub> solution at room temperature, at a scan rate of 50 mV/s.

Fig. 9-1 TEM bright and dark field image of as-prepared Pt/ FeO<sub>x</sub>/C nanocomposite (a) and (b). SAED patterns of Pt/FeO<sub>x</sub>/C nanocomposite (c). EDS spectrum (d).

Fig. 9-2 XRD pattern of Pt/ FeO<sub>x</sub>/C nanocomposite.

Fig. 9-3 HRTEM image of as-prepared Pt/FeO<sub>x</sub>/C nanocomposite suggested Pt particles are randomly oriented (inset image of bright field TEM image corresponding to (c) and (d)) (a). Dark field image were obtained using Pt (111) reflections of indicated spotty in SAED pattern (inset image) (b). Dark field image with FeO<sub>x</sub> (311) reflections in SAED pattern (inset image) (c).

Fig. 9-4 Relationship between the open circuit voltage (OCV) loss due to the methanol poisoning and the concentration of the methanol in 0.5 M H<sub>2</sub>SO<sub>4</sub> electrolytes.

Fig. 9-5 Oxygen reduction on a 4 mm diameter glassy carbon electrode in O<sub>2</sub>-saturated 0.5 M H<sub>2</sub>SO<sub>4</sub> at a scan rate of 20 mV/s. Rotation rate from 0 rpm to 3000 rpm.

Fig. 9-6 K-L plots for oxygen reduction on a glassy carbon electrode in 0.5 M H<sub>2</sub>SO<sub>4</sub> at various potentials.

## LIST OF TABLES

Table 3-1 Typical materials and chemicals used in this study.

Table 4-1  $Q_{20}/Q_{\max}$  of different samples ( $Q_{20}$  is the discharge capacity at the 20th cycles,  $Q_{\max}$  is the maximum discharge capacity of samples).

Table 4-2 Results of ac impedance analysis of the bare Sn, MWNT-Sn and MWNT-SnNi electrodes.

Table 7-1 Pt nanoparticle size calculated by Scherrer's formula based on the XRD pattern (220) peak.

Table 7-2 Amount of the Pt nanoparticle catalyst loaded on the CNT supports as estimated by standardless EDS analysis of large sample areas.

Table 7-3 The intensity ratio of the D and G bands ( $I_D/I_G$ ) obtained from Raman shift.

Table 7-4 The Specific Electrochemical Surface Area (ECA) of catalysts as determined by hydrogen electroadsorption

Table 8-1 The specific electrochemical surface area (ECA) of Pt/MC, Pt/CA, and commercial Pt/C catalysts as determined by hydrogen electroadsorption.

Table 9-1 The number of electrons exchanged per molecule of  $O_2$  to the applied potential.

## PUBLICATIONS

1. Guo, Z. P.; **Zhao, Z. W.**; Liu, H. K.; Dou, S. X., Electrochemical lithiation and de-lithiation of MWNT-Sn/SnNi nanocomposites. *Carbon* 2005, 43, 1392.
2. **Zhao, Z. W.**; Guo, Z. P.; Liu, H. K., Non-aqueous synthesis of crystalline  $\text{Co}_3\text{O}_4$  powders using alcohol and cobalt chloride as a versatile reaction system for controllable morphology. *Journal of Power Sources* 2005, 147, (1-2), 264-268.
3. Guo, Z. P.; **Zhao, Z. W.**; Liu, H. K.; Dou, S. X., Lithium insertion in Si-TiC nanocomposite materials produced by high-energy mechanical milling. *Journal of Power Sources* 2005, 146, (1-2), 190-194.
4. **Zhao, Z. W.**; Guo, Z. P.; Ding, J.; Wexler, D.; Ma, Z. F.; Zhang, D. Y.; Liu, H. K., Novel ionic liquid supported synthesis of platinum-based electrocatalysts on multiwalled carbon nanotubes. *Electrochemistry Communications* 2006, 8, (2), 245-250.
5. **Zhao, Z. W.**; Guo, Z. P.; Ma, Z. F.; Wu, X.; Liu, H. K., Titania nanotube supported tin anodes for lithium intercalation. *Electrochemistry Communications* 2007, 9, 697-702.
6. Wang, J.; Chew, S.Y.; **Zhao, Z. W.**; Ashraf, S.; Wexler, D.; Chen, J.; Ng, S.H.; Chou, S.L.; Liu, H. K., Sulfur-mesoporous carbon composites in conjunction with a novel ionic liquid electrolyte for lithium rechargeable batteries. *Carbon* 2008, 46, 229-235.
7. **Zhao, Z. W.**; Guo, Z. P.; Liu, H. K.; Dou, S. X., Various carbon metal nanocomposites for lithium ion batteries and direct methanol fuel cells. The 211<sup>th</sup> Electrochemical Society Meeting Transactions, Chicago 2007, (in press).
8. **Zhao, Z. W.**; Guo, Z. P.; Yao, P.; Liu, H. K.; Dou, S. X., Mesoporous carbon and tin nanocomposites as anode materials for Li-ion battery. *Journal of Materials Science and Technology* (invited paper in press).